



This is to certify that the

thesis entitled

Modeling A Radio Control Scale Helicopter For Robust Control Design

presented by

Chang-po Chao

has been accepted towards fulfillment of the requirements for

Macter degree in Mechanical Engineer, of Science

Date 2//6/93

**O**-7639

MSU is an Affirmative Action/Equal Opportunity Institution

LIBRARY Michigan State University

PLACE IN RETURN BOX to remove this checkout from your record.

TO AVOID FINES return on or before date due.

	E DATE DUE DATE DUE		
S.0 4 1995			
MAR BOLOUTE			
TIAN			
	-		
		•	

MSU Is An Affirmative Action/Equal Opportunity Institution characters pm3-p.

# MODELING A RADIO CONTROL SCALE HELICOPTER FOR ROBUST CONTROL DESIGN

Ву

Chang-po Chao

## **A THESIS**

Submitted to
Michigan State University
in partial fulfillment of the requirements
for the degree of

MASTER OF SCIENCE

Department of Mechanical Engineering

#### **ABSTRACT**

# MODELING A RADIO CONTROL SCALE HELICOPTER FOR ROBUST CONTROL DESIGN

# By Chang-po Chao

Helicopter flight control serves as an interesting and significant benchmark control design problem. In this study we look at the modeling of a scale helicopter and how it can be related to control design. Three nonlinear models of a radio control (R/C) scale helicopter, designed and fabricated in the Dynamic Systems and Control laboratory, are derived. Their only difference is the inflow velocity distribution assumed to exist over the rotor disk. After theses nonlinear models are determined we use the framework of uncertain linear system to represent them in a manner useful for robust control design. Our goal is to establish the effect of parameter variations in the nonlinear models on the uncertain linear system representations and their associated robust control designs. We use parametric and nonparametric uncertain linear system representations and the established theory of robust control. The 2-norm of the tracking error is our performance measure. Each controller is evaluated by considering the worst case tracking response of all possible compensated nonlinear models to step inputs of three different amplitudes (10°,20°,30°). The merit of each modeling effort and control design is considered and recommendations are made regarding the approach that offers the greatest promise for application.

DEDICATION

To my parents and girl friend who have given me the greatest love and support

#### **ACKNOWLEDGMENTS**

Over the past one and one half years a number of present and former professors and graduate students have contributed either directly or indirectly to my research. In particular, I would like to thank my major advisor Dr. Philip FitzSimons, who made me aware of standard procedures for system identification and convinced me of the advantages of the Internal Model Control structure. Without substantial advice and support, I could not have completed this project. I also owe special thanks to Dr. Clark Radcliffe who provided me timely help about my open-loop response measurement and Mr. Jerry Palazorro who designed the original helicopter hovering device a year ago. Finally, I would like to thank Xian Li Huang, Sachin Gogate, Parag Wakankar and Jonathan Iwamasa who have often assisted me in the Control Laboratory.

# TABLE OF CONTENTS

LIST OF TABLES v	⁄iii
LIST OF FIGURES	ix
NOMENCLATURE	хi
1 INTRODUCTION	
1.1 Modeling the Physical System	1
1.2 Modeling for Control System	2
1.3 Robust Control Design	2
2 MODELING THE PHYSICAL SYSTEM	
2.1 Parallelogram Linkage Dynamics	4
2.2 Drive Train Dynamics	5
2.3 Rotor Thrust and Torque	6
3 PARAMETER IDENTIFICATION	
3.1 Documented and Experimental Information Available	9
3.2 Nominal Linkage Parameters and How They were Determined	9
3.3 Nominal Rotor Parameters and How They were Determined	10
3.4 Nominal Motor/Drive Train Parameters and How They were Determined	12
3.5 Nominal Nonlinear State Variable Models	13
4 LINEARIZATION AND EXPERIMENTAL MODEL VALIDATION	
4.1 Linearization	15
4.2 Model Validation	16
5 MODELING FOR CONTROL DESIGN	
5.1 Linear State Variable Model	19
5.2 Effect of Physical model parameter variations on linear model parameter	
variation	19
5.3 Effect of Physical model nonlinearity on linear model parameter variation 2	20
5.4 Effect of Physical model parameter measurements on linear model parameter	

	variations using Conic Sector Bound method 2	.1
6 CONT	ROL DESIGN AND EVALUATION 2	:3
	6.1 Parametric Uncertainty 2	4
	6.2 Nonparametric Uncertainty 2	6
	6.3 Comprehensive Uncertainty 2	:7
	6.4 Nominal Plants Used for Robust Control Design 2	9
7 EVAL	UATION 3	1
	7.1 How is the Worst-Case Determined	1
	7.2 Worst-case responses for different robust controllers and the associated	
	models	2
8 CONC	CLUSION 3	7
REFERE	ENCE	8
APPENDI	IX	
A.1	Mathematical Development	
A.1.	.1 DC Motor Dynamics	9
A.1.	2 Application of Momentum Theory for Rotor 4	0
A.1.	3 Application of Blade Element Theory for Rotor4	2
A.1.	4 Linearization4	4
A.2	Experimental Data	
A.2.	1 Experimental Measurements of the DC Motor Armature Resistance 4	5
A.2.	2 Relationship between the Thrust and Speed of Rotor4	6
A.2.	Relationship among the Thrust, Torque, Speed of the Rotor, Current and	
	Voltage4	7
A.2.	4 Relationship between output voltage of Hall Effect sensor and the angular	
	displacement of the parallel linkages 4	8
A.3	Nominal System Parameters 4	9
A.4	Parameter Uncertainties5	1

A.5 Simulation Results	53
------------------------	----

# LIST OF TABLES

Number	Title Page	
3.3.1	Optimal rotor parameters	10
3.4.1	Optimal nominal parameters derived from power balance	12
5.3.1	The Conic Sector Bounds for three different models	22
7.2.1	Worst-case 2-norms for the cases with IMC filter which has $\lambda = 0.1$	32
7.2.2	Worst-case 2-norms for the cases with IMC filter which has $\lambda = 0.2$	33
A.2.1	Measurements of the motor armature resistance, $R_a$	45
A.2.2	Measurements for the relationship between the thrust and rotor speed	46
A.2.3	Measurements for the relationship among the thrust, torque, rotor,	
	current and voltage	47
A.2.4	Measurements for the relationship between Hall Effect sensor and	
	the angular displacement of the parallelogram linkage	48

# **LIST OF FIGURES**

Number	<u>Title</u>	age
1.1	Schematic diagram of the scale helicopter	1
2.1.1	Nomenclature of the parallelogram linkage	4
2.3.1	Velocity distributions	8
3.2	Hall Effect sensor curve fitting	9
3.3.1	The thrust with the associated optimized parameters	11
3.3.2	The load torques with the associated optimized parameters	11
3.4.1	Power balance with three different velocity distribution	13
4.2.1	Schematic diagram of the experimental setup	16
4.2.2	Experimental and theoretical Frequency Response	17
4.2.3	Coherence of the Frequency Response	18
6.0.1	The IMC structure	23
6.1.1	Fuzzy Nyquist plot for cubic model	24
6.1.2	Local Plot of $p(i\omega)c_c(i\omega)$ for cubic model	25
6.1.3	Upper bounds of the sensitivities for parametric representation	25
6.2.1	Robust stability consideration	26
6.2.2	Upper bounds of the sensitivity functions	27
6.3.1	Upper bounds of sensitivity fuctions for comprehensive representation	28
6.3.2	Robust consideration for "Comprehensive nonparametric representation"	28
6.4	Nominal plants	30
7.2.1	Worse-case response for 30° input with $\lambda = 0.1$ t	34
7.2.2	Worse-case response for 30° input with $\lambda = 0.2$	35
7.2.3	Control effort for input 300 with $\lambda = 0.2$	35
7.2.4	Rotor speed for input 30° with $\lambda = 0.1$	36
7.2.5	Rotor speed for input 30° with $\lambda = 0.2$	36
A.1.1	Simplified model of a DC motor	39

A.1.2	Control Volume used in Momentum Theory	40
A.1.3	2-D Airfoil Terms for a Rotor Blade Section	42

# NOMENCLATURE

<b>Abbreviations</b>	
IMC	Internal Model Control
ISE	Integral Squared Error
Symbols	
a	Airfoil lift curve slope
$b_0$	Coefficient of Coulomb friction for the rotor
$b_{i}$	Coefficient of viscous friction for the rotor
$b_{1,p}$	Coefficient of viscous friction for the parallelogram linkage
$C_L$	Lift coefficient
$C_{D}$	Drag coefficient
c	Airfoil chord length
$c_{c}(s)$	Classic feedback controller
d(s)	Disturbance
$dA_0$	Upstream cross-sectional differential area of the stream tube
$dA_1$	Cross-sectional differential area of the stream tube at the rotor disk
$dA_2$	Downstream cross-sectional differential area of the stream tube
D	Drag force
dD	Differential drag force
dL	Differential lift force
e(s)	Error signal
f(s)	IMC filter
fd	Feedback signal
$f_s$	Offset of the acting line of the thrust

8	Gravity	
$i_a$	Current of the DC motor armature circuit	
$J_r$	Total moment of inertia for the drive train, which referred to rotor speed	
$J_p$	Inertia of the parallel linkage	
$K_H$	Slope of the output equation for Hall Effect sensor	
$K_V$	Motor Back EMF constant	
$K_{\tau}$	Motor Torque constant	
L	Lift force	
$L_a$	Inductance of the DC motor armature circuit	
$L_{CG}$	Length from O to C.G. of the parallelogram linkage	
$L_p$	Length of rotor-side arm of parallel linkages	
L <sub>5</sub>	Length from the joint of the parallelogram linkage to center of mass of the counterweight	
$ar{l}_{_{m}}(\omega)$	Bound on the multiplicative uncertainty	
$K_H$	Slope of the output equation for Hall Effect sensor	
m	Mass of the parallelogram linkage and gear assembly	
$m_5$	Mass of the counterweight	
$P_0$	Atmospheric pressure	
$P_1$	Pressure on upper side of the rotor plane	
$P_2$	Pressure on lower side of the rotor plane	
p(s)	Plant model	
$ ilde{p}(s)$	Nominal model	
q(s)	IMC controller	
$ ilde{q}(s)$	1st step IMC controller for $H_2$ – optimal control	

R Radius of the rotor  $R_{a}$ DC Motor Armature resistance r Radial position from the center of the rotor  $r_i(s)$ Physical input r'(s)Normalized input  $\boldsymbol{T}$ Thrust generated by the rotation of the rotor  $\boldsymbol{V}$ Constant velocity  $V_{a}$ Motor armature voltage  $V_{b}$ Motor back EMF  $V_H$ Output voltage of Hall Effect sensor Velocity of the rotor disk relative to the ambient air  $v_0$ Velocity of the air flow through the rotor plane  $\nu_{\rm i}$ Velocity of the air flow through the rotor plane  $v_2$  $\nu_{w}$ Wind velocity w(s)Weighting function y(t), y(s)Calculated nominal system output y'(s)Actual process output Steady state y<sub>ss</sub>

#### **Greek Characters**

lpha Angle of attack of airfoil  $\Delta t$  Sampling time interval  $\varepsilon(s)$  Sensitivity  $\phi$  Inflow angle

λ Time constant of IMC filter

 $\theta$  Angular displacement of the parallelogram linkage

 $\theta_p$  Airfoil Pitch angle

 $\rho$  Air density

au Torque

 $au_{\it friction}$  Motor frictional torque

 $au_{motor}$  Motor output torque

 $au_{rotor}$  Load torque

 $\omega$  Rotor speed

## Subscript

bet Blade Element Theory

c Cubic velocity distribution

l Linear velocity distribution

mt Momentum Theory

O Nominal value

u Uniform velocity distribution

### 1. INTRODUCTION

## 1.1 Modeling the Physical System

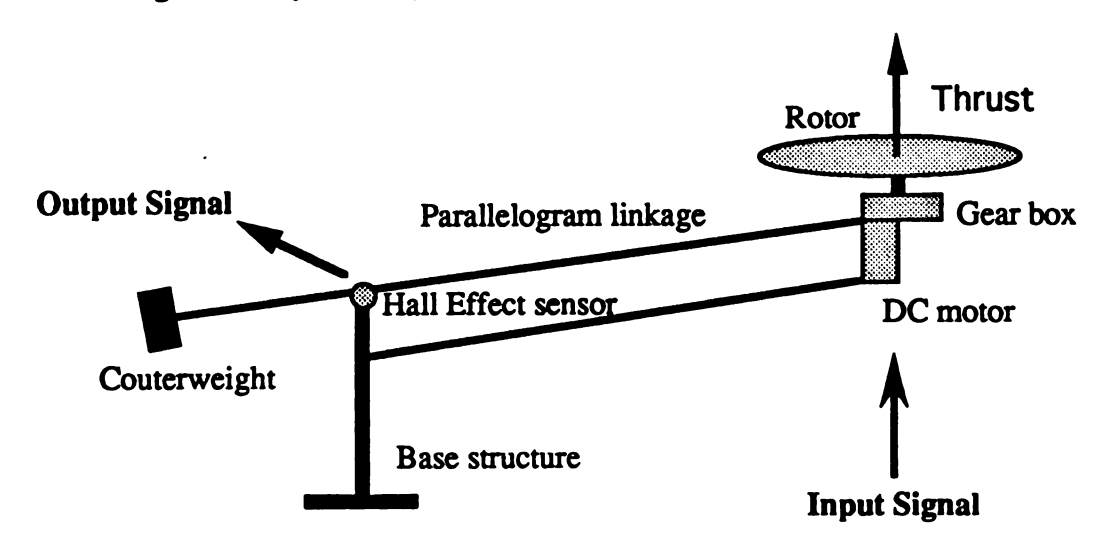


Figure 1.1 Schematic Diagram of the Scale Helicopter

A single-degree-of-freedom scale helicopter was designed and built in the Dynamic Systems and Control Laboratory to investigate the modeling and control of a rotor driven system. A schematic diagram of this device is shown in Figure 1.1. The mechanical part of the system has four components: a rotor system (DC motor, drive train and rotor), a parallelogram linkage, a base structure, and a counterweight. The rotor system is mounted on the parallelogram linkage, which is attached to the base structure, and is balanced by a counterweight that can be moved to adjust the equilibrium thrust level. The input signal corresponds to a voltage applied to the permanent magnet DC motor which powers the rotor through the drive train. The pitch of the individual rotor blades is fixed and the thrust of the rotor system is modulated by varying the rotor speed. The angle of the parallelogram linkage relative to the base is the controlled variable. A Hall Effect sensor provides the output signal which is used for control purposes.

A nonlinear, lumped parameter model was used to describe the dynamics of the device. The electrical dynamics of the DC motor were neglected since they are much faster than the mechanical dynamics of the system. The thrust produced and torque required by the rotor were obtained by combining Blade Element Theory and Momentum Theory (as in [2] and [3]). We assumed quasi-static aerodynamics and considered three different inflow velocity distributions over the rotor disk: uniform, linear, and cubic. The parameters required for each model were identified using the method of least squares to fit the theoretical results to static thrust measurements. Additional measurements and documented data were used to determine the nominal values and expected variations of the other model parameters.

### 1.2 Modeling for Control Design

Once the three nominal nonlinear models were determined, we used the framework of uncertain linear systems (ULS) to represent the dynamics of the device in a manner applicable to robust control design. Both parametric and nonparametric ULS representations were considered. We found the parametric ULS representations first and then used disk shaped uncertainty regions in the Nyquist plane to form the nonparametric representations. The parametric uncertainties in the ULS representations were the result of unknown system parameters and system nonlinearities. We used the hard bound method discussed in [5] and the conic sector bound method discussed in [6] to find bounds for these parameters. We considered four parametric uncertainty descriptions and four nonparametric uncertainty descriptions. Three of the parametric ULS models follow directly from the uncertain nonlinear models derived and have a similar algebraic structure. They differ only in the ranges of the parameters which result from the nonlinear terms associated with the different assumed inflow distributions. The fourth description we chose to include all three of the other descriptions. After finding the four parametric ULS descriptions we then found their associated nonparametric representations.

#### 1.3 Robust Control Design and Evaluation

The robust control design procedure we used consisted of two steps. In the first step, an  $H_2$  optimal control was designed to minimize the 2-norm of the tracking error for the

nominal linear plant model assuming a step input was to be tracked. Once the nominal controller was designed it was augmented by a low-pass filter which was adjusted to achieve robust stability and performance.

The main goal of this study was to determine how variations in the nonlinear model parameters affect the uncertain linear system models and the associated robust control designs. We considered eight different plant models, hence eight different controllers. To evaluate each controller we assumed that the "truth" model was described by one of the three nonlinear model structures considered and had parameters belonging to a prescribed allowable set. The performance of each controller was then judged by determining from among all of the possible "truth" models the tracking error with the largest 2-norm that resulted from a step up command held for ten seconds followed by a step down command held for ten seconds. In order to get a feel for the nonlinear behavior of the compensated systems three step amplitudes were used (10°,20°,30°).

## 2. MODELING THE PHYSICAL SYSTEM

## 2.1 Parallelogram Linkage Dynamics

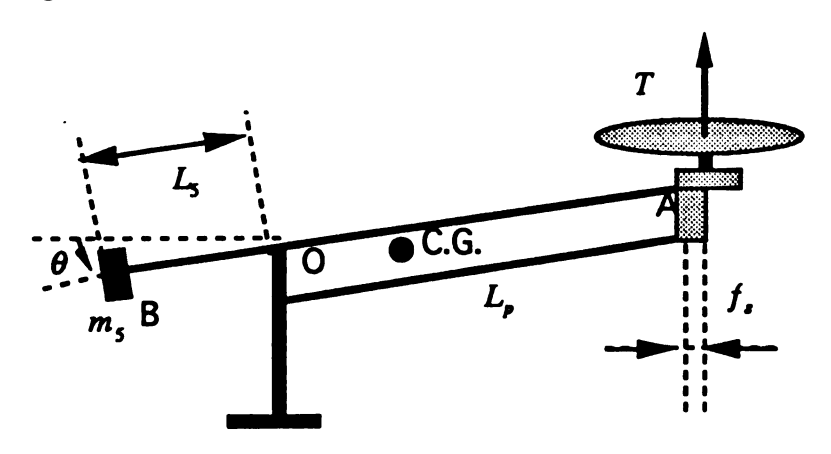


Figure 2.1.1 Nomenclature of the Parallelogram Linkage

Using the nomenclature of Figure 2.1.1 and elementary dynamics we find the equation of motion for the parallelogram linkage is given by

$$J_{\rho}\ddot{\theta} + b_{1,\rho}\dot{\theta} = \left(-Mg + TL_{\rho}\right)\cos\theta + Tf_{s} \tag{2.1.1}$$

$$J_p = J_p' + L_5^2 m_5 (2.1.2)$$

$$M = L_{CG}m - L_5m_5 (2.1.3)$$

where  $b_{1,p}$  = Coefficient of viscous friction for the parallelogram linkage

 $f_{\star}$  = Offset of the acting line of the thrust

 $J_p$  = Moment of inertia about O

 $J_p$  = Moment of inertia of the parallelogram linkage + rotor system

L<sub>5</sub> = Length from the joint of the parallelogram linkage, O, to the center of mass of the counterweight

 $L_{CG}$  = Length from O to C.G. of the parallelogram linkage

 $L_p$  = Length from the joint of the parallelogram linkage, O, to the shaft of the DC motor

m =Mass of the parallelogram linkage and rotor assembly

 $m_s$  = Mass of the counterweight

T = Thrust generated by the rotor

 $\theta$  = Angular displacement of the parallelogram linkage

## 2.2 Drive Train Dynamics

A permanent magnet DC motor is used to drive the rotor through a single stage drive train. The motor output torque balances the load torque which has three components. These three components include the torque required to accelerate the drive train/rotor system, the torque required to drive the rotor blades through the air,  $\tau_{rotor}$ , and the torque required to overcome friction in the drive train,  $\tau_{friction}$ . The relationship among these torques is given by (see Appendix A.1.1)

$$K_{\tau} \left( \frac{V_a - K_v \omega}{R_a} \right) = J_r \dot{\omega} + \tau_{rotor} + \tau_{friction}$$
 (2.2.1)

$$K_{\tau} \left( \frac{V_a - K_{\nu} \omega}{R_a} \right) = J_r \dot{\omega} + \tau_{rotor} + b_0 sign(\omega) + b_1 \omega$$
 (2.2.2)

where

 $b_0$  = Coulomb friction coefficient

 $b_1$  = Viscous friction coefficient

 $J_r$  = Total Moment of Inertia of the Drive Train + Rotor (referred to the rotor speed)

 $K_{\nu}$  = Back EMF Constant (referred to the rotor speed)

 $K_{\tau}$  = Torque Constant (referred to the rotor speed)

 $R_a$  = Armature Resistance

 $V_a$  = Supply Voltage

 $\omega$  = Rotor Speed

and in the second expression we assume  $\tau_{friction}$  results from Coulomb and viscous friction terms.

#### 2.3 Rotor Thrust and Torque

To predict the thrust and torque generated by the rotor we combine Blade Element Theory and Momentum Theory [2], [3]. The basic assumptions required are that the air is incompressible, the flow is quasi-static and the inflow velocity distribution over the rotor disk,  $v_1 = v_1(r)$ , is represented by a one parameter family of surfaces. Three commonly assumed inflow velocity distributions are uniform, linear, and cubic

$$v_1(r) = V_{\mu} \tag{2.3.1}$$

$$v_1(r) = V_1 \times r \tag{2.3.2}$$

$$v_1(r) = V_c \times r^2 \times (R - r) \tag{2.3.3}$$

where

r =Radial distance from the rotor's hub

R =Radius of the rotor

 $V_{\mu}, V_{\ell}, V_{\epsilon}$  = Parameters of the inflow velocity distributions

Once the inflow velocity distribution is assumed we find two differential expressions for thrust. One results from Momentum Theory (see Appendix A.1.2) and the other from Blade Element Theory (see Appendix A.1.3). Integrating each of these expressions and then setting them equal to each other makes it possible to solve for the inflow velocity parameter. This, in turn, makes it possible to determine the thrust produced and the torque required by the rotor as a function of the rotor parameters, rotor speed, and velocity of the rotor relative to the air mass. The expressions that result are given below.

#### (1) Rotor Model Assuming Uniform Inflow Distribution

$$T_{u,bet} = \rho ac \left( \omega^2 \theta_p \frac{R^3}{3} - \omega \frac{R^2}{2} V_u \right) \tag{2.3.4}$$

$$T_{u,mi} = 2\pi\rho R^2 (V_u^2 - V_u v_0)$$
 (2.3.5)

$$V_{\mu} = \left(\frac{v_0}{2} - \frac{\omega ac}{8\pi}\right) + \frac{1}{2}\sqrt{\left(\frac{ac\omega}{4\pi} - v_0\right)^2 + \frac{2ac\omega^2\theta_p R}{3\pi}}$$
(2.3.6)

$$\tau_{rotor,u} = \rho ac \left( \omega \theta_p V_u \frac{R^3}{3} - V_u^2 \frac{R^2}{2} \right)$$
 (2.3.7)

## (2) Rotor Model Assuming Linear Inflow Distribution

$$T_{l,bet} = \rho ac \left(\omega^2 \theta_p - \omega V_l\right) \frac{R^3}{3} \tag{2.3.8}$$

$$T_{l,ml} = 4\pi\rho \left(\frac{R^4}{4}V_l^2 - \frac{R^3}{3}v_0V_l\right)$$
 (2.3.9)

$$V_{I} = \left(\frac{4v_{0}}{6R} - \frac{ac\omega}{6\pi R}\right) + \frac{1}{2}\sqrt{\left(\frac{ac\omega}{3\pi R} - \frac{4v_{0}}{3R}\right)^{2} + \frac{4ac\omega^{2}\theta_{p}}{3\pi R}}$$
(2.3.10)

$$\tau_{rowr,l} = \rho ac \left(\omega \theta_{\rho} V_{l} - V_{l}^{2}\right) \frac{R^{4}}{4}$$
 (2.3.11)

## (3) Rotor Model Assuming Cubic Inflow Distribution

$$T_{c,bet} = \rho ac \left( \omega^2 \theta_p \frac{R^3}{3} - \frac{\omega V_c R^5}{20} \right) \tag{2.3.12}$$

$$T_{c,ml} = 4\pi\rho \left(\frac{R^8}{168}V_c^2 - \frac{R^5}{20}v_0V_c\right)$$
 (2.3.13)

$$V_{c} = \left(\frac{21v_{0}}{5R^{3}} - \frac{21ac\omega}{20\pi R^{3}}\right) + \frac{1}{2}\sqrt{\left(\frac{21ac\omega}{10\pi R^{3}} - \frac{42v_{0}}{5R^{3}}\right)^{2} + \frac{56ac\omega^{2}\theta_{p}}{\pi R^{5}}}$$
(2.3.14)

$$\tau_{rowr,c} = \rho ac \left( \omega \theta_{p} V_{c} \frac{R^{6}}{30} - V_{c}^{2} \frac{R^{8}}{168} \right)$$
 (2.3.15)

Note that the subscripts u, c, l refer to the uniform, cubic and linear velocity distributions, respectively. The subscript bet indicates the expression derived from Blade Element Theory and mt indicates that it derived from Momentum Theory.

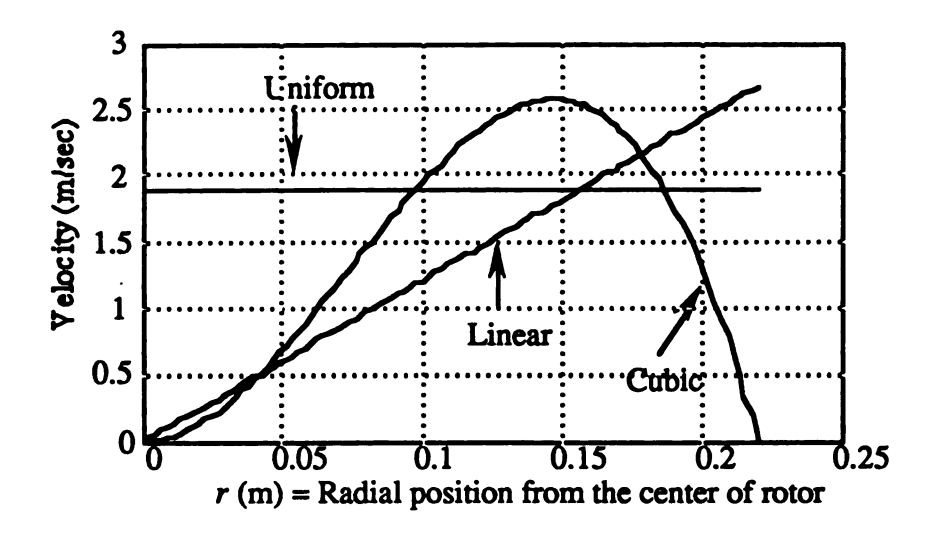


Figure 2.3.1 Velocity distributions

Three different velocity distributions are shown in Figure 2.3.1 that generating the same magnitude thrust (0.3 LB = 1.33 N).

Among the three velocity distributions shown it appears that the cubic one is most appealing on physical grounds. However, the other two distributions are often used for historical reasons or due to their simplicity.

#### 3 PARAMETER IDENTIFICATION

### 3.1 Documented and Experimental Information Available

The motor armature resistance,  $R_e$ , was measured at twenty-three different rotor rotative positions (Appendix A.2.1). The nominal value was determined to be the average of the above twenty measurements. The torque constant,  $K_{\tau}$ , which has the same numerical value as the back EMF constant,  $K_{\tau}$ , in SI was obtained by referring to the catalog provided by the DC motor company (and factoring in the gear ratio since we use the rotor speed as our reference). To investigate the relationships among the thrust, rotor speed, motor armature current and voltage, we performed a static thrust test (Appendix A.2.2 and A.2.3). The thrust was measured using a model DFG 50 force gauge [8] from the Chantillon Company. The rotor speed was measured using a B&K model strobescope type 4913. The armature current and the applied voltage were determined using two model Fluke 77 digital multimeters.

## 3.2 Nominal Linkage Parameters and How They were Determined

The relationship between the output voltage of the Hall Effect Sensor and the angular displacement of the parallelogram linkage was also investigated by experiment (see Appendix A.2.4).

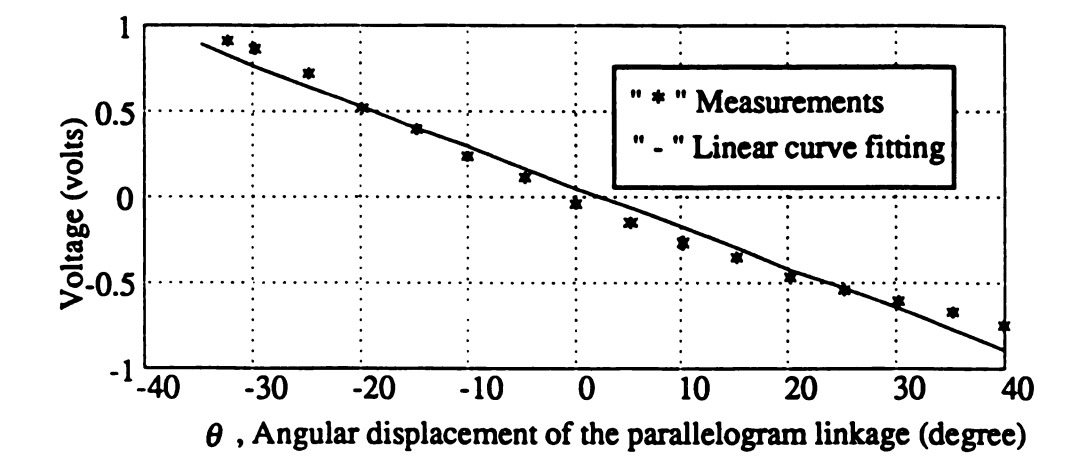


Figure 3.2 Hall Effect sensor curve fitting

The linear curve fitting in Figure 3.2 shows that over a certain range of the magnetic rotation, the relationship between angular position and the output voltage is linear and the nominal voltage output is nearly zero. This linear relationship can be approximated by

$$V_H = K_H \theta \tag{3.2.1}$$

where  $K_H = 0.0235$  (Volts/degree) and  $V_H$  is the output voltage of the sensor.

## 3.3 Nominal Rotor Parameters and How They were Determined

Among the rotor and aerodynamic parameters, the chord length, c, and the radius of the rotor, R, were measured directly. The variation of air density  $\rho$  in the laboratory is small enough to be ignored. Because the pitch angle  $\theta_p$  may be different from its static value when the rotor is rotating and the exact value of the characteristic lift curve slope a is hard to determine, the theoretical thrust can not predict very well if we use these parameter value. To solve this problem, the least square method is utilized to calculate the optimal rotor parameters  $\theta_p$  and a by fitting theoretical to experimental thrust (see Appendix A.2.2). The results are shown in Table 3.3.1.

Table 3.3.1 Optimal rotor parameters

	Uniform model	Linear model	Cubic model
a (no unit)	6.05	5.99	5.72
$\theta_p$ (degree)	13.1	12.8	13.0

Figure 3.3.1 shows that the thrust predicted using the associated optimized parameters listed in Table 3.3.1 are almost the identical curves. It makes us ensured that all three thrust prediction can well predict the thrust well with the rotor speed from 0 RPM to 1400 RPM.

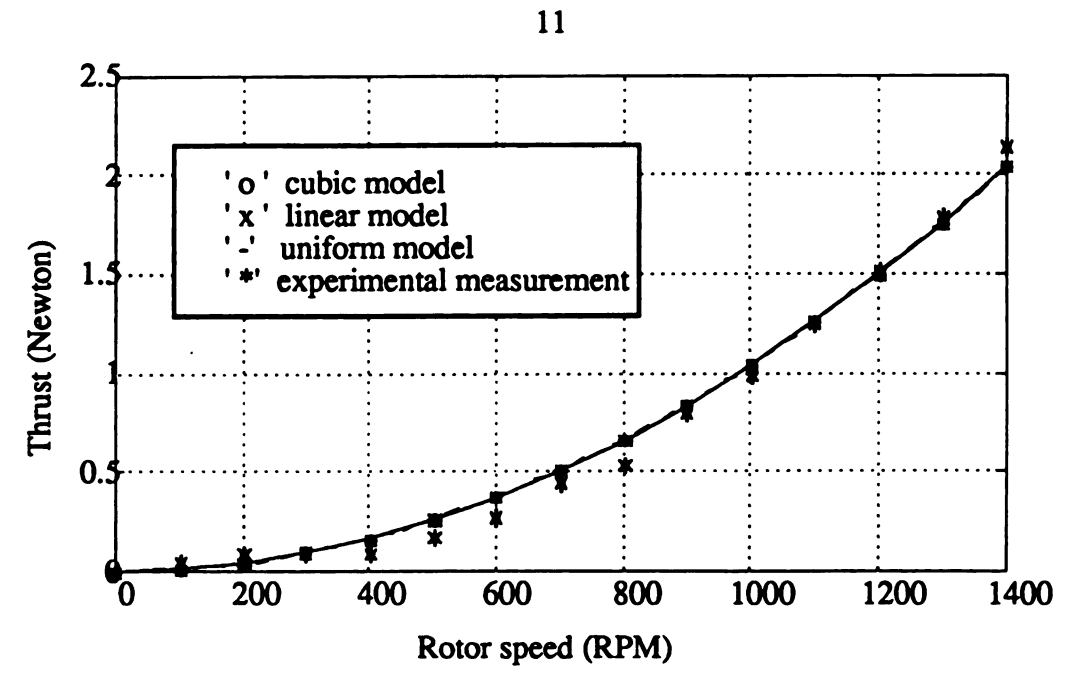


Figure 3.3.1 The thrust with the associated optimized parameters

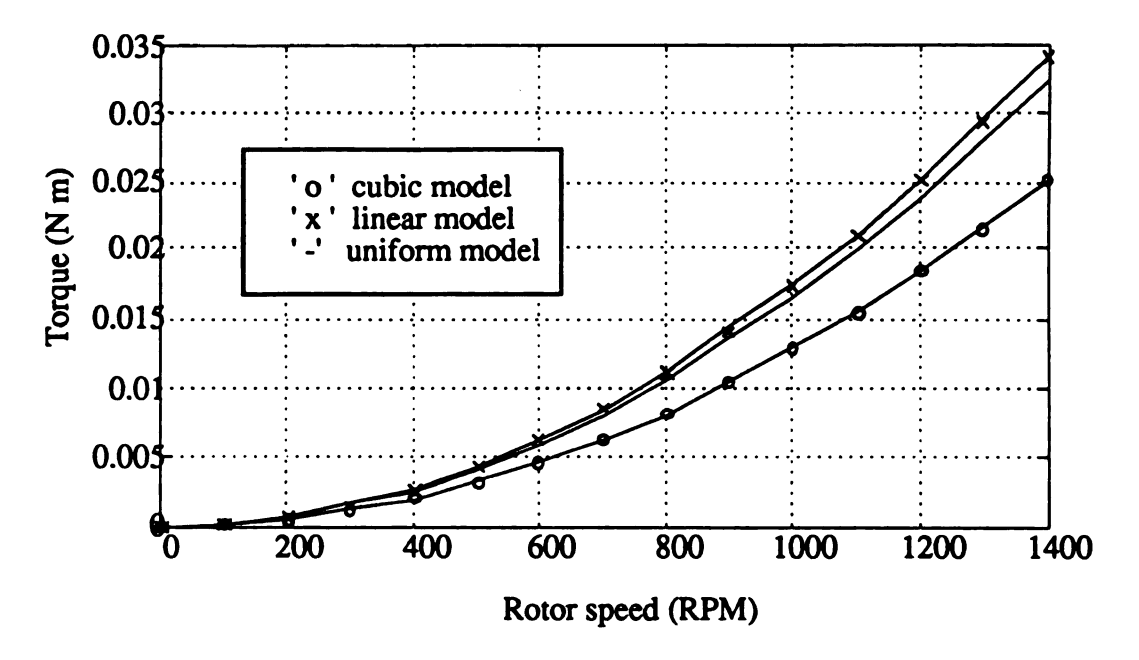


Figure 3.3.2 The load torques with the associated optimized parameters

In Figure 3.3.2 the load torques predicted by three different set of optimal parameters receptively shown to be different especially in high rotor speed range.

#### 3.4 Nominal Motor/Drive Train Parameters and How They were Determined

Among motor/drive train parameters, the coefficient of Coulomb friction for the DC motor,  $b_0$ , was obtained by measuring the largest current that could be applied to the motor without initiating rotor rotation. The coefficient of viscous friction,  $b_1$ , was identified by the power balance

$$i_a V_a = \tau_{rotor} \omega + i_a^2 R_a + \tau_{friction} \omega \tag{3.4.1}$$

We assume the frictional terms result from the sum of the Coulomb's and viscous friction, then the above equation become

$$i_a V_a = \tau_{rowr} \omega + i_a^2 R_a + b_0 |\omega| + b_1 \omega^2$$
 (3.4.2)

In (3.4.2), since a,  $\theta_p$  used to predict  $\tau_{rotor}$  are set to fit the experimental results using the measurements of the thrust, we can assume  $\tau_{rotor}$  is well predicted and the nominal values of  $V_a$ ,  $i_a$ ,  $R_a$  and  $b_0$  can be measured, the only unknown in the power balance (3.4.2) is the coefficient of the viscous friction,  $b_1$ . Therefore by fitting the output power to the input power and using least square method again, three nominal optimal  $b_1$  are obtained in Table 3.4.1 for three different velocity distributions.

Table 3.4.1 Optimal nominal parameters derived from power balance

	b <sub>1</sub> (Nm sec/rad)	
Uniform Distribution	3.41x10 <sup>-4</sup>	
Linear Distribution	3.29x10 <sup>-4</sup>	
Cubic Distribution	3.85x10 <sup>-4</sup>	

Table 3.4.1 reveals that the values of  $b_1$  for uniform and linear distribution are smaller than the cubic one because the load torque predicted by uniform and linear distribution in Figure 3.3.2 is larger than the other's.

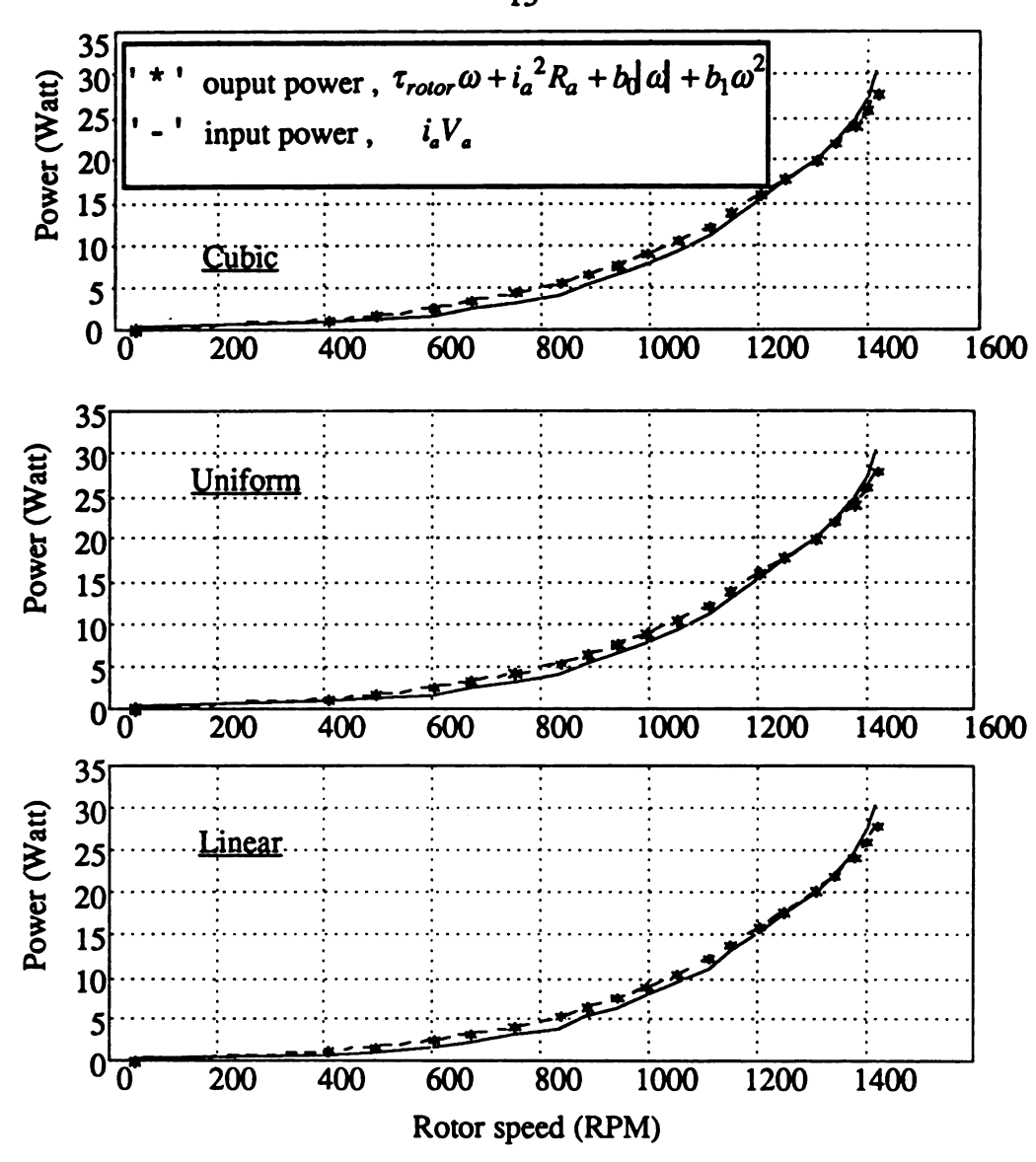


Figure 3.4.1 Power balance with three different velocity distribution

Figure 3.4.1 shows that the output power and the input power can well balanced for the three different velocity distributions with their associated optimal parameters  $b_1$ 's and the fittings shown up are almost identical for three different velocity distributions.

### 3.5 Nominal Nonlinear State Variable Model

With the equation of motion for the parallelogram linkage, the equation describing the drive train dynamics, the expressions used to predict the thrust and torque and the parameters determined in this section which are measurable nominal values or optimized

ones, the overall nonlinear system can be described by the following two nonlinear differential equations and one output equation.

$$J_{p}\ddot{\theta} + b_{1,p}\dot{\theta} = (-Mg + T \times L_{p})\cos\theta + f_{s} \times T \tag{2.1.1}$$

$$\dot{\omega} = \left(K_{\tau} \left(\frac{V_a - K_{\nu}\omega}{R_a}\right) - b_0 sign(\omega) - b_1 \omega - \tau_{rotor}\right) / J_r$$
 (2.2.1)

$$V_H = K_H \theta \tag{3.2.1}$$

In addition to some dimensions and weights which can be measured directly, the other parameters should have uncertainties associated with them such as

- (1) Motor armature resistance  $R_a$
- (2) Coulomb's friction  $b_0$
- (3) Coefficient of the viscous friction  $b_1$
- (4) Torque and Back EMF constant,  $K_{\tau}$  and  $K_{\nu}$
- (5) Slope of the hall Effect output equation (3.2.1),  $K_H$
- (6) Lift curve slope, a
- (7) Pitch angle,  $\theta_p$

In state variable form, we may combine the nominal nonlinear state variable model (2.1.1), (2.2.1) and (3.2.1) to be written as nonlinear state equations

$$\dot{\mathbf{x}} = \mathbf{f}(\mathbf{x}, u)$$

$$y = K_H x_1$$
(3.5.1)

where

$$\mathbf{x} = \begin{bmatrix} x_1 \\ x_2 \\ x_3 \end{bmatrix} = \begin{bmatrix} \theta \\ \dot{\theta} \\ \omega \end{bmatrix}$$

$$\mathbf{y} = V_{\mathbf{H}}$$

# 4 LINEARIZATION AND EXPERIMENTAL MODEL VALIDATION

#### 4.1 Linearization

In the laboratory, for the case the counterweight is set to be 2 lb (0.91 kg), the operating range for the angular displacement of the parallelogram linkage is from -40 degree to 50 degree and the input armature voltage  $V_a$  is about from 6.2 volts to 7.2 volts to prevent the bottom of the gear box from hitting the ground. By setting the right hand side of the nonlinear state equations (3.5.1) to zeros and solving it, we find the nominal supply voltage and the nominal motor speed

$$V_{a,0} = 6.40 \text{ (Volts)}, \ \omega_0 = 853 \text{ (RPM)}, \ \dot{\theta}_0 = 0 \text{ (rad / sec)}$$
 (4.1.1)

needed to keep the parallelogram linkage at the equivalent position  $\theta_o$ . This set of nominal values are especially for the case of the cubic velocity distribution model. Using these nominal values, the nonlinear state equations (3.5.4) can be linearized as (see Appendix A.1.5)

where 
$$\dot{\mathbf{x}} = \mathbf{A}\mathbf{x} + \mathbf{B}\mathbf{u}$$

$$y = \mathbf{C}\mathbf{x}$$

$$\mathbf{A} = \begin{bmatrix} 0 & 1 & 0 \\ a_{21} & a_{22} & a_{23} \\ 0 & a_{32} & a_{33} \end{bmatrix},$$

$$\mathbf{B} = \begin{bmatrix} 0 \\ 0 \\ b_3 \end{bmatrix}$$

$$\mathbf{C} = \begin{bmatrix} K_H & 0 & 0 \end{bmatrix}$$

$$(4.1.2)$$

For the case that the equivalent  $\theta_o$  is 50, the linearized A, B, and C are

$$\mathbf{A} = \begin{bmatrix} 0 & 1 & 0 \\ -0.0094 & -0.3979 & 0.05320 \\ 0 & 0.5763 & -3.6531 \end{bmatrix}$$

$$\mathbf{B} = \begin{bmatrix} 0 & 0 & 49.6161 \end{bmatrix}^{T}$$

$$\mathbf{C} = \begin{bmatrix} 1.4324 & 0 & 0 \end{bmatrix}$$

$$\lambda(\mathbf{A}) = \begin{bmatrix} -3.6672 & -1.4795 & -0.0064 \end{bmatrix}$$

We can see that the system have three non zero stable eigenvalues including one very slow eigenvalue which is close to imaginary axis.

#### 4.2 Model Validation

A experimental set-up shown in Figure 4.2.1 was used to investigate open-loop response for model validation.

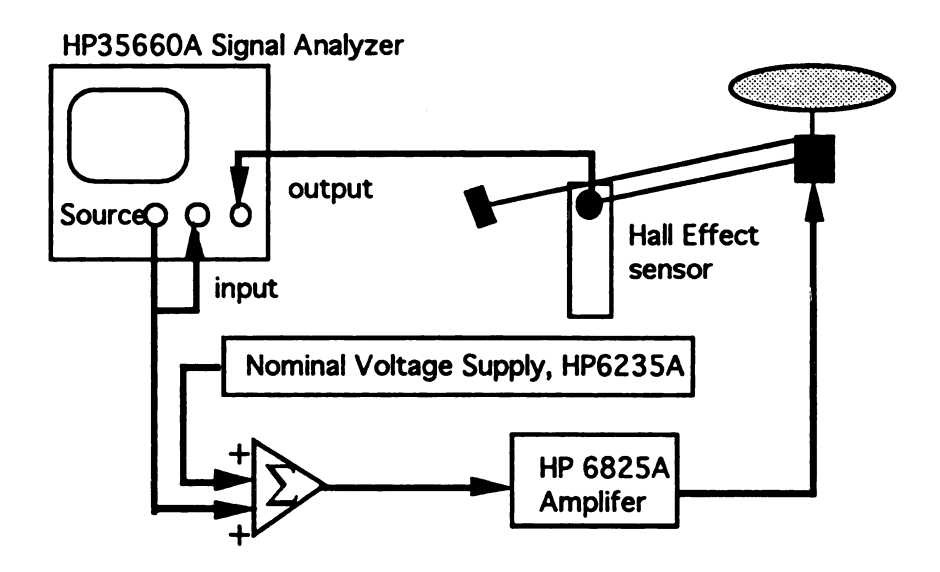


Figure 4.2.1 Schematic diagram of the experimental setup

The HP 35660A signal analyzer [7] was used to investigate the frequency response. This analyzer can provide a source signal for excitation as input signal of the analyzer itself. In this experiment set-up this signal was added to the nominal voltage which is supplied by the HP 6235A power supply and is estimated off-line by the preceding experiments, which measured the armature DC motor voltage  $V_{\bullet,0}$  required for keeping the parallelogram

linkage at the equilibrium position. HP 6825A amplifier provide the power to drive DC motor. The output signal of the Hall Effect sensor is quasi-proportional to the angular displacement of the parallelogram linkages, and this signal is connected to output channel of the signal analyzer.

By setting the coefficient of the viscous friction for the shaft of parallelogram linkage as

$$b_{1,p} = 0.33 \, (N \sec/rad)$$
 (4.2.1)

and using periodic chirp of amplitude 0.4 volts for excitation, the experimental and the theoretical results are matched to each other well in Figure 4.2.2. In this Figure it shows when the frequency of the excitation goes beyond 0.8 Hz, the amplitude of the response is nearly zero and the noise become dominant, then the measurements are not reliable. By the plotting of coherence shown in Figure 4.2.3, this coherence is very low when the frequency goes below about 0.06 Hz. That means at this frequency region, the system nonlinearity become dominant. It is why the theoretical result can not predict the behavior very well at the very low frequency region.

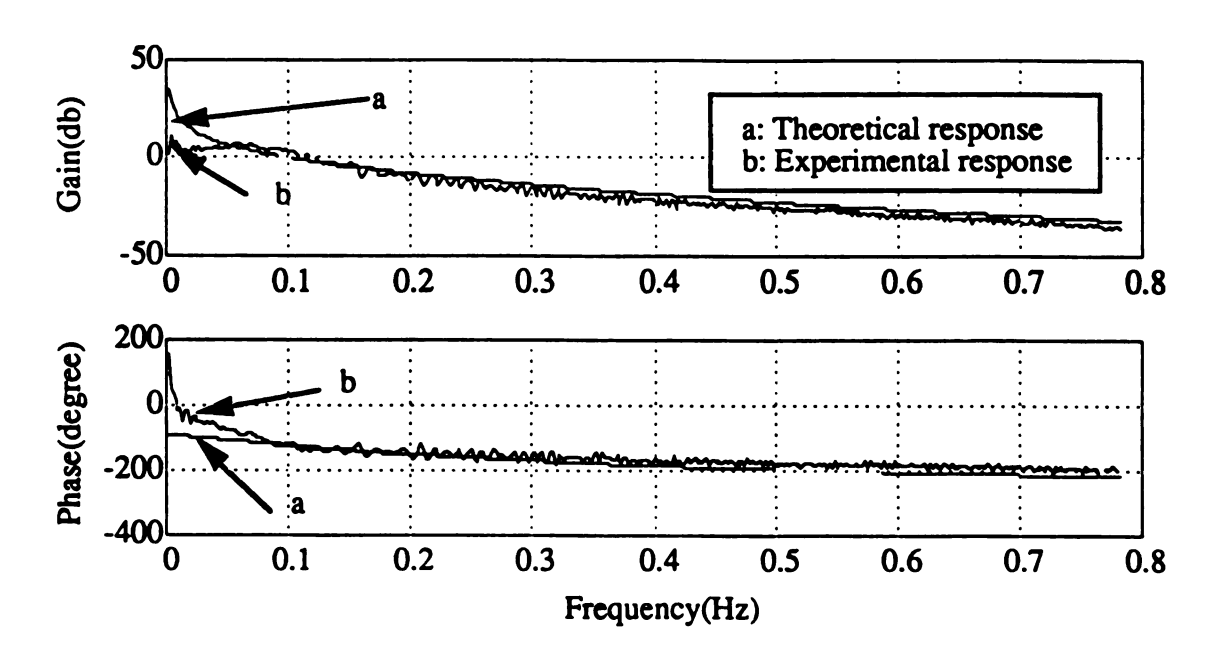


Figure 4.2.2 Experimental and theoretical Frequency Response

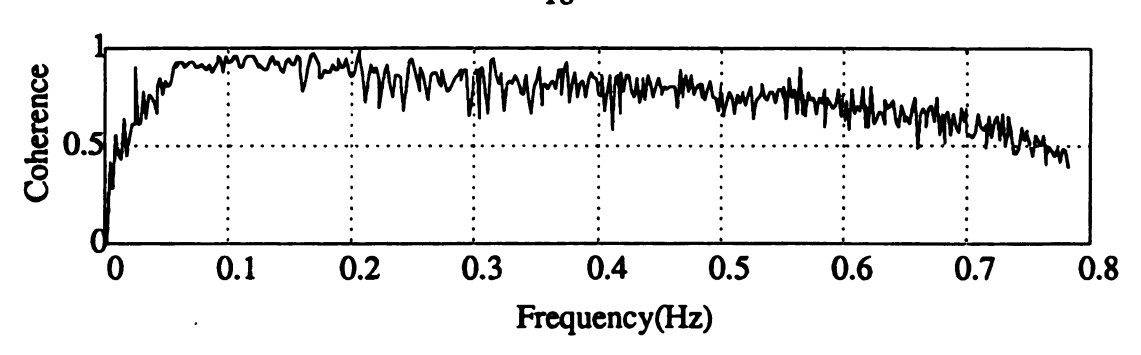


Figure 4.2.3 Coherence of the Frequency Response

#### 5 MODELING FOR CONTROL DESIGN

#### 5.1 Linear State Variable Model

In the linear state model (4.1.2), several parameter variations involved in this model. Generally, they can be divided into two groups. In the first group, the uncertainties arise from system parameter variation. These parameters are

- (1) Motor armature resistance  $R_a$
- (2) Coefficient of the viscous friction  $b_1$
- (3) Torque and Back EMF constant,  $K_{\tau}$  and  $K_{\nu}$
- (4) Slope of the hall Effect output equation (3.5.3),  $K_H$

Compared to those involved in nonlinear state variable model, Coulomb friction is not included here because this terms will eliminated after linearization.

The second group is from nonlinearity and variation associated with the thrust and torque which have the nonlinear characteristics and parametric variation arising from

- (1) Lift curve slope, a
- (2) Pitch angle,  $\theta_p$

# 5.2 Effect of Physical model parameter variations on linear model parameter variations

The uncertainty for  $R_a$  can be obtained by applying the statistic Hard Bound method [5] on the static measurements (see appendix A.2.4) by assuming uniform distribution over the uncertainty interval, thus

$$R_{a,0} = 2.25 \ (ohm), R_a \in [2.10, 2.40]$$
 (5.2.1)

where  $R_{a,0}$  is the nominal DC motor armature resistance and subscript "0" denotes the nominal value.

The uncertainties of  $K_{\tau}$ ,  $K_{\nu}$ ,  $b_1$ , a and  $\theta_p$  are approximated by 5% of their nominal values (see Appendix A.3)

# 5.3 Effect of Physical model nonlinearity on linear model parameter variations

In addition to the above three parametric uncertainties, in fact we neglect the nonlinearity due to linearization. In order to include the nonlinearity variation in the linear model, here we introduce "Conic Sector Bound" method [6].

#### The Conic Sector Bound Method

Given The nonlinear function  $f(\tilde{x})$  that is Lipschitz, where  $\tilde{x}$  is  $n \times 1$  vector

Find  $\bar{k}$  and  $\underline{k}$  such that there exists a vector  $\tilde{k}$  that can represent this nonlinear function as  $f(\tilde{x}) = \tilde{k} \ \tilde{x}$  within the compact domain  $D_1$ ,  $(\forall \ \tilde{x} \in D_1)$ , and this  $\tilde{k}$  has the bound

$$\underline{k}_i \leq \tilde{k}_i \leq \overline{k}_i$$

where  $\bar{k}$ ,  $\underline{k}$ , and  $\tilde{k}$  are all  $1 \times n$  vectors.

The strategy to solve this problem is that first we grid the compact domain  $D_1$  and take the finite number (relatively large enough) of sample points in  $D_1$ . If the nonlinear function is known to be Lipschitz [9], then for every single sample point by minimizing the 2-norm of the vector  $\tilde{k}$ , we can find the most conservative  $\tilde{k}$  to predict the nonlinear function. Secondly, comparing these all values of  $\tilde{k}$  resulting from every single point in , we choose the maximum of all upper bounds as a new upper bound and the minimum of all lower bounds as a new lower bound.

In order to apply Conic Sector Bound method, the equations used to predict the thrust produced and the torque required to drive the rotor are assumed to have the following forms for deriving Conic Sector Bounds.

$$T(\dot{\theta},\omega) - T(\dot{\theta}_{0},\omega_{0}) = (T_{\dot{\theta}}^{0} + k_{11})\dot{\theta} + (T_{\omega}^{0} + k_{12})(\omega - \omega_{0}) = \alpha_{11}\dot{\theta} + \alpha_{12}(\omega - \omega_{0})$$

$$\tau(\dot{\theta},\omega) - \tau(\dot{\theta}_{0},\omega_{0}) = (\tau_{\dot{\theta}}^{0} + k_{21})\dot{\theta} + (\tau_{\omega}^{0} + k_{22})(\omega - \omega_{0}) = \alpha_{21}\dot{\theta} + \alpha_{22}(\omega - \omega_{0})$$
(5.3.1)

where 
$$T_{\dot{\theta}}^{0} = \frac{dT}{d\dot{\theta}}$$
  $T_{\omega}^{0} = \frac{dT}{d\omega}$   $\tau_{\dot{\theta}}^{0} = \frac{d\tau}{d\dot{\theta}}$   $\tau_{\omega}^{0} = \frac{d\tau}{d\omega}$ 

Because the above four nominal derivatives can be calculated. The remaining unknowns in (5.3.1) are

$$k_{11}, k_{12}$$
 or  $\alpha_{11}, \alpha_{12}$  for Thrust  
 $k_{21}, k_{22}$  or  $\alpha_{21}, \alpha_{22}$  for Torque (5.3.2)

By minimizing the weighted 2-norm of

 $kDk^{T} (5.3.3)$ 

where

$$\mathbf{D} = \begin{bmatrix} d_1 & 0 \\ 0 & d_2 \end{bmatrix}$$

$$k = [k_{11}, k_{12}] or [k_{21}, k_{22}]$$

and using the form of (5.3.1), we can find Conic Sector Bounds for the nonlinear function. Note that the weighting matrix can be determined arbitrarily in order to obtain physically reasonable Conic Sector Bounds.

Within the reasonable compact domain

$$D = \left\{ (\dot{\theta}, \omega) : |\dot{\theta}| \le 2,600 \ RPM \le \omega \le 1400 \ RPM \right\}$$
 (5.3.3)

,we consider the nonlinearity of the thrust and torque and the parametric uncertainties arising form a and  $\theta_p$ , Conic Sector Bounds are found by using the particular weighting that make the system stable. These Bounds are shown in Table 5.3.1.

# 5.4 Effect of Physical model parameter measurements on linear model parameter variations using Conic Sector Bound method

In addition to nonlinearity, we also use this Conic Sector Bound method to accommodate the measurement uncertainty in linear variable model.

Table 5.3.1 The Conic Sector Bounds for three different models

weigh	ting	O	ζ <sub>11</sub>	O	
	$\frac{d_2}{d_1}$	$\underline{\alpha}_{11}$	$\overline{\alpha_{_{11}}}$	$\underline{lpha_{\scriptscriptstyle 12}}$	$\overline{lpha_{_{12}}}$
Cubic	30	-1.71x10 <sup>-1</sup>	-9.14x10 <sup>-2</sup>	1.25x10 <sup>-2</sup>	2.47x10 <sup>-2</sup>
Linear	30	-1.87x10 <sup>-1</sup>	-9.90x10 <sup>-2</sup>	1.13x10 <sup>-2</sup>	2.65x10 <sup>-2</sup>
Uniform	30	-2.10x10 <sup>-1</sup>	-1.34x10 <sup>-1</sup>	1.01x10 <sup>-2</sup>	2.73x10 <sup>-2</sup>

weighting			$lpha_{\scriptscriptstyle 21}$		$\alpha_{2}$	
	$\frac{d_2}{d_1}$	$\underline{\alpha_{\scriptscriptstyle 21}}$	$\overline{\alpha_{_{21}}}$	$\underline{\alpha_{22}}$	$\overline{\alpha_{22}}$	
Cubic	20	-2.05x10 <sup>-3</sup>	4.43x10 <sup>-4</sup>	1.25×10 <sup>-4</sup>	3.05x10 <sup>-4</sup>	
Linear	20	-1.47x10 <sup>-3</sup>	1.42x10 <sup>-3</sup>	1.95x10 <sup>-4</sup>	3.72×10 <sup>-4</sup>	
Uniform	20	-1.83x10 <sup>-3</sup>	1.25x10 <sup>-3</sup>	1.77x10-4	3.58x10 <sup>-4</sup>	

For the uncertainty associated with  $K_H$ , it can be calculated by treating the finite number of experimental measurements as the nonlinear function values and applying the above Conic Sector Bound method. Thus this uncertainty can be found as

$$V_H = K_H \theta$$
,  $K_H \in [0.0200, 0.0250]$  (5.4.1)

### 6 CONTROL DESIGN

The dynamics of the parallelogram linkage is heavily influenced by the parameter variations. One method introduced by Morari and Zafiriou [7] uses the IMC controller to minimize the effect of model uncertainty. This IMC structure is shown in Figure 6.0.1.

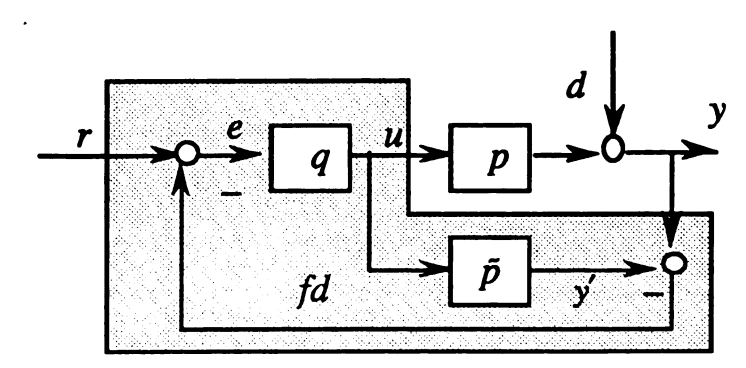


Figure 6.0.1 The IMC structure

Here p denotes the plant and  $\tilde{p}$  the nominal models.  $r_i$ , r' and w are physical input, normalized input and weighting function respectively. q is IMC controller.

By comparison between the classic feedback controller structure and the IMC structure shown in Figure 6.0.1, the performance achievable with IMC is identical to that achievable with the classic feedback controller  $c_c$  shown selected such that

$$c_c = \frac{q}{1 - \tilde{p}q} \tag{6.0.1}$$

The IMC controller design contain two steps. In the first step the controller  $\tilde{q}$  is selected for good response without regard for constraint and model uncertainty; that is

$$\bar{q} = \frac{1}{\bar{p}} \tag{6.0.2}$$

Note that our model inverse is an acceptable solution because the linear model (4.1.2) is minimum-phase plant.

In the second step for satisfying the robustness requirement the controller  $\tilde{q}$  is augmented by a low-pass filter f

$$q = \tilde{q}f \tag{6.0.3}$$

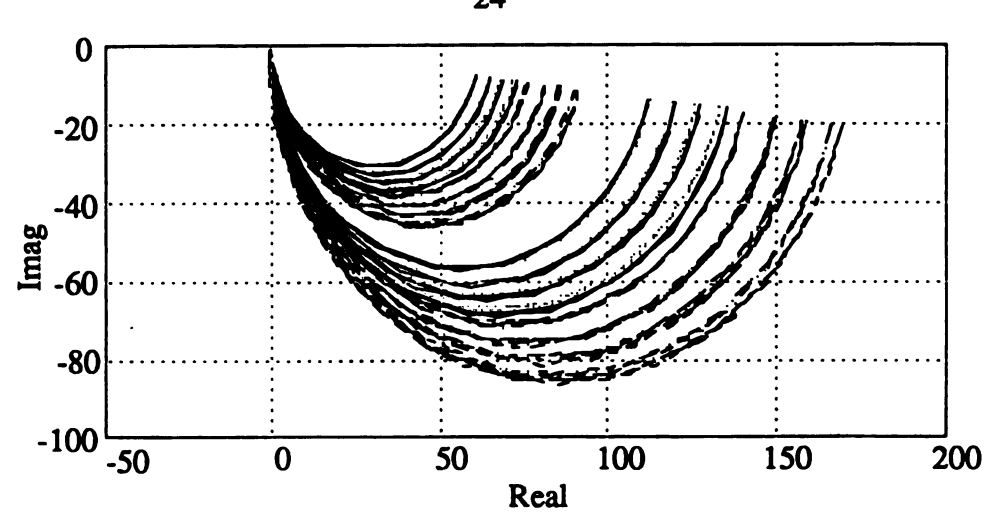


Figure 6.1.1 Fuzzy Nyquist plot for cubic model

to provide the roll-off necessary for robustness and milder action of the manipulated variable. If it is designed for asymptotically constant inputs (step input), then

$$f = \frac{1}{(\lambda s + 1)^3} \tag{6.0.4}$$

This filter can make q proper in order to be causal.

#### 6.1 Parametric Uncertainty

Parametric uncertainty representation describes the model by using the linear state variable model (4.1.2) and letting all uncertain parameters vary in their associated uncertain interval including Conic Sector Bounds. The Fuzzy Nyquist in Figure 6.1.1 shows all these various linear models which use cubic velocity distribution assumption.

Using the nominal linear model (4.1.2) as nominal plant to design the IMC controller q, we plot the local Nyquist band of  $p(i\omega)c_c(i\omega)$  near to (-1,0) with  $\lambda$  from 0.05 to 10 in Figure 6.1.2, which will never encircle or cover (-1,0) so that the closed-loop system is guaranteed to be stable. By plotting Nyquist bands of  $p(i\omega)c_c(i\omega)$  for the other two models, the results also shows  $p(i\omega)c_c(i\omega)$  does not cover (-1,0).

The sensitivity function  $\varepsilon$  is defined as

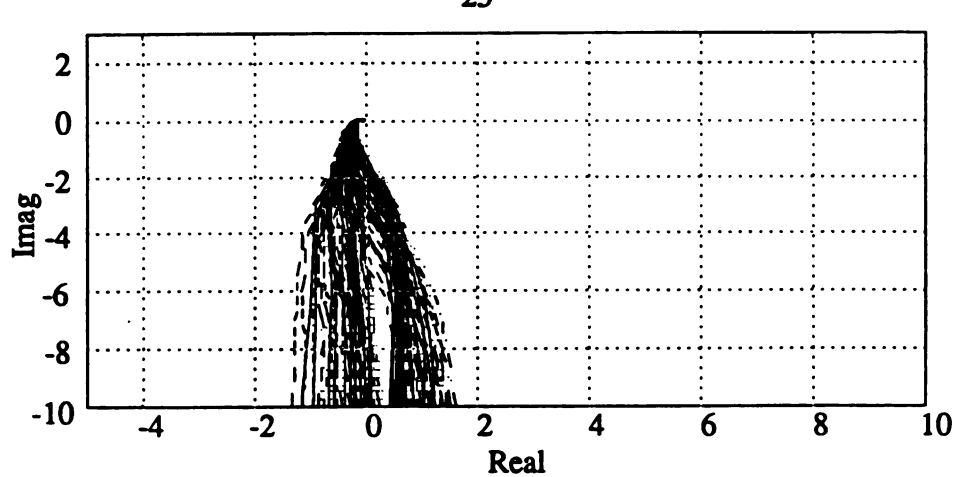


Figure 6.1.2 Local Plot of  $p(i\omega)c_c(i\omega)$  for cubic model

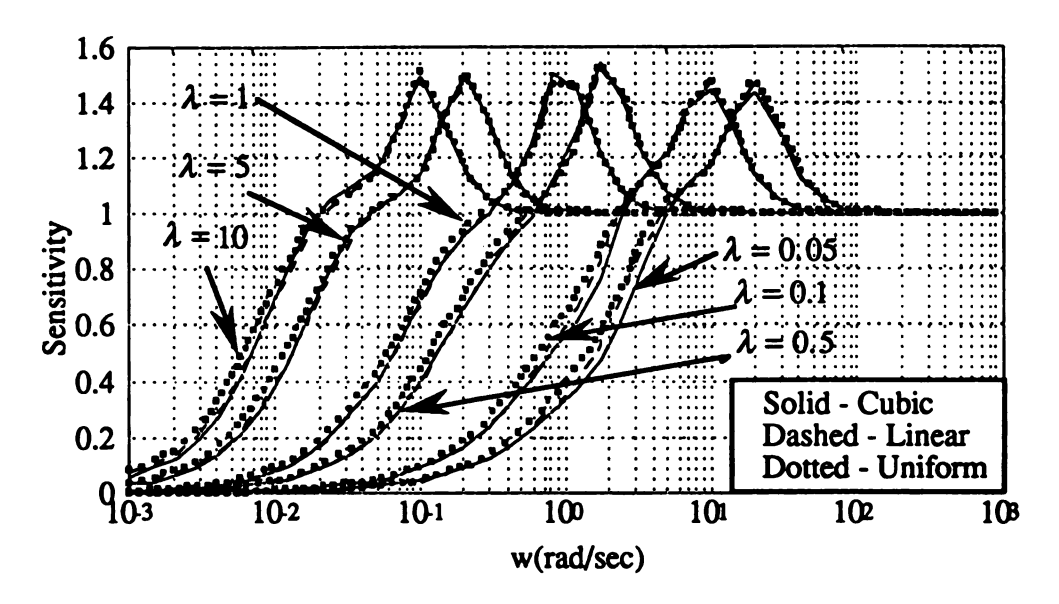


Figure 6.1.3 Upper bounds of the sensitivities for parametric representation

$$\varepsilon = \frac{1}{\left(1 + pc_{c}\right)},\tag{6.1.1}$$

In [7] the robust performance requires that the distance from all possible  $p(i\omega)c_c(i\omega)$  to the point (-1,0), i.e.,  $|1+pc_c|$  has to exceed the specified maximum weighting function w. By using the information revealed in the Fuzzy Nyquist plot of Figure 6.1.2 or the other plot of  $p(i\omega)c_c(i\omega)$  for the other two models, we find out the upper bounds of the sensitivity functions shown in Figure 6.1.3 for three different distribution models. It

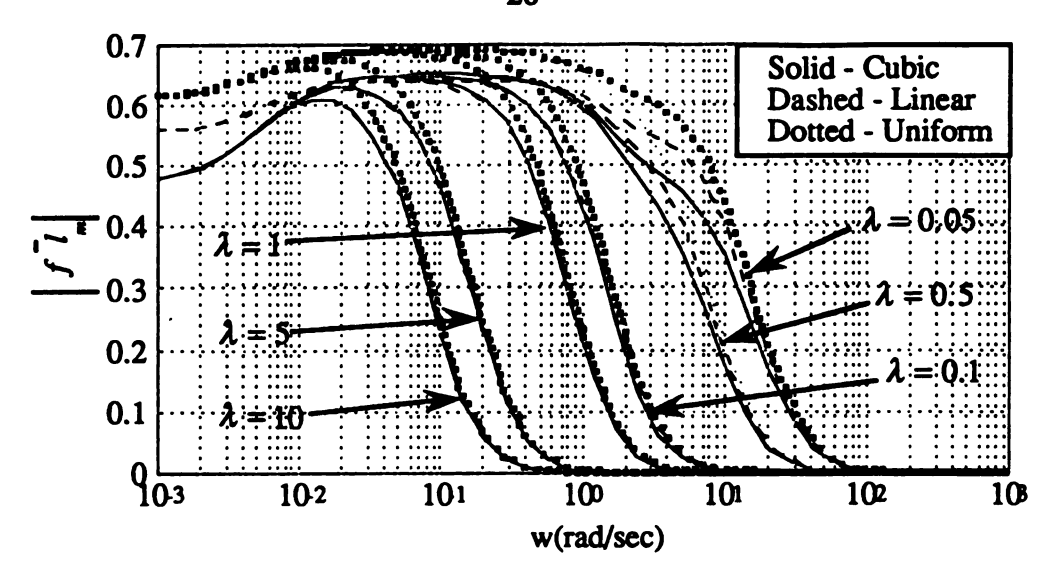


Figure 6.2.1 Robust stability consideration

appears that the bounds derived from three different models are almost identical to each other. The upper bounds of the weighting functions can be obtained by the inverses of the preceding sensitivity bounds.

#### 6.2 Nonparametric Uncertainty

In nonparametric representation, the family  $\Pi$  shown in Nyquist domain, which represent all possible plants p, can be enclosed by a disk defined by

$$\Pi = \left\{ p: \frac{\left| p(i\omega) - \tilde{p}(i\omega) \right|}{\tilde{p}(i\omega)} \le \bar{l}_{m}(\omega) \right\}$$
(6.2.1)

where  $\bar{l}_m$  is referred to as an multiplicative uncertainty and  $\bar{p}(i\omega)$  is the nominal plant or the model defining the centers of all the disk shaped regions, which is used to design IMC controller q.

In [7], it suggests that for nonparametric representation, if the values of  $|f\bar{l}_m|$  never exceed one over all frequency domain, the closed-loop system is guaranteed to be robustly stable. Figure 6.2.1 shows that the values of  $|f\bar{l}_m|$  never exceeds one over all physical reasonable frequency domain so that the closed-loop system is robustly stable.

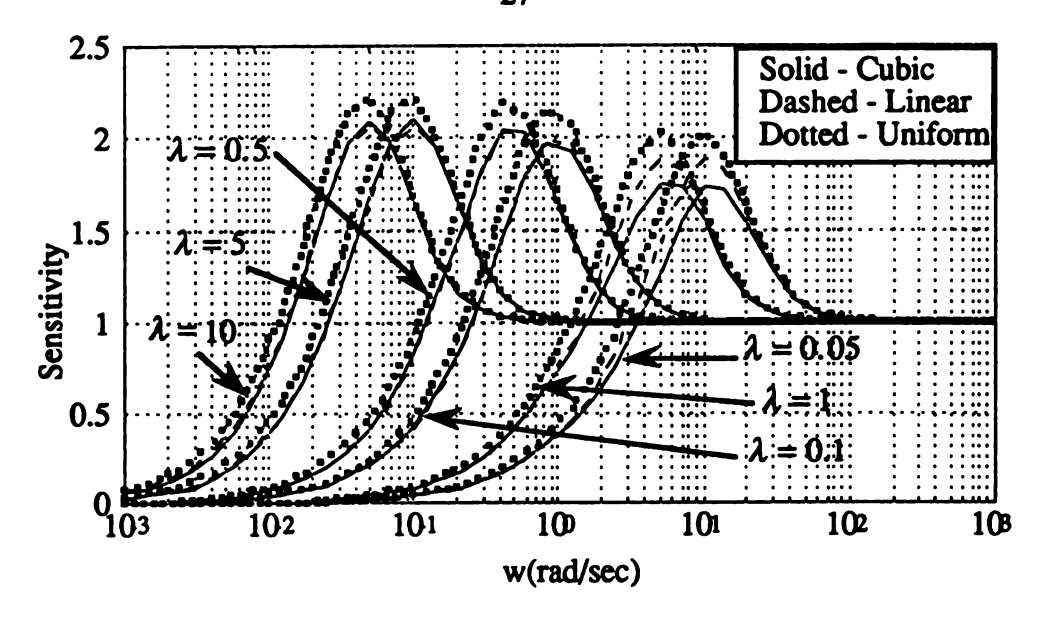


Figure 6.2.2 Upper bounds of the sensitivity functions

The robust performance criterion also can be given by

$$|f\bar{l}_m| + |(1-f)w| < 1$$
 (6.2.2)

The above equation can be used to derive the upper bounds of weighting functions and sensitivity functions which are shown in Figure 6.2.2.

#### 6.3 Comprehensive Uncertainty

For the case of the comprehensive uncertainty representation we consider that the model must be able to represent the dynamics that could arise from any of the three linear variable models (differing by inflow distributions). Two controllers result from comprehensive uncertainty. The first one, called "Comprehensive parametric representation," uses the nominal plant that has associated nominal parameters with uncertainties which can represent all uncertainties arising from any of three models. The second one called, "Comprehensive nonparametric representation," uses nominal plant that is the centers of uncertainty disks in Nyquist domain, which encircle the uncertainty arising from any of three models.

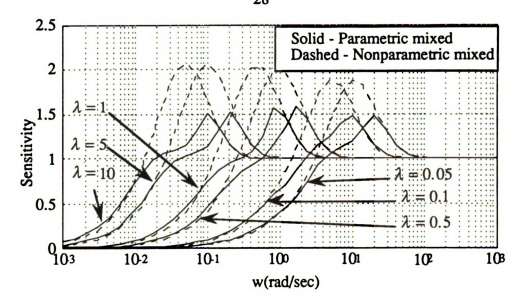


Figure 6.3.1 Upper bounds of sensitivity fuctions for comprehensive representation

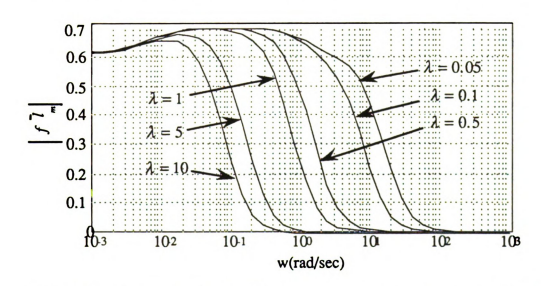


Figure 6.3.2 Robust consideration for "Comprehensive nonparametric representation"

Using the same previous criterions, for the case of "Comprehensive parametric representation,"  $p(i\omega)c_c(i\omega)$  still not encircle (-1,0) and the sensitivities are shown in Figure 6.3.1 to be smaller than "comprehensive-nonparametric" ones.

For the case of "Comprehensive nonparametric representation," the values of  $|f\bar{I}_{\bf m}|$  shown in Figure 6.3.2 does not exceed one so that the closed-loop system with this controller still be robustly stable.

#### 6.4 Nominal Plants Used for Robust Control Design

Eight nominal plants used for robust control design are plotted in Figure 6.4. These nominal plants are derived based on the uncertainties of

- (a) Parametric representation and Cubic model. The nominal plant is the linear nominal planet of the cubic model.
- (b) Parametric representation and Linear model. The nominal plant is the linear nominal plant of the linear model.
- (c) Parametric representation and Uniform model. The nominal plant is the linear nominal plant of the uniform model.
- (d) Comprehensive parametric representation. The nominal plant is the average of the above three nominal plants
- (e) Nonparametric representation and Cubic model. The nominal plant is the centers of uncertainty disk in Nyquist domain for the cubic model
- (f) Nonparametric representation and Linear model. The nominal plant is the centers of uncertainty disk in Nyquist domain for the linear model
- (g) Nonparametric representation and uniform model. The nominal plant is the centers of uncertainty disk in Nyquist domain for the uniform model
- (h) Comprehensive nonparametric representation. The nominal plant is the centers of uncertainty disk in Nyquist domain. This uncertainty can arise from any of the above three uncertainty linear models

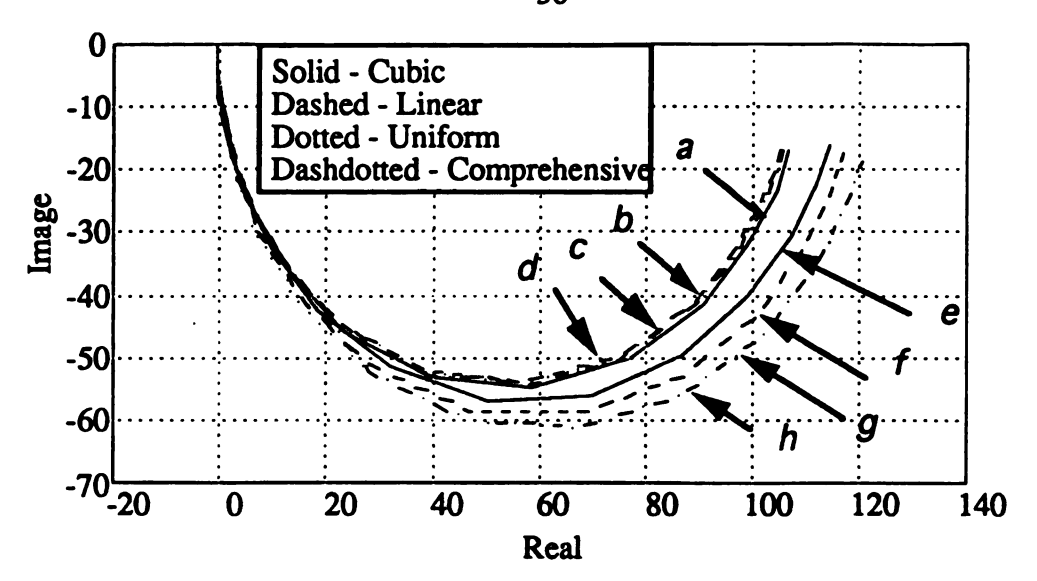


Figure 6.4 Nominal plants

#### 7 EVALUATION

We used the nonlinear state variable model (3.5.1) instead of linearized model and unit output feedback structure for simulation. The IMC filter with  $\lambda = 0.1$  or  $\lambda = 0.2$  was realized by controller canonical form [10]. The applicable eight different robust controller which use the nominal plant shown in Figure 6.4. The control effort was the sum of the output of the IMC filter and the nominal voltage supply that can keep the system at the equilibrium position when the feedback signal is zero. The simulation algorithm was using 4th and 5th order Runge-Kutta formulas which has tolerance set under 1e-5.

#### 7.1 How is the Worst-Case Determined

In order to define the worst case, we introduce an performance index called 2-norm which is

$$\|e(t)\|_{2}$$

$$= \sqrt{\int_{t_{0}}^{t_{f}} |e(t)|^{2} dt}$$

$$\approx \sqrt{\sum_{i=0}^{n-1} \left(\frac{e(t_{i})^{2} + e(t_{i+1})^{2}}{2}\right) \Delta t}$$
(7.1)

where

 $e_i = y_i - y_{ss}$ 

 $\Delta t$  = Sample time interval = 0.1 sec

y = Time response trace

 $y_{ss}$  = Steady state

Using this 2-norm definition, the worse case occurs when 2-norm error reaches its maximum value. While using the three nonlinear state variable models (3.5.1), in addition to considering possible plants due to the parametric uncertainties, which result from lift curve slope, pitch angle, DC motor armature resistance, torque constant, viscous friction and Hall Effect sensor, we add the uncertainties of 5% of the Coulomb friction into

	Controller a	Controller b	Controller c	Controller d
100	13.7233 * <i>l</i>	13.7111 *u	13.7273 *l	13.6879 * <i>l</i>
200	29.6059 * u	29.5788 *u	29.5314 *c	29.5289 *1
30°	56.4482 *u	56.4871 *u	56.4803 * <i>l</i>	56.2301 *u

Table 7.2.1 Worst-case 2-norms for the cases with IMC filter which has  $\lambda = 0.1$ 

	Controller e	Controller f	Controller g	Controller h
100	14.6214 * <i>l</i>	14.4197 * <i>l</i>	14.0989 *l	15.5336 *l
200	30.4191 *u	30.1712 *u	30.0410 *u	31.8937 * <i>l</i>
30o	51.8027 *u	52.4556 *u	55.1732 *u	50.8499 *u

<sup>\*</sup> Note that c, u, or l represent the worst case is corresponding to cubic, linear or uniform model respectively.

account. Using line search method [11], we search for the worst-case responses with respect to each controller.

# 7.2 Worst-case responses for different robust controllers and the associated models

In simulation, for each controller we search for worse case and the associate 2-norms which might corresponding to any of velocity model or system parameter. The reference signal is set to be the step input which is some certain degree during the 10 sec and 0° in the remaining 10 second. The simulation result shows that the worst-case parameters are always boundary parameters and these parameters are dependent on the inflow velocity distribution but independent of the controller used. Table 7.2.1 and Table 7.2.2 list the worst-case 2-norms for each controller, which are corresponding to different IMC filters.

Table 7.2.2 Worst-case 2-norms for the cases with IMC filter which has  $\lambda=0.2$ 

	Controller a	Controller b	Controller c	Controller d
100	18.7924 * <i>l</i>	18.8056 *u	18.7924 * <i>l</i>	18.7664 * <i>l</i>
200	38.2131 * u	38.2131 *u	37.9692 *c	37.8170 * <i>l</i>
30o	58.8725 <b>*</b> u	58.7634 *u	58.5773 <b>*</b> l	58.4899 <b>*</b> u

	Controller e	Controller f	Controller g	Controller h
10°	20.1400 *1	19.8789 * <i>l</i>	19.5240 * <i>l</i>	21.0060 *1
200	40.9684 *u	40.4430 *u	39.7484 *u	42.6154 *1
300	63.0479 <b>*</b> u	62.2680 *u	61.2601 *u	65.4545 *u

<sup>\*</sup> Note that c, u, or l represent the worst case is corresponding to cubic, linear or uniform model respectively.

Form Table 7.2.1 with  $\lambda = 0.1$ , in 2-norm sense, the controller d derived from the comprehensive parametric uncertainty is proved better than the others for the smaller step input (e.g.  $10^{\circ} 20^{\circ}$ ) but for larger step input (e.g.  $30^{\circ}$ ), the controller h derived from comprehensive nonparametric uncertainty is proved better. Form Table 7.2.2 with  $\lambda = 0.2$ , in 2-norm sense, the controller d derived from the comprehensive parametric uncertainty is proved better than the others for different kinds of input

In Figure 7.2.1, using the step input 30° we plot the eight worst-case traces corresponding to eight controllers with  $\lambda = 0.1$ . It indicates that the upward motion is absolutely different from the downward motion. Figure 7.2.2 shows the same worst-case responses but with  $\lambda = 0.2$ .

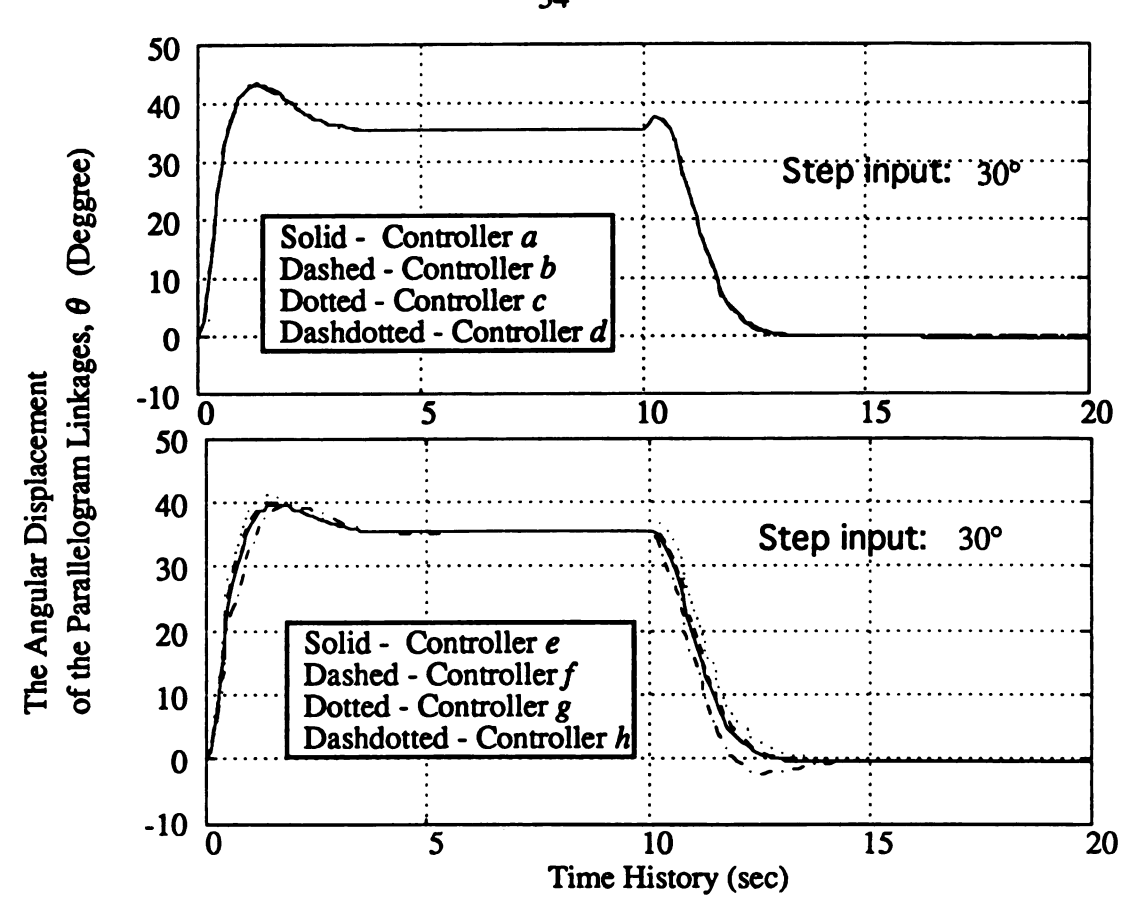


Figure 7.2.1 Worse-case response for 30° input with  $\lambda = 0.1$ 

Figure 7.2.3 shows the time trace of the control effort; i.e., the output voltage of the IMC filter for the worst-case for the input  $30^{\circ}$  with  $\lambda = 0.2$ . It indicates that the amplifier used for implementation have to be powerful enough to generate as high as about sum of peak of output voltage of IMC filter, 10 Volts and nominal voltage about 6 Volts.

Figure 7.2.4 shows the time traces corresponding to rotor speed using IMC filter with  $\lambda = 0.1$ . Obviously, the rotor speed is out of reasonable physical range

$$\{\omega:600RPM \le \omega \le 1400RPM\} \tag{7.2.1}$$

which is the one we used to derive the Conic Sector Bounds. Figure 7.2.4 shows rotor speed will always in the physical range if we use IMC filter with  $\lambda = 0.2$ .

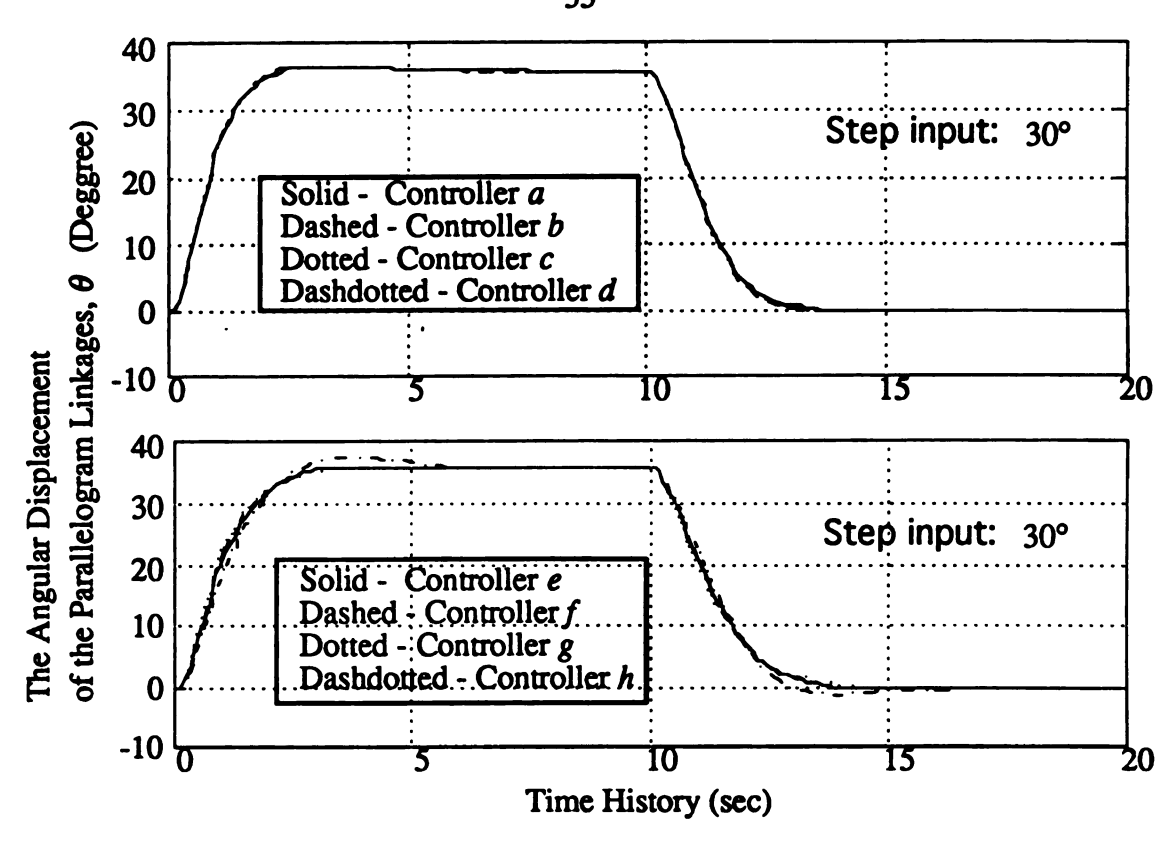


Figure 7.2.2 Worse-case response for 30° input with  $\lambda = 0.2$ 

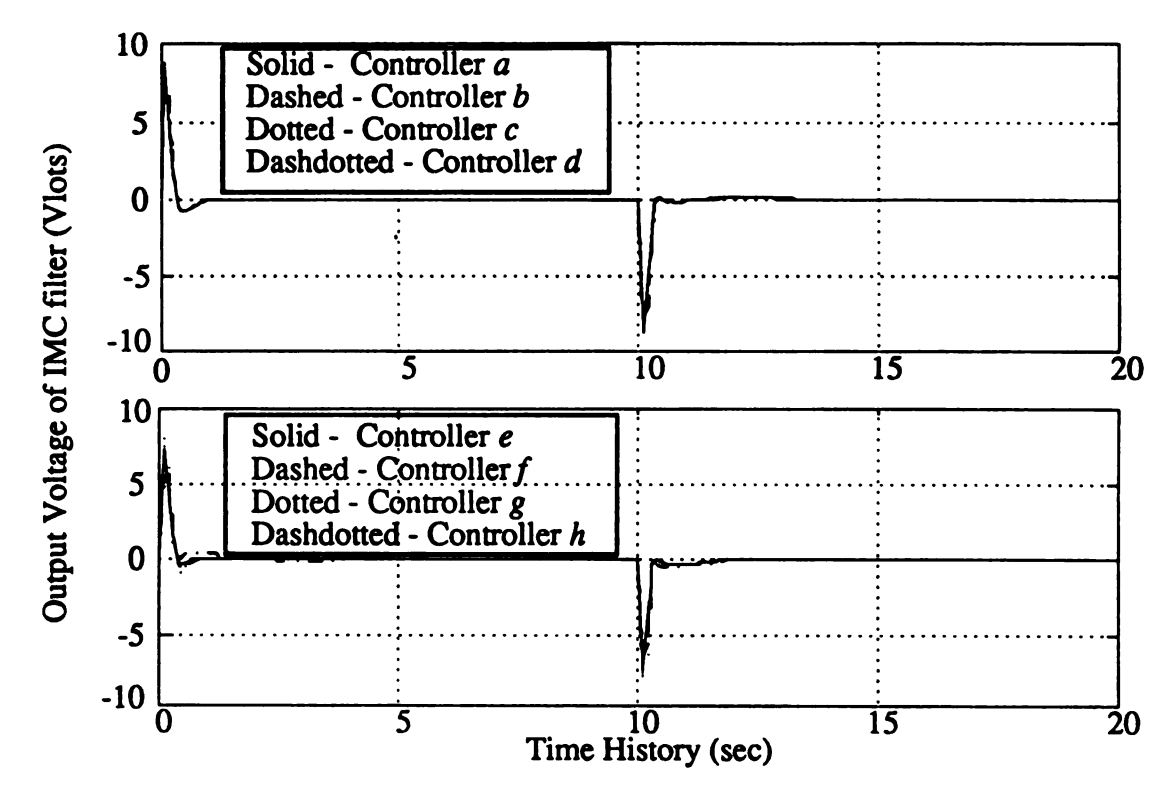


Figure 7.2.3 Control effort for input 30° with  $\lambda = 0.2$ 

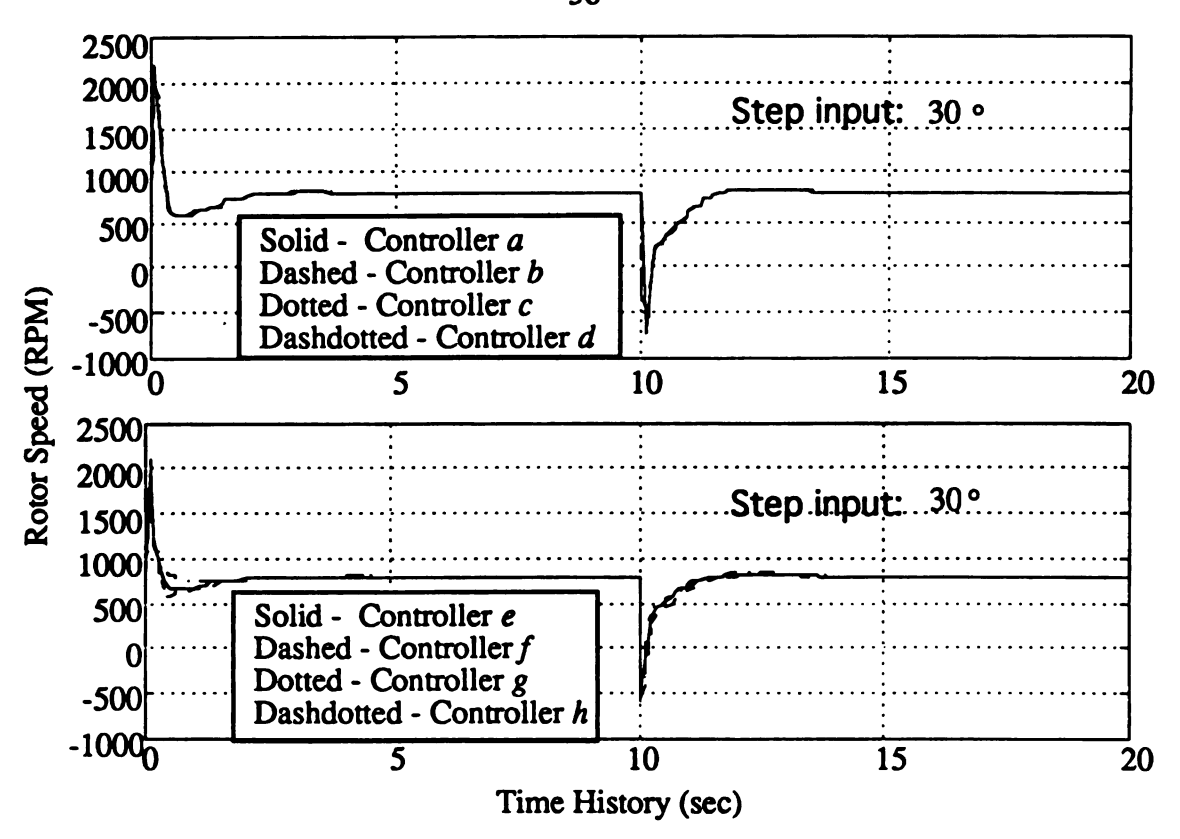


Figure 7.2.4 Rotor speed for input 30° with  $\lambda = 0.1$ 

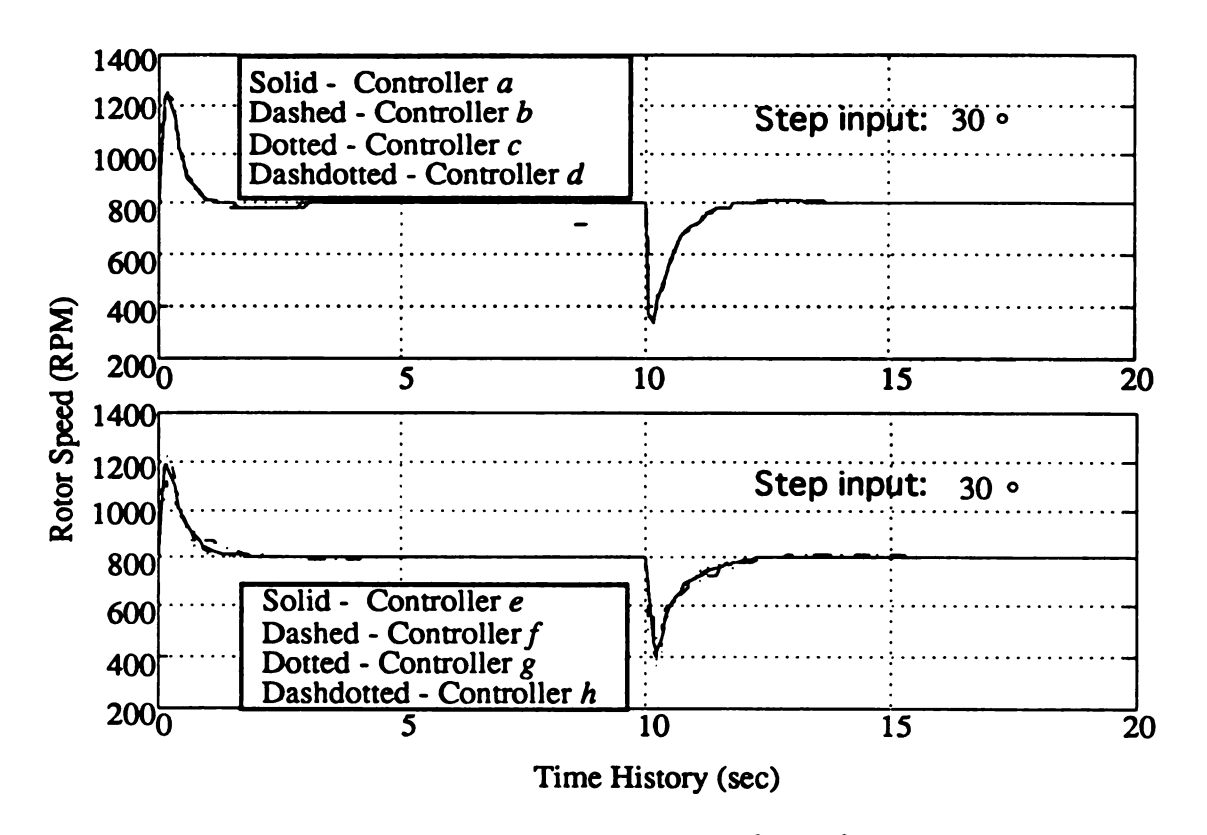


Figure 7.2.5 Rotor speed for input 30° with  $\lambda = 0.2$ 

#### 8. CONCLUSION

The physical system was described by a nonlinear model. This nonlinear model is able to predict the dynamics of drive train, parallelogram linkage and the thrust produced and the torque required by the rotor.

We modeled a nonlinear system using the framework of Uncertain Linear System which has the uncertainty that results from parametric uncertainty or Conic Sector Bounds. By using this ULS, we can investigate the effect of three different inflow velocity distributions on both the uncertain linear system and the control design. It was found that for small parameter variations, the effect of inflow velocity distribution assumed was not very significant.

Eight robust controllers were designed to minimize the effect of the uncertainty. They are designed using parametric, nonparametric and comprehensive uncertainty representation for three different velocity distribution models. The stability analysis shows that the closed-loop system is stable for any controller. A time domain analysis including simulation and the 2-norm error calculation were completed. The worst case always occurs for the plant with the boundary parameters. The simulation results shows that using the reasonable IMC filter with  $\lambda = 0.2$ , the controller design using comprehensive parametric uncertainty yields better performance than the others.

#### REFERENCE

- [1] Benjamin C. UK, 1991, Automatic Control System, Prentice Hall, Englewood Cliffs, New Jersey.
- [2] J. Seddon, 1990, Basic Helicopter Aerodynamics, American Institute of Aeronautics and Astronautics. Inc., Washington D.C.
- [3] Donald M. Layton, 1984, *Helicopter Performance*, Matrix Publisher, Inc., Beaverton, Oregon.
- [4] HP 35660A Dynamic Signal Analyzer Getting Started Guide and Front-Panel Reference, 1988, Hewllet-Packard Company, Everette, Washington.
- [5] Bo Wahlberg and Lennart Ljung, 1992," Hard Frequency -Domain Model Error Bounds from Least-Square Like Identification Techniques," *IEEE Transaction on Automatic Control*, vol. 37, No. 37, pp. 900-912.
- [6] Anderson Broan, 1990, Optimal Control: Linear Quadratic Method, Prentice Hall, Englewood Cliffs, New Jersey
- [7] Manfred Morrari and Evanghelos Zafiriou, 1989, *Robust Process Control*, Prentice Hall, Englewood Cliffs, New Jersey.
- [8] Menu of Digital Force Gauge Model DFG, 1986, Chatillon Force Measurement, Greensboro, North Carolina.
- [9] Hassan K. Khalil, 1992, Nonlinear Systems, Macmillan, New York.
- [10] Wilson J Rugh, 1993, *Linear System Theory*, Prentice Hall, Englewood Cliffs, New Jersey.
- [11] Jasbir S. Arora, 1989, Introduction to Optimum Design, McGraw-Hill, New York.

#### **APPENDIX**

#### A.1 Mathematical Development

#### A.1.1 DC Motor Dynamics

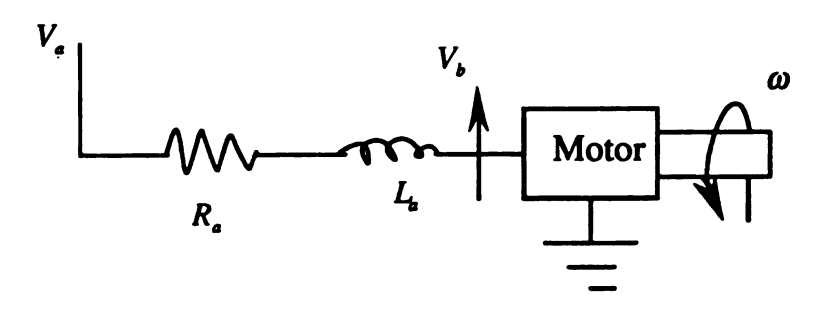


Figure A.1.1 Simplified model of a DC motor

In a running permanent magnet DC motor, the current  $i_a$  flows through the armature which has resistance  $R_a$ , inductance  $L_a$  and supply armature voltage  $V_a$ . Since the armature is a conductor rotating in a magnetic field, a voltage referred to as the back EMF.,  $V_b$ , is induced in the armature. A simple model shown in Figure A.1.1 describing this electric circuit is given by

$$V_{a} = V_{b} + L_{a} \frac{di_{a}}{dt} + R_{a}i_{a}$$
 (A.1.1.1)

The relationships governing the behavior of the gyrator portion of the model in Figure A.1 are given by

$$V_b = K_v \omega \tag{A.1.1.2}$$

$$\tau_{motor} = K_{\tau} i_a \tag{A.1.1.3}$$

where  $K_{\nu}$  is the back EMF constant,  $\omega$  is the rotor speed,  $\tau_{motor}$  is the output torque of the motor and  $K_{\tau}$  is the torque constant (Note that for convenience we have chosen the rotor speed as our reference speed and this will affect the values of  $K_{\nu}$  and  $K_{\tau}$ ). The term

 $L_a \frac{di}{dt}$  in (A.1.1.1) is small enough over the frequency range of interest to be considered zero. Therefore we can combine (A.1.1.1), (A.1.1.2), and (A.1.1.3) to find

$$\tau_{motor} = K_{\tau} \left( \frac{V_a - K_{\nu} \omega}{R_a} \right) \tag{A.1.1.4}$$

This motor torque balances the torque required to accelerate the drive train/rotor system, the torque required to drive the rotor blades through the air mass,  $\tau_{rotor}$ , and the torque resulting from friction in the drive train  $\tau_{friction}$ . This relationship is given by

$$K_{\tau} \left( \frac{V_a - K_v \omega}{R_a} \right) = J_r \dot{\omega} + \tau_{rotor} + \tau_{friction}$$
 (A.1.1.5)

#### A.1.2 Application of Momentum Theory for Rotor

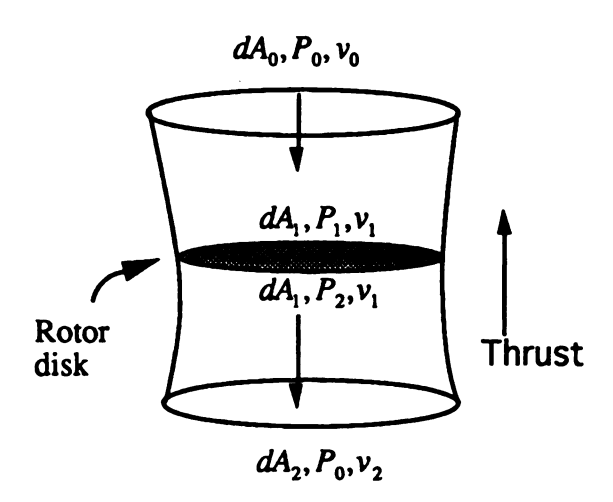


Figure A.1.2 Control Volume used in Momentum Theory

In Figure A.1.2, we show the control volume used for this analysis. The areas, pressures, and velocities shown in this Figure are defined below

 $dA_0$  = upstream cross-sectional differential area of the stream tube

= Cross-sectional differential area of the stream tube at the rotor disk

dA<sub>2</sub> = Downstream cross-sectional differential area of the stream tube

 $P_0$  = Atmospheric pressure

 $P_1$  = Pressure on upper side of the rotor disk

 $P_{\gamma}$  = Pressure on lower side of the rotor disk

 $v_0$  = Upstream velocity of the air flow relative to the rotor disk

 $v_1$  = Velocity of the air flow through the rotor disk

 $v_2$  = Downstream velocity of the air flow relative to the rotor disk

 $\rho$  = Air density

We assume that the air is incompressible and apply Bernoulli's equation to streamlines above and below the rotor disk and find

$$P_0 + \frac{1}{2}\rho v_0^2 = P_1 + \frac{1}{2}\rho v_1^2 \tag{A.1.2.1}$$

$$P_0 + \frac{1}{2}\rho v_2^2 = P_2 + \frac{1}{2}\rho v_1^2 \tag{A.1.2.2}$$

Subtracting (A.1.2.1) from (A.1.2.2) yields

$$\frac{1}{2}\rho(v_0^2-v_2^2)=P_1-P_2 \tag{A.1.2.3}$$

The Momentum Equation is given by

$$(P_2 - P_1)dA_1 = \rho v_2^2 dA_2 - \rho v_0^2 dA_0$$
 (A.1.2.4)

The Continuity Equation yields

$$v_0 dA_0 = v_1 dA_1 = v_2 dA_2 \tag{A.1.2.5}$$

Substituting (A.1.2.5) into (A.1.2.4), we have

$$(P_2 - P_1)dA_1 = \rho v_1(v_2 - v_0)dA_1$$
 (A.1.2.6)

Multiplying (A.1.2.3) by dA<sub>1</sub> leads to

$$(P_2 - P_1)dA_1 = \frac{1}{2}\rho(\nu_2 - \nu_0)(\nu_2 + \nu_0)dA_1$$
 (A.1.2.7)

Comparing (A.1.2.6) and (A.1.2.7), we find

$$v_2 = 2v_1 - v_0 \tag{A.1.2.8}$$

Substituting (A.1.2.8) into (A.1.2.6) we finally arrive at an expression for the differential thrust dT generated by the rotor

$$dT = (P_2 - P_1)dA_1$$

$$= \rho v_1(2v_1 - 2v_0)dA_1$$

$$= 2\rho v_1(v_1 - v_0)dA_1$$
(A.1.2.9)

Note that  $v_1$  is the inflow velocity distribution assumed to exist over the rotor disk.

#### A.1.3 Application of Blade Element Theory for Rotor

Blade Element Theory is introduced [2] here to find an alternative expression for the thrust and torque that are dependent on the rotor geometric design. In order to develop this expression, certain terms used in 2-D airfoil theory are shown in Figure A.1.3 below.

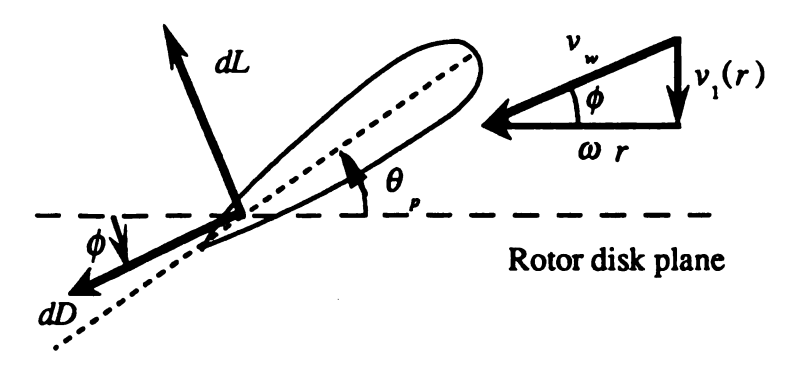


Figure A.1.3 2-D Airfoil Terms for a Rotor Blade Section

Recalling from 2-D airfoil theory the drag and lift forces are dependent on the square of the resultant wind velocity  $v_w$ . We can write the differential lift and drag equations as

$$dD = \frac{1}{2} \rho v_{w}^{2} (C_{D}c) dr$$
 (A.1.3.1)

$$dL = \frac{1}{2} \rho v_{w}^{2} (C_{L}c) dr$$
 (A.1.3.2)

where d represent the differential notation. D and L are the drag and the lift force, respectively. Note that dD is parallel and dL is perpendicular to the relative wind  $v_w$ .

The lift coefficient is approximated well (as long as the section is within stall limits) by

$$C_L = a\alpha \tag{A.1.3.3}$$
 where  $a = \text{Lift curve slope}$  
$$\alpha = (\theta - \phi) = \text{Angle of attack}$$

The inflow angle (in Fig A.1.3)  $\phi$  is typically small so that it can be approximated by

$$\phi = \tan^{-1} \left( \frac{v_1}{\omega r} \right) \approx \frac{v_1}{\omega r} \tag{A.1.3.4}$$

and the resultant wind velocity can be approximated by

$$v_{\perp} \approx \omega r$$
 (A.1.3.5)

Here  $v_1$  is the inflow wind velocity, r, refers to the radial position on the rotor blade, and  $\omega$  is the angular speed of the rotor.

The angle of attack is the difference between the pitch angle  $\theta_p$  and the inflow angle  $\phi$ .

$$\alpha = \theta_{p} - \phi \tag{A.1.3.6}$$

By substituting (A.1.3.3), (A.1.3.4), (A.1.3.5) and (A.1.3.6) into (A.1.3.2), the differential lift on a blade element becomes

$$dL = \frac{1}{2}\rho\omega^2 r^2 ac \left(\theta_p - \frac{v_1}{\omega r}\right) dr$$
 (A.1.3.7)

Since dD is very small relative to dL, the differential thrust dT is well approximated by differential lift dL well. Thus

$$dT \approx \frac{1}{2}\rho\omega^2 r^2 ac \left(\theta_p - \frac{v_1}{\omega r}\right) dr$$
 (A.1.3.8)

The torque required to drive the blade element through the air mass can be approximately produced by the component of the lifting force dL in the rotor disk plane normal to the blade centerline. Therefore

$$d\tau_{rotor} = r\sin(\phi) dL = r\phi dL = \frac{v_1}{\omega} dL \qquad (A.1.3.9)$$

Substituting (A.1.3.7) into (A.1.3.9), we find

$$d\tau_{rotor} = \rho ac(\omega r^2 \theta_{p} v_1 - r v_1^2) dr \qquad (A.1.3.10)$$

The differential thrust (A.1.3.8) and torque (A.1.3.10) are used to derive net thrust and torque.

### A.1.4 Linearization

$$\dot{\mathbf{x}} = \mathbf{A}\mathbf{x} + \mathbf{B}\mathbf{u}$$

$$\mathbf{y} = \mathbf{C}\mathbf{x}$$
(4.1.2)

where 
$$\mathbf{A} = \begin{bmatrix} 0 & 1 & 0 \\ a_{21} & a_{22} & a_{23} \\ 0 & a_{32} & a_{33} \end{bmatrix},$$

$$\mathbf{B} = \begin{bmatrix} 0 \\ 0 \\ b_3 \end{bmatrix}$$

$$\mathbf{C} = \begin{bmatrix} K_H & 0 & 0 \end{bmatrix}$$

$$a_{21} = \frac{\left(-Mg + T \times L_{p}\right) \times \sin x_{1}}{J_{p}},$$

$$a_{22} = \frac{dT}{dx_2} \times \frac{\cos x_1}{J_p} \times L_p + \frac{f_s}{J_p} \times \frac{dT}{dx_2} - b_{1.p},$$

$$a_{23} = \frac{dT}{dx_3} \times \frac{\cos x_1}{J_p} \times L_p + \frac{f_s}{J_p} \times \frac{dT}{dx_3},$$

$$a_{32} = \frac{-\frac{d\tau_{rotor}}{dx_2}}{J_{\perp}},$$

$$a_{33} = \frac{1}{J_r} \left[ -\left(\frac{r_L}{r_m}\right)^2 \frac{K_\tau K_\nu}{R_a} - \frac{d\tau_{rotor}}{dx_3} - b_1 \right],$$

$$b_3 = \left(\frac{r_L}{r_m}\right) \frac{K_{\tau}}{J_r R_a}.$$

#### A.2 Experimental Data

All experiments were designed and performed in Control Laboratory at Michigan State University. Some experiments apply high-tech equipments such as Force Gauge and Signal Analyzer. Standard experimental procedure and detailed technique are recorded in associated menus available in the laboratory. All measurements precision are recorded in maximum precision of the equipments.

#### A.2.1 Experimental Measurements of the DC Motor Armature Resistance

The armature resistance  $R_a$  is not possible to be measured when the rotor is running. We used the multimeter to measure the static motor armature resistance with respect to twenty-three different angular position of the rotor.

Resistance (ohm)
2.33
2.33 2.36
2.24
2.28
2.20 2.17
2.17
2.27
2.26
2.20
2.15
2.14
2.19 2.10
2.10
2.17
2.20
2.24
2.30
2.38
2.39
2.36
2.09
2.14
2.12

Figure A.2.1 Measurements of the motor armature resistance,  $R_a$ 

#### A.2.2 Relationship between the Thrust and Speed of Rotor

Taking off the counterweight, Force Gauge, which was used to measure lift force, was placed below the rotor assembly to support parallelogram linkage. By using Strobescope Type 4913, we can measure the rotor speed in unit of RPM. The reasonable operating range for rotor speed is from 0 RPM to 1400 RPM. The following measurements were calibrated based on the precision of digital multimeter.

Rotor Speed	Thrust
(RPM)	(N)
0	0
100	4.48x10 <sup>-2</sup>
200	8.96x10 <sup>-2</sup>
300	8.96x10 <sup>-2</sup>
400	8.96x10 <sup>-2</sup>
500	1.79x10 <sup>-1</sup>
600	2.69x10 <sup>-1</sup>
700	4.48x10 <sup>-1</sup>
800	5.38x10 <sup>-1</sup>
900	8.06x10 <sup>-1</sup>
1000	1.06
1100	1.25
1200	1.52
1300	1.79
1400	2.15

Table A.2.2 Measurements for the relationship between the thrust and rotor speed

### A.2.3 Relationship among the Thrust, Torque, Speed of the Rotor, Current and Voltage

We measured the Current and voltage by repeating the same experimental procedure and taking more samples within the reasonable operating range. The results is shown in Table A.2.3.

Speed (RPM)	Voltage (Volts)	Current (Amp)	Thrust (N)
40	1.00	0.150	2.22x10 <sup>-2</sup>
50	2.00	0.200	2.22x10 <sup>-2</sup>
405	3.00	0.290	8.96x10 <sup>-2</sup>
491	3.50	0.360	1.86x10 <sup>-1</sup>
598	4.00	0.450	2.91x10 <sup>-1</sup>
669	4.50	0.540	3.72x10 <sup>-1</sup>
749	5.00	0.630	5.40x10 <sup>-1</sup>
834	5.50	0.740	6.50x10 <sup>-1</sup>
886	6.00	0.890	7.84x10 <sup>-1</sup>
944	6.50	0.990	8.96x10 <sup>-1</sup>
995	7.00	1.12	1.00
1053	7.50	1.26	1.12
1110	8.00	1.40	1.25
1150	8.50	1.54	1.39
1210	9.00	1.73	1.55
1250	9.50	1.86	1.66
1310	10.0	2.00	1.79
1340	10.5	2.12	1.93
1380	11.0	2.26	1.99
1400	11.5	2.39	2.14
1420	12.0	2.53	2.20

Table A.2.3 Measurements for the relationship among the thrust, torque, rotor, current and voltage

# A.2.4 Relationship between output voltage of Hall Effect sensor and the angular displacement of the parallel linkages

Using the split supply  $\pm 6$  volts and adjusting the angular position of the Hall Effect sensor relative to the base support, we can set the nominal output voltage of Hall Effect sensor to nearly zero when the parallelogram linkage is at horizontal position. The following measurements were made with angular displacement of the parallelogram linkage from -32.5° to 40°.

Angular displacement (degree)	Output voltage (Volts)
40.0	-0.753
35.0	-0.677
30.0	-0.612
25.0	-0.542
20.0	-0.47
15.0	-0.365
10.0	-0.276
5.00	-0.167
0.00	-0.047
-5.00	0.108
-10.0	0.235
-15.0	0.391
-20.0	0.521
-25.0	0.713
-30.0	0.854
-32.5	0.903

Table A.2.4 Measurements for the relationship between Hall Effect sensor and the angular displacement of the parallelogram linkage

# A.3 Nominal System Parameters

# **Symbols**

a = 5.72 (Cubic)	Characteristic lift curve slope	(dimensionless)
= 5.99 (Linear)		
= 6.05 (Uniform)		
$b_0 = 6.31 \times 10^{-3}$	Coefficient of Coulomb friction	(N m)
$b_1 = 3.85 \times 10^{-4} \text{ (Cubic)}$	Coefficient of viscous friction	(N m sec/rad)
$= 3.29 \times 10^{-4}$ (Linear)		
$= 3.85 \times 10^{-4} \text{ (Uniform)}$		
$b_{1,p} = 0.33 9$	Coefficient of viscous friction for the	(N sec/rad)
	parallelogram linkage	
$c = 3.00 \times 10^{-2}$	Chord length	(m)
$f_s = 2.30 \text{ x} 10^{-2}$	Offset of acting line of the thrust	(m)
g = 9.81	Magnitude of gravity	$(m/sec^2)$
$J_r = 5.53 \times 10^{-4}$	Moment of inertia for the rotor and	$(kg m^2)$
	the gear assembly	$(kg m^2)$
$K_{\nu} = 6.57 \times 10^{-3}$	Back EMF constant	(Volt sec/rad)
$K_{\tau} = 6.57 \times 10^{-3}$	Torque constant	(N m/amp)
$L_{CG} = 4.95 \times 10^{-1}$	Length from O to C.G. of the parallelogram	(m)
	linkage	
$m = 7.30 \times 10^{-1}$	Mass of the parallelogram linkage and gear	
	assembly	(kg)
$R = 2.20 \times 10^{-1}$	Radius of the rotor	(m)
$R_a = 2.25$	Armature resistance	(ohm)

## **Greek Characters**

$$\theta_p = 13.0^{\circ}$$
 (Cubic) Pitch angle (degree)

= 12.80 (Linear)

= 13.1<sup>o</sup> (Uniform)

 $\rho = 1.23$ 

Air density

 $(kg/m^3)$ 

#### A.4 Parameter Uncertainties

All uncertainties which were derived from conic sector bounds, or hard-bound and used in chapters are listed below.

(1) Armature resistance

$$R_{a,0} = 2.27 \ (ohm)$$

$$R_a \in [2.10, 2.40]$$

(2) Coefficient of Coulomb friction

$$b_{0.0} = 6.31 \times 10^{-3} (N m)$$

$$b_0 \in [5.99, 6.62] \times 10^{-3}$$

- (3) Coefficient of viscous friction in the drive train
- (i) Cubic

$$b_{10} = 3.84 \times 10^{-4} Nm(sec/rad)$$

$$b_0 \in [3.65, 4.04] \times 10^{-4}$$

(ii) Linear

$$b_{10} = 3.29 \times 10^{-4} Nm(sec/rad)$$

$$b_0 \in [3.12, 3.45] \times 10^{-4}$$

(iii) Uniform

$$b_{1.0} = 3.41 \times 10^{-4} N m (sec/rad)$$

$$b_0 \in [3.24, 3.58] \times 10^{-4}$$

(4) Torque constant

$$K_{5,0} = 0.00657 (Nm/Amp)$$

$$K_{\tau} \in [6.24, 6.89] \times 10^{-3}$$

(5) Back EMF constant

$$K_{v,0} = 0.00657 (Volt (sec/rad))$$

$$K_V \in [6.24, 6.89] \times 10^{-3}$$

(6) Hall Effect output equation

$$V_s = K_H \theta$$
,  $K_{H,0} = 0.0235$ 

$$K_H \in [2.00, 2.50] \times 10^{-2}$$

- (7) Lift curve slope (no unit)
  - (i) Cubic

$$a_0 = 5.72$$

$$a \in [5.44, 6.01]$$

(ii) Linear

$$a_0 = 5.99$$

$$a \in [5.69, 6.29]$$

(iii) Uniform

$$a_0 = 6.05$$

$$a \in [5.75, 6.35]$$

## (7) Pitch angle

(i) Cubic

$$\theta_{p,0} = 1.30 \times 10^{1} \text{ (deg } ree)$$
  $\theta_{p} \in [1.23, 1.36] \times 10^{1} \text{ (deg } ree)$ 

(ii) Linear

$$\theta_{p,0} = 1.28 \times 10^{1} \text{ (deg } ree)$$
  $\theta_{p} \in [1.21, 1.34] \times 10^{1} \text{ (deg } ree)$ 

(iii) Uniform

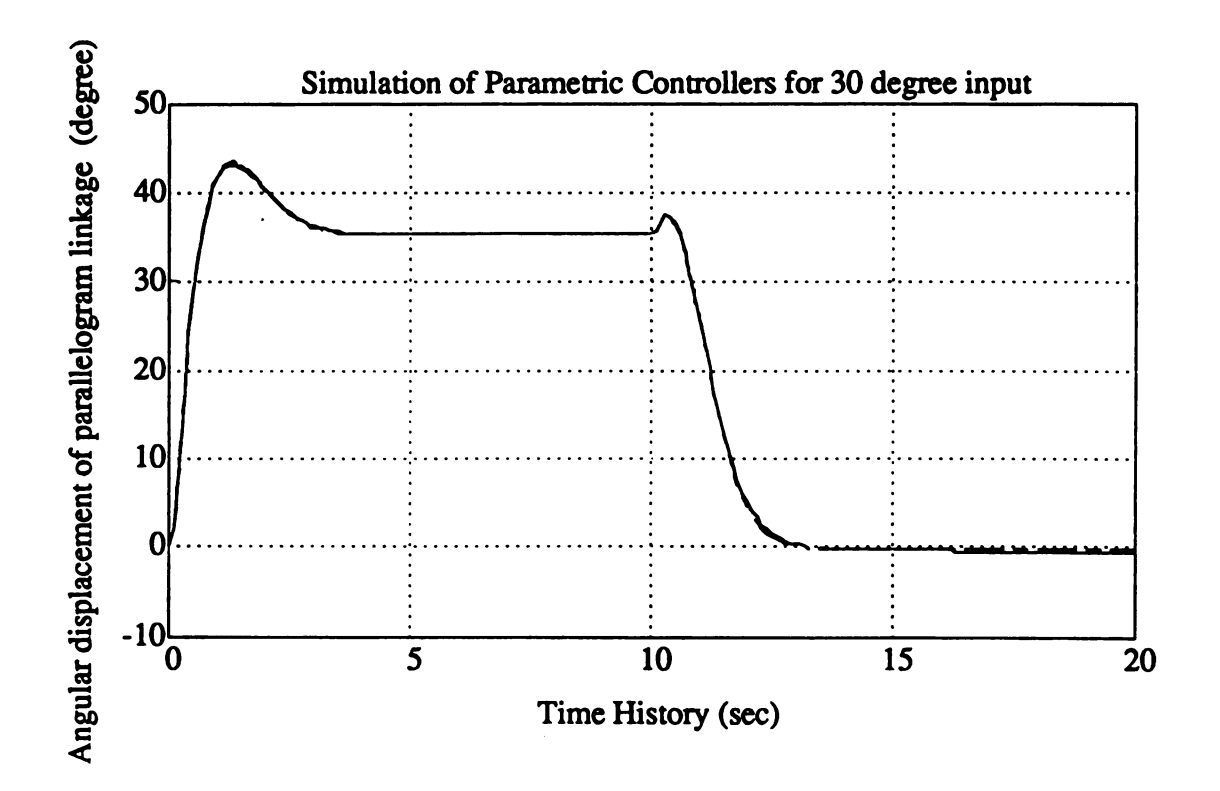
$$\theta_{p,0} = 1.31 \times 10^{1} \text{ (deg } ree)$$
  $\theta_{p} \in [1.24, 1.37] \times 10^{1} \text{ (deg } ree)$ 

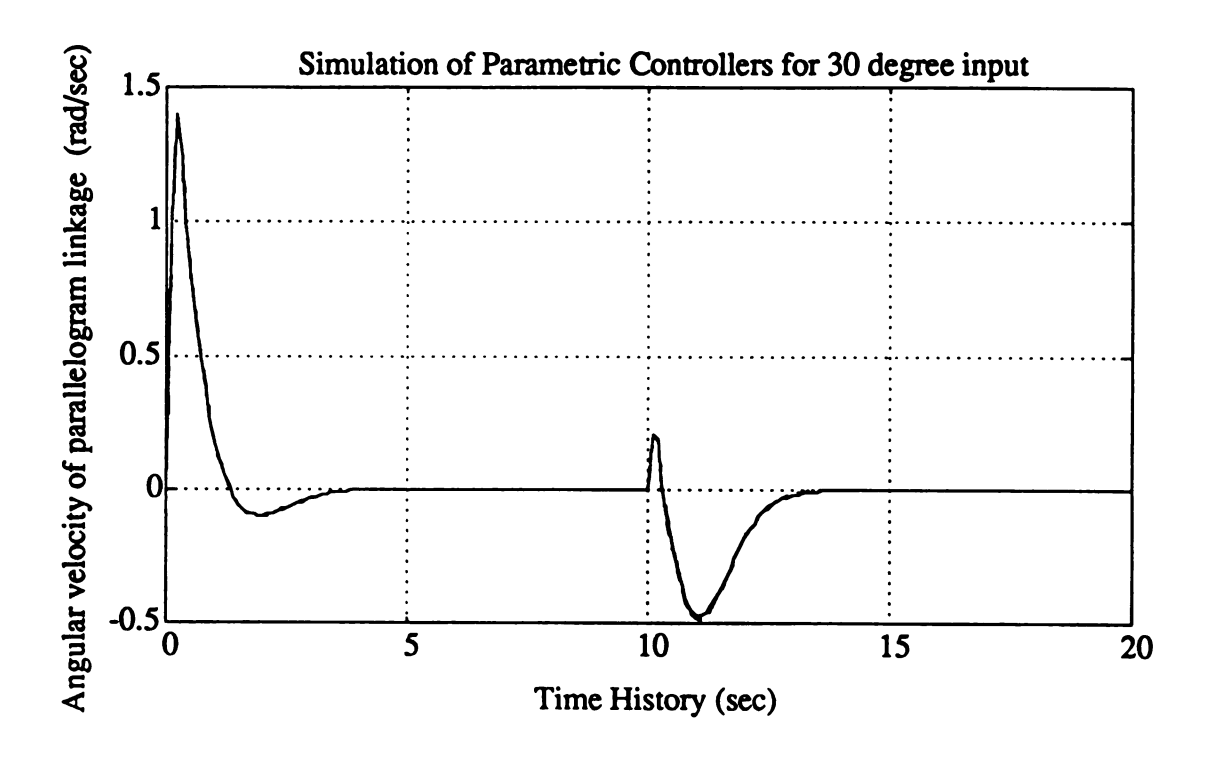
#### A.5 Simulation Results

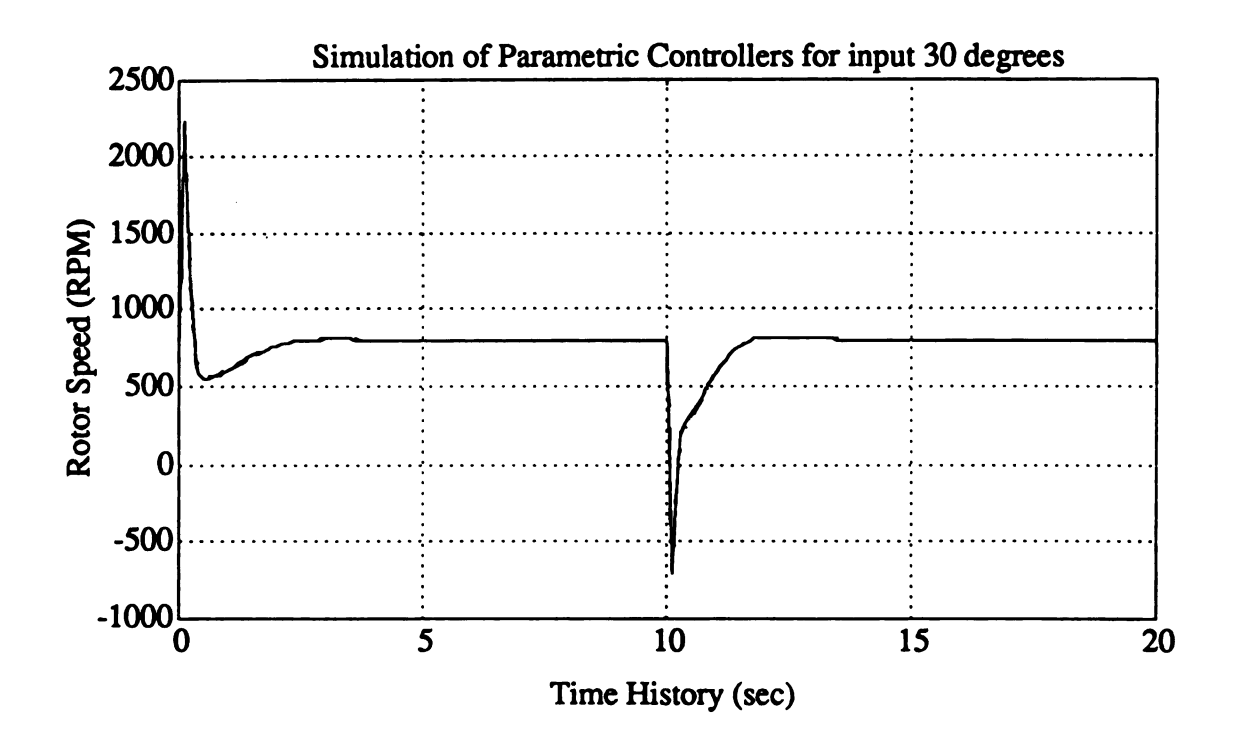
Three state traces and control effort which is corresponding to worst-case response are all plotted in the following eighty-four plots with the input  $10^{\circ}$ ,  $20^{\circ}$  or  $30^{\circ}$  and  $\lambda = 0.1$  or 0.2 In each plot, the corresponding controller is

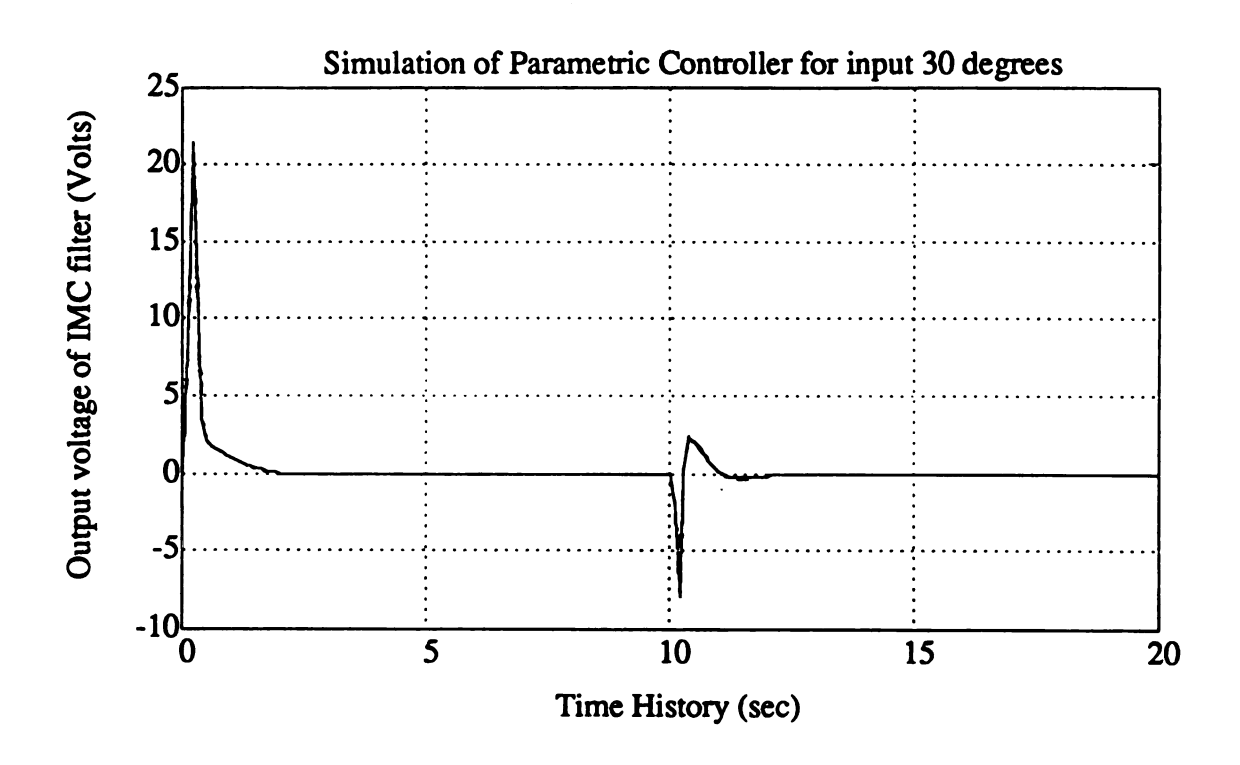
- (1) Solid line Controller a or e
- (2) Dashed line Controller b or f
- (3) Dotted line Controller c or g
- (4) Dot dashed line Controller d or h

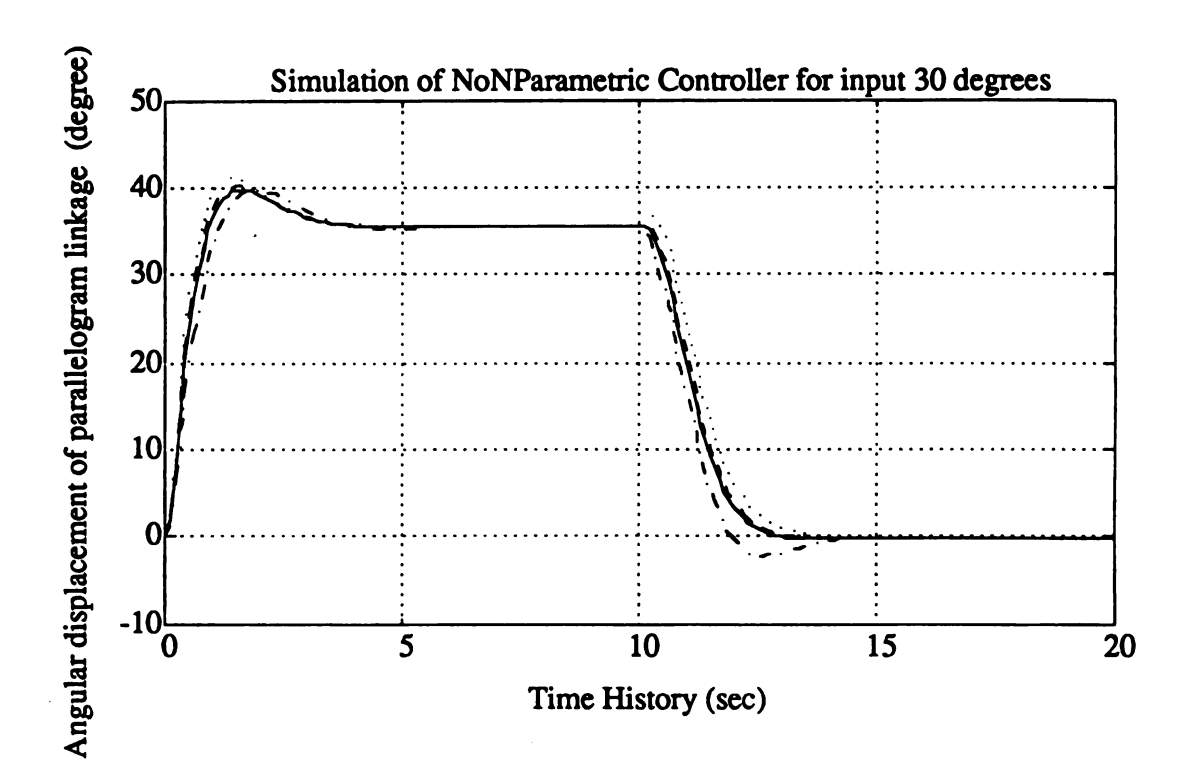
#### (1) The first twenty-four plots are for the IMC controllers with $\lambda = 0.1$

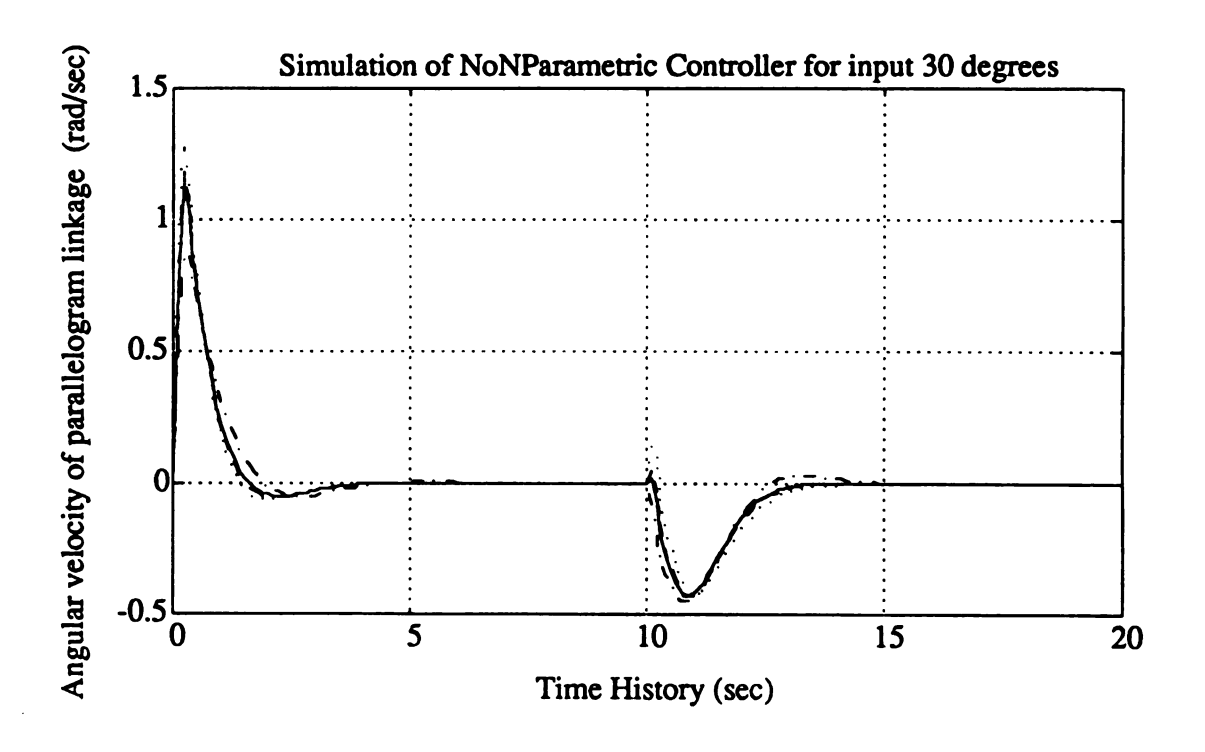


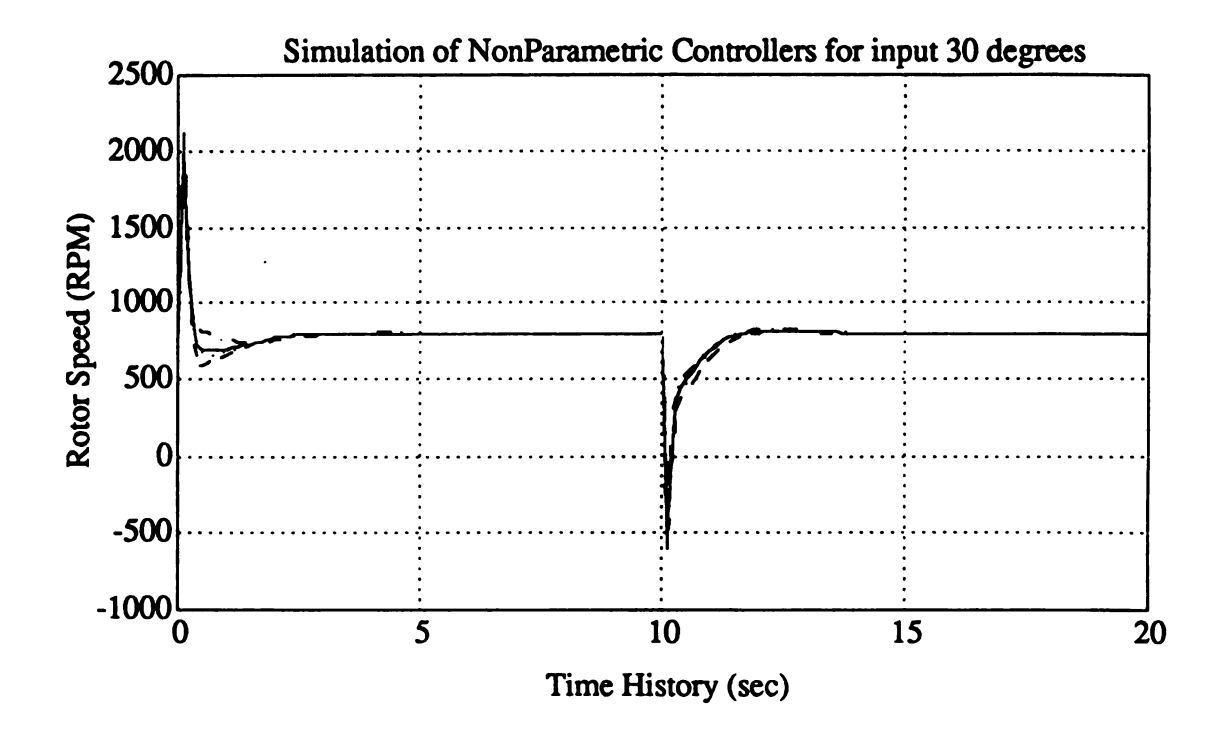


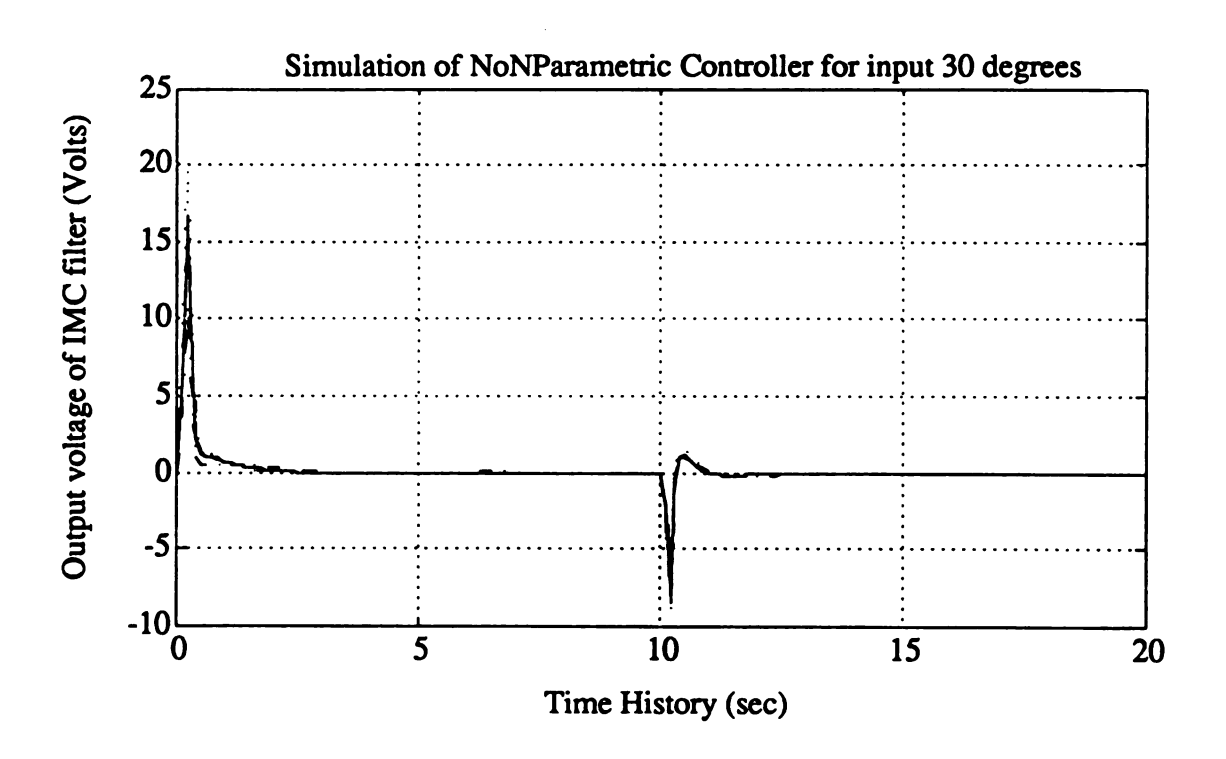


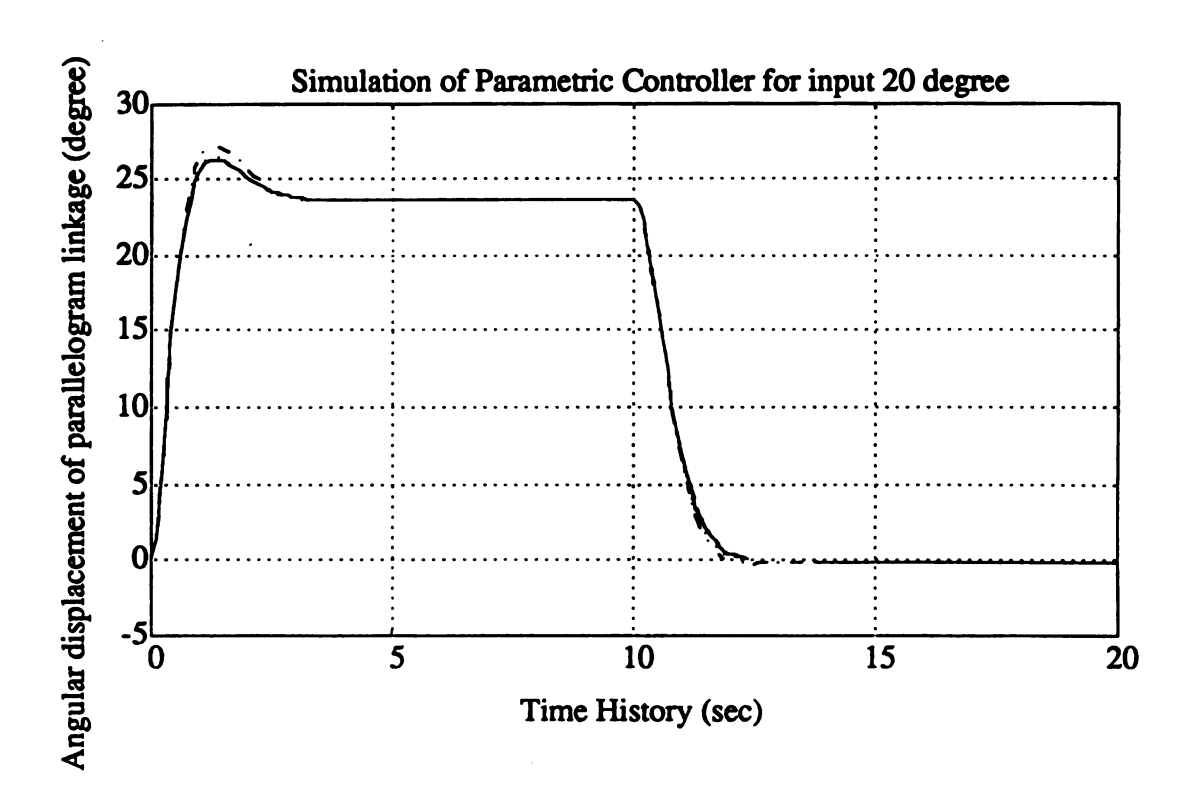


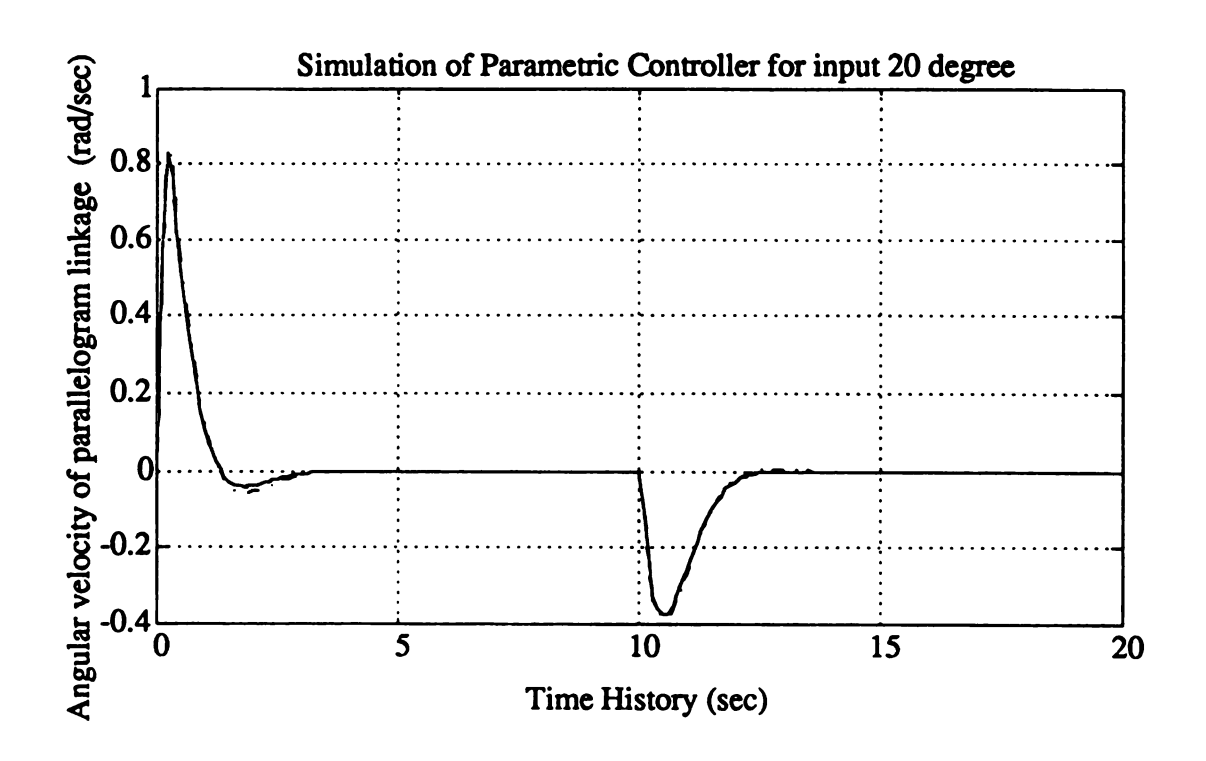


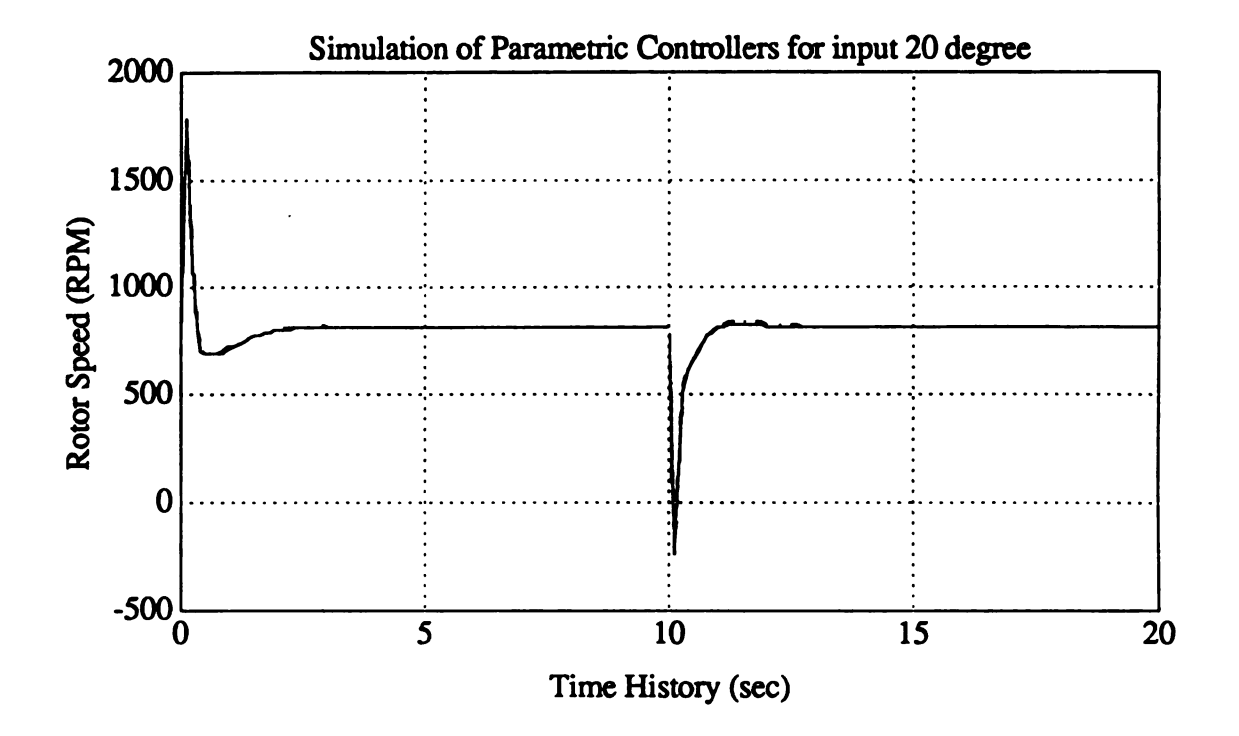


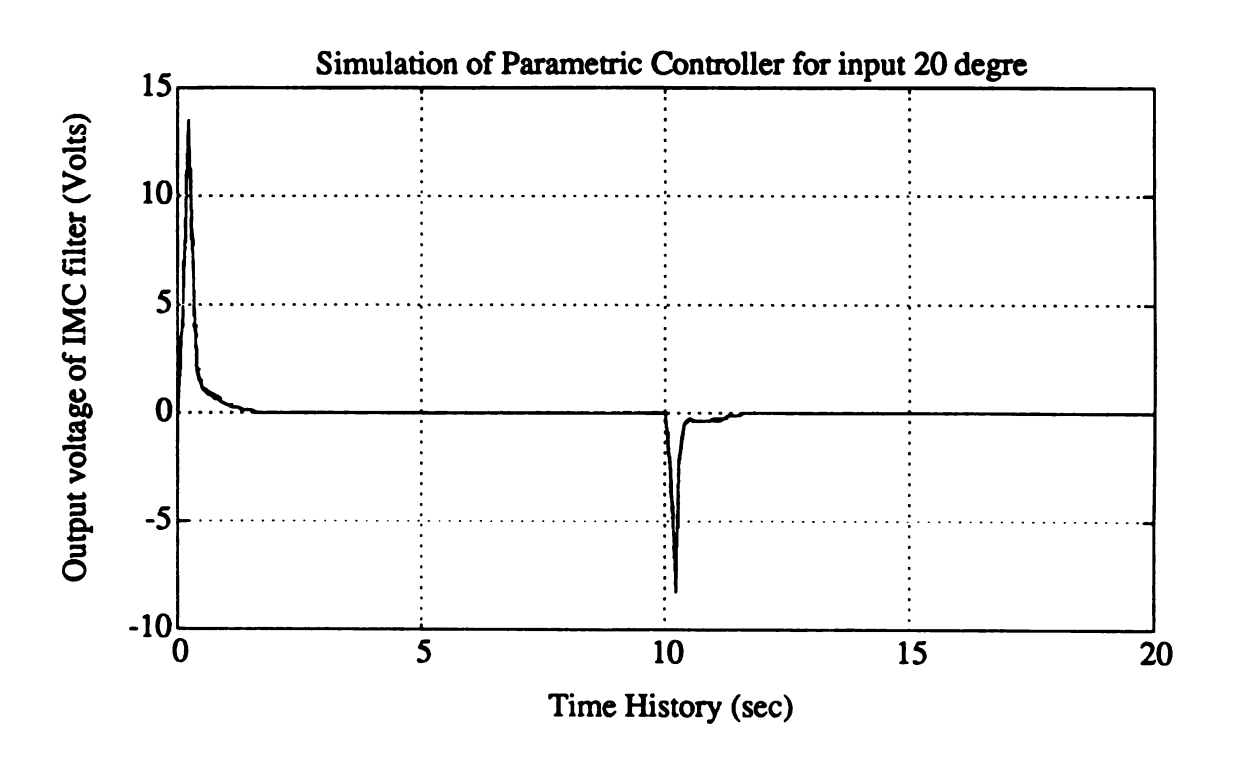


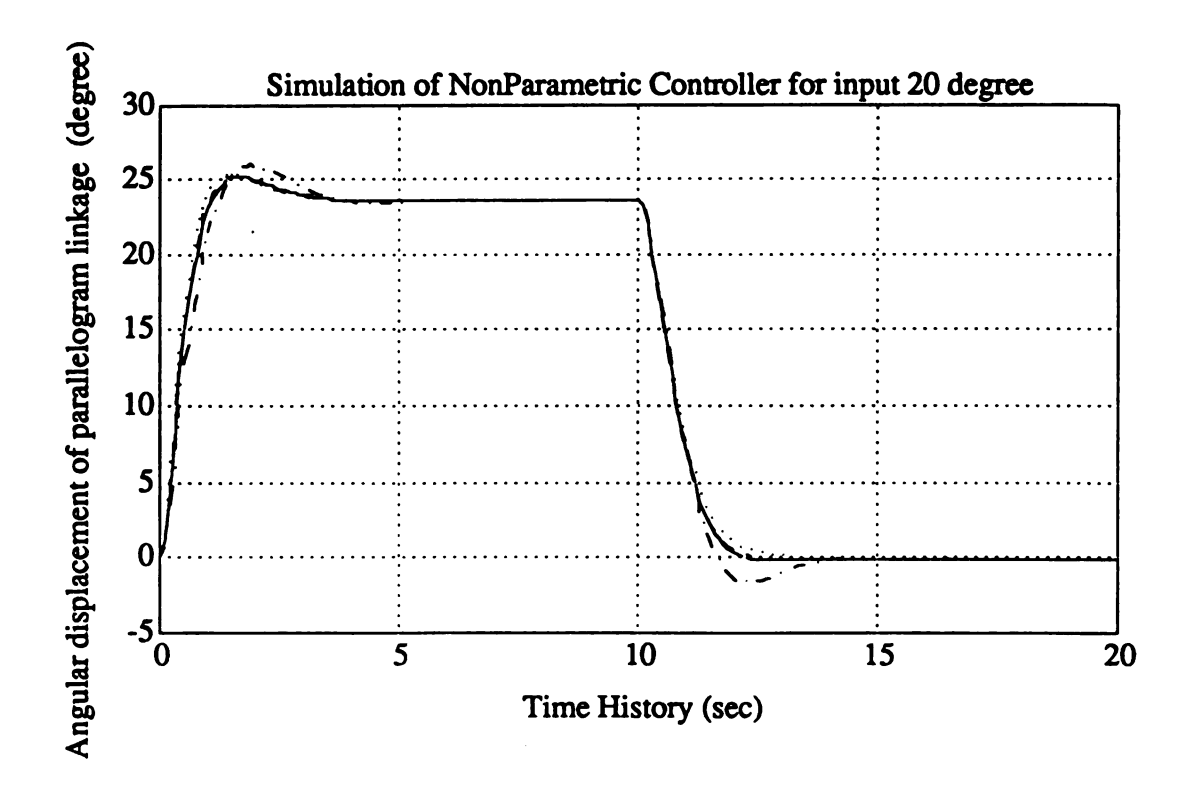


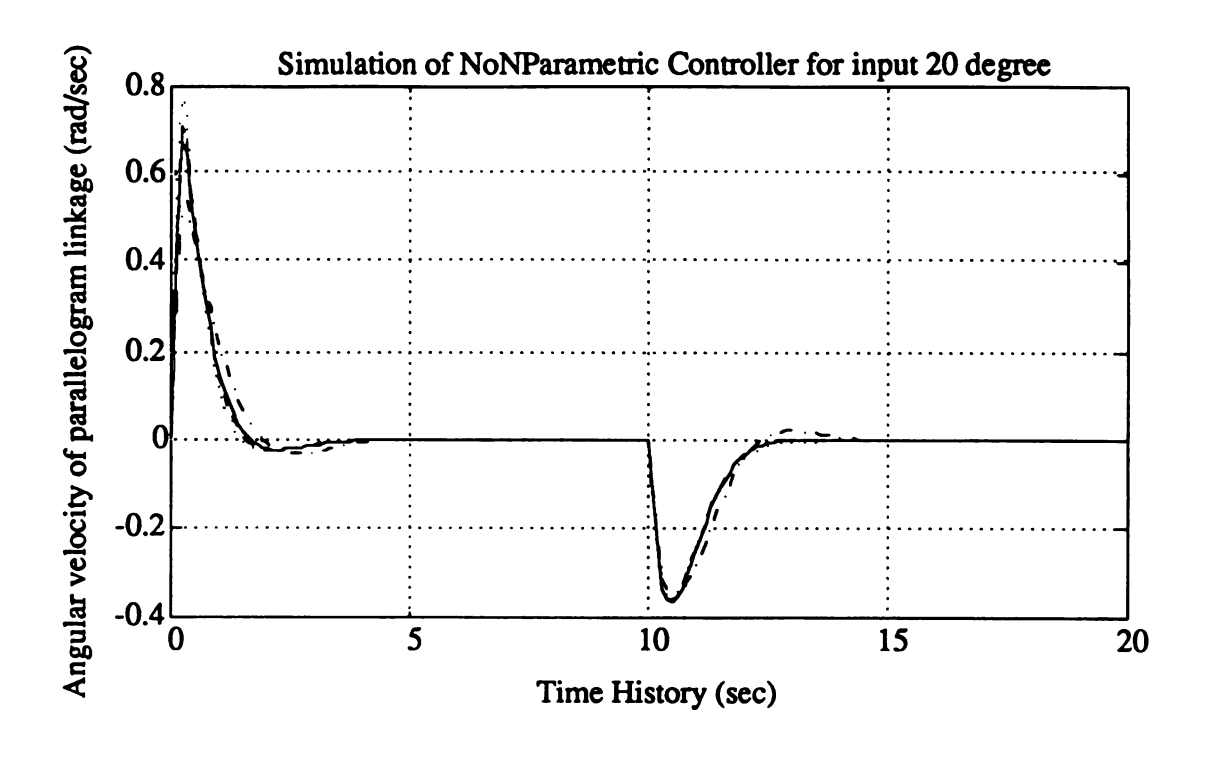


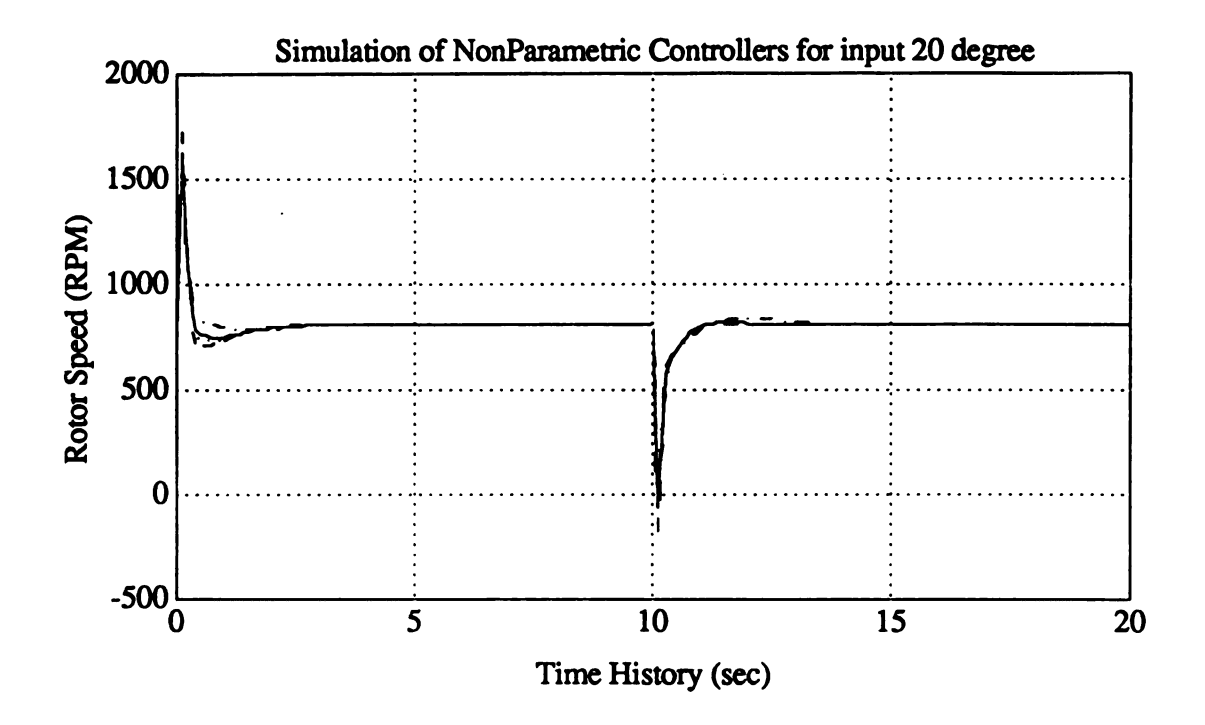


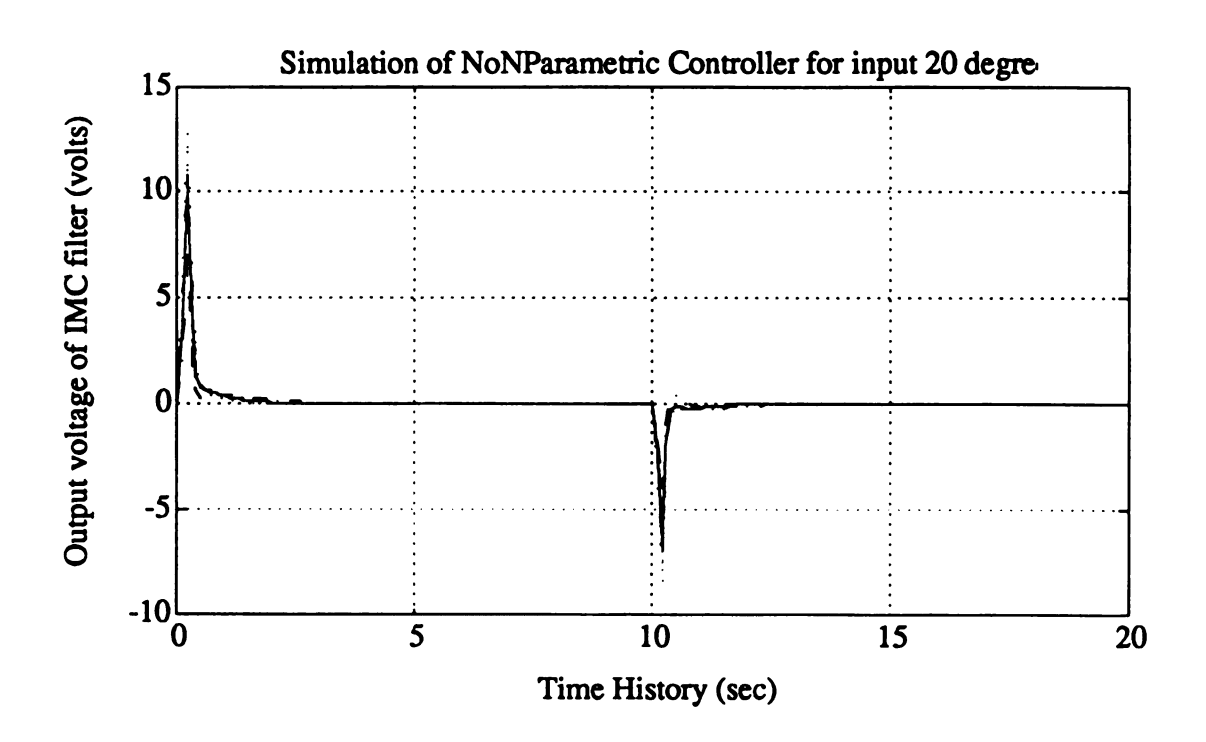


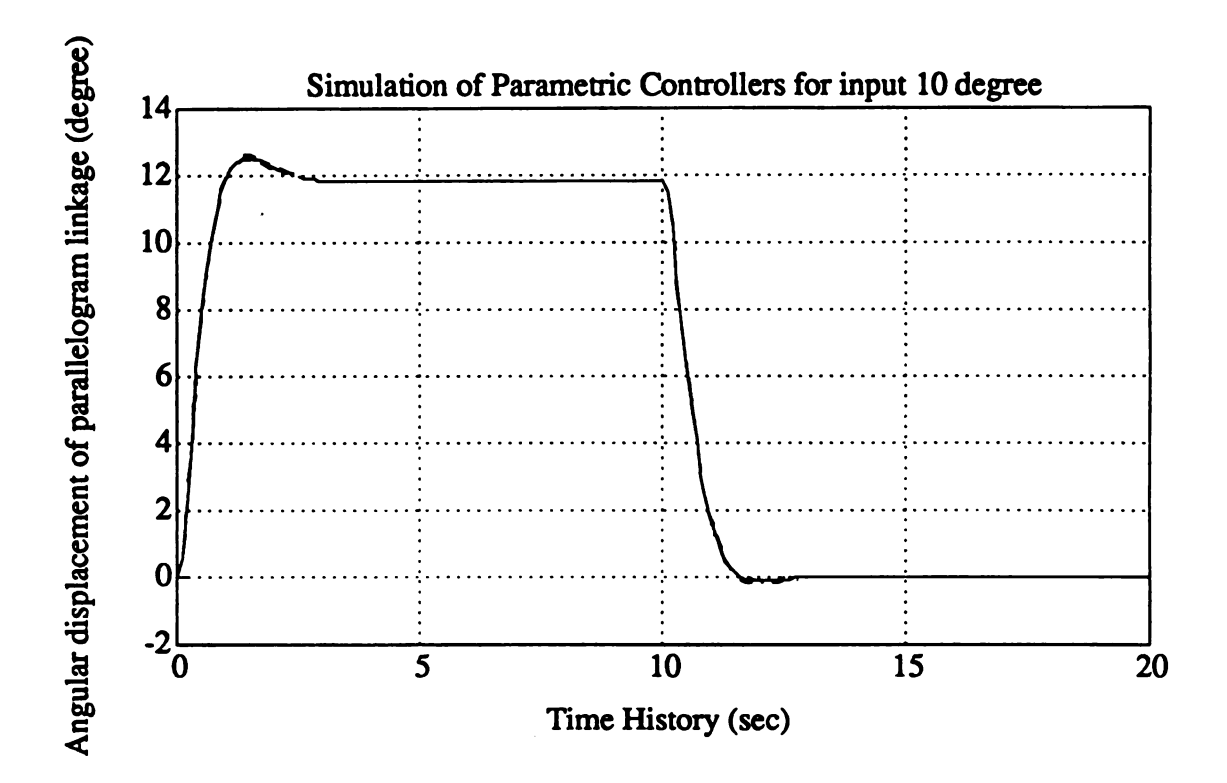


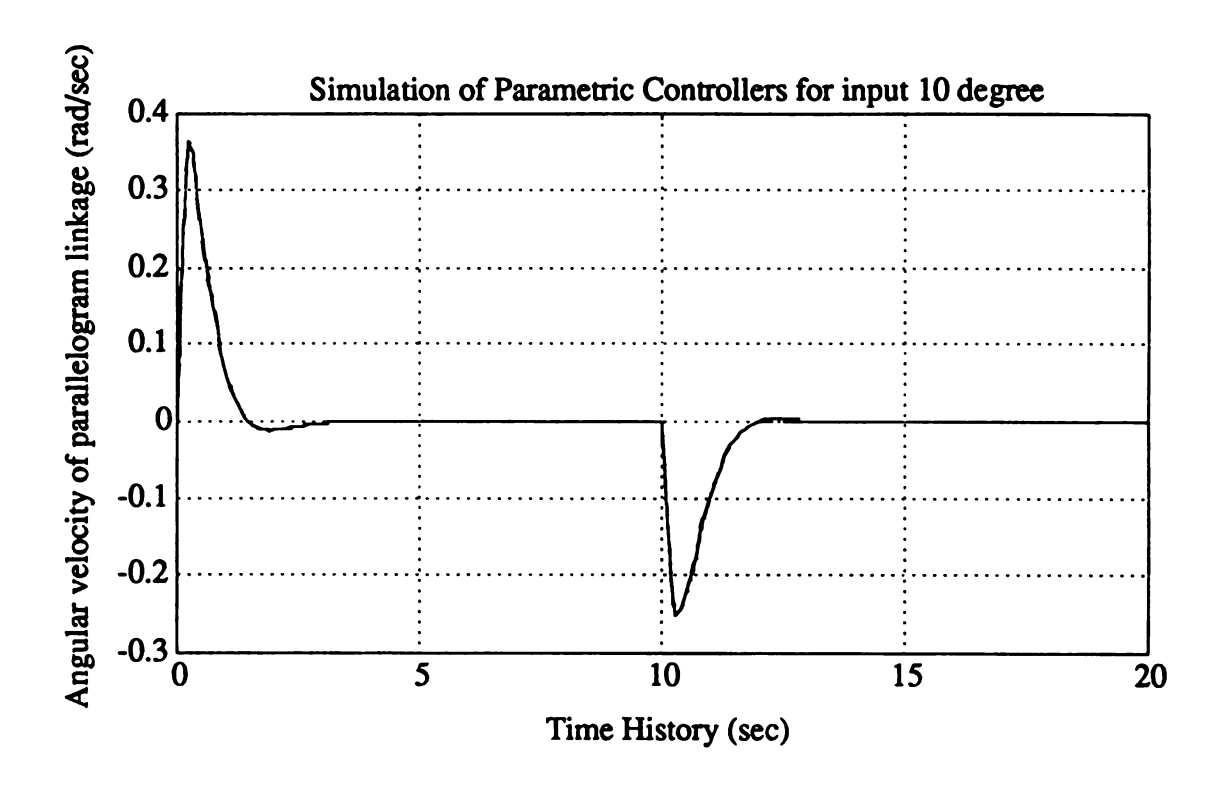


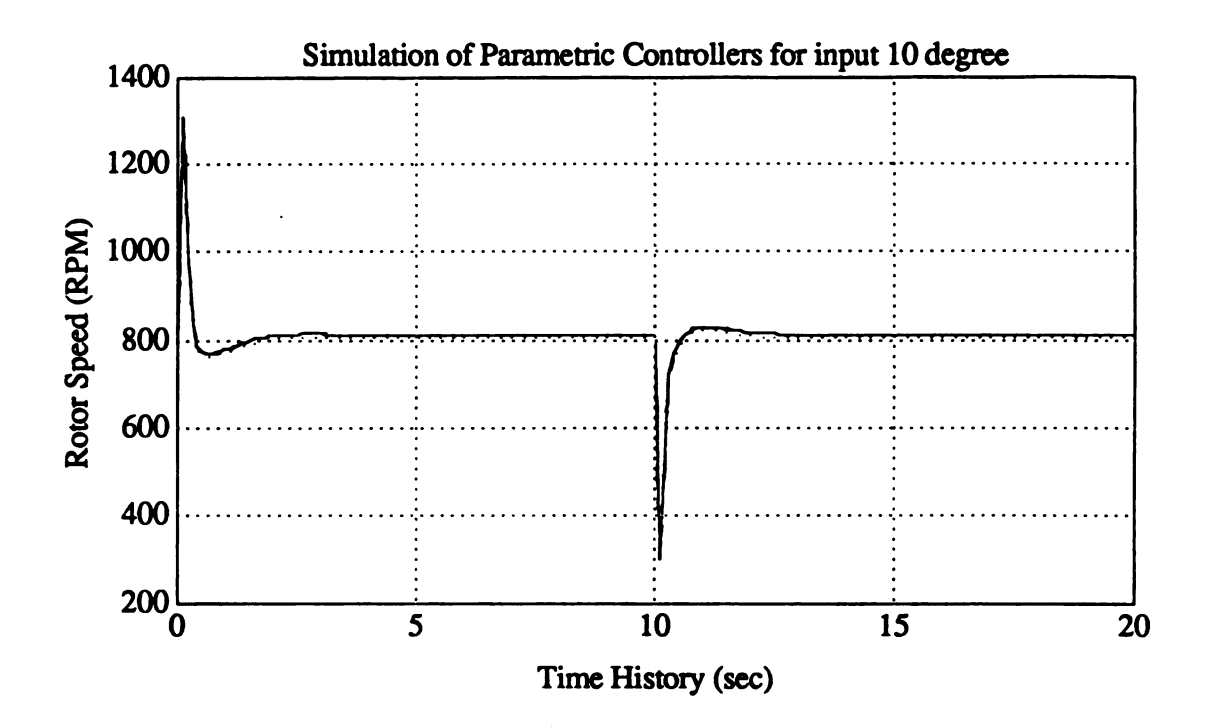


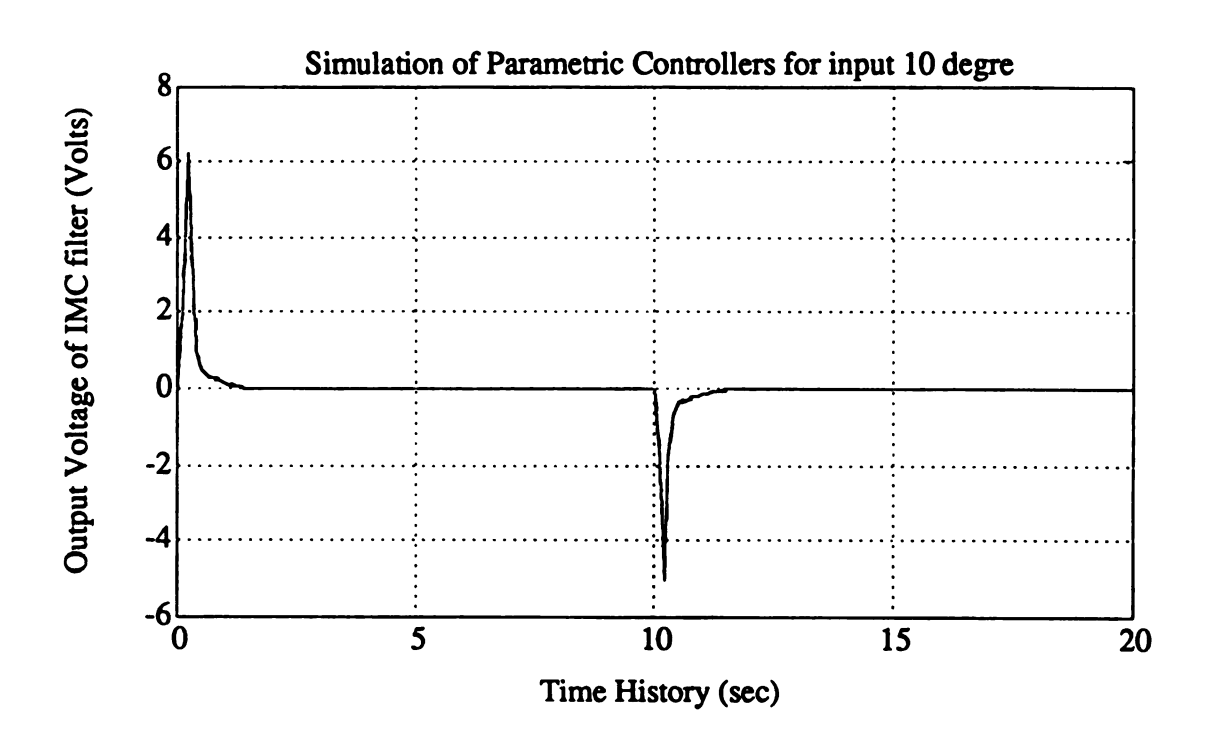


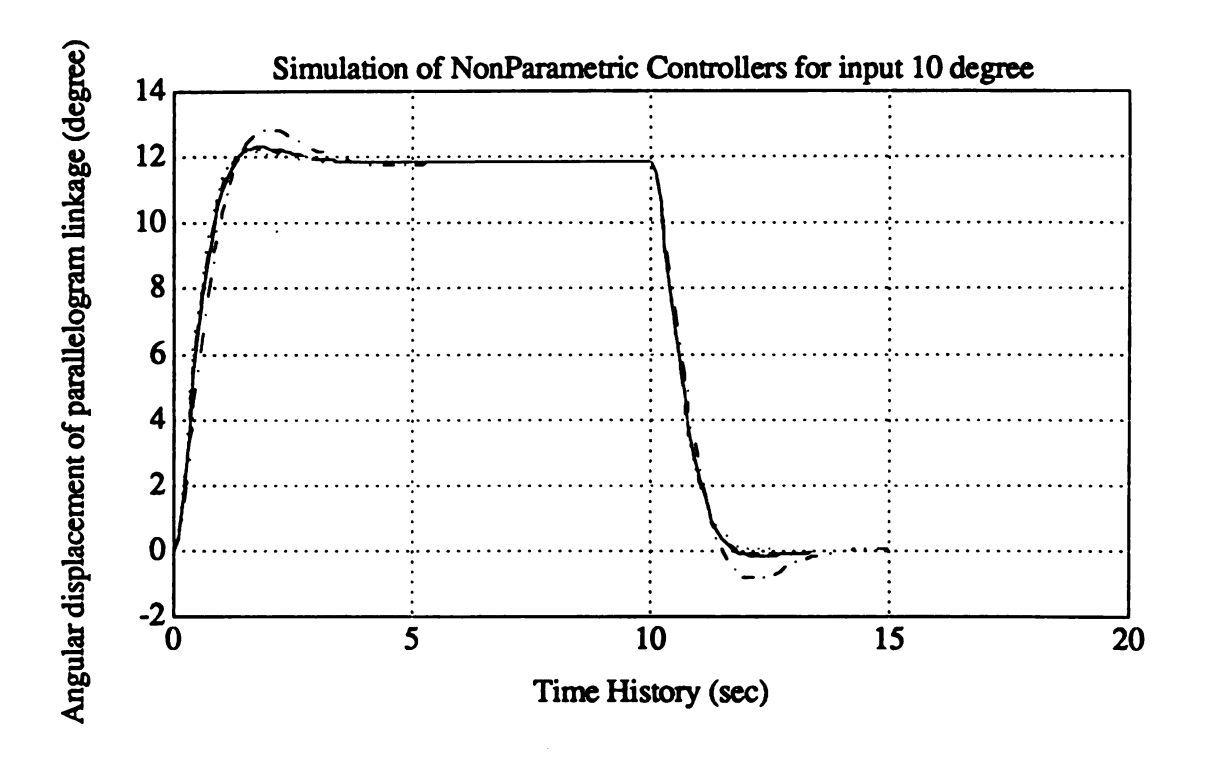


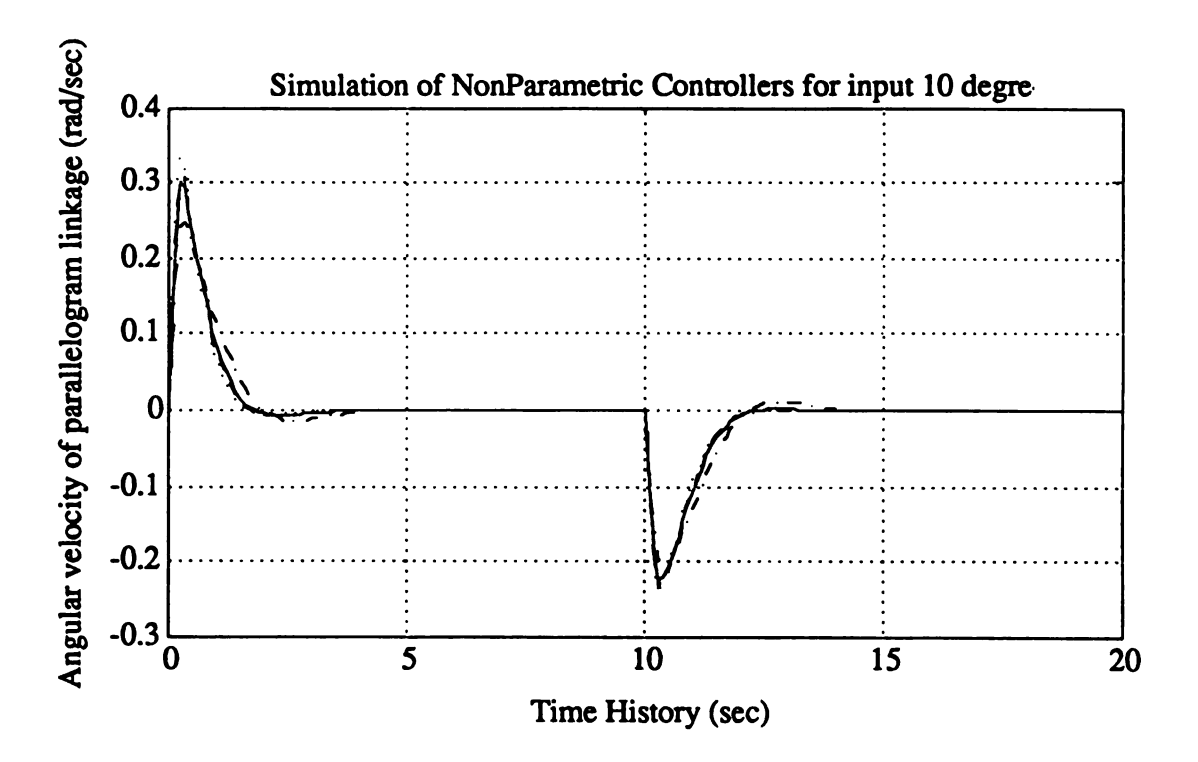


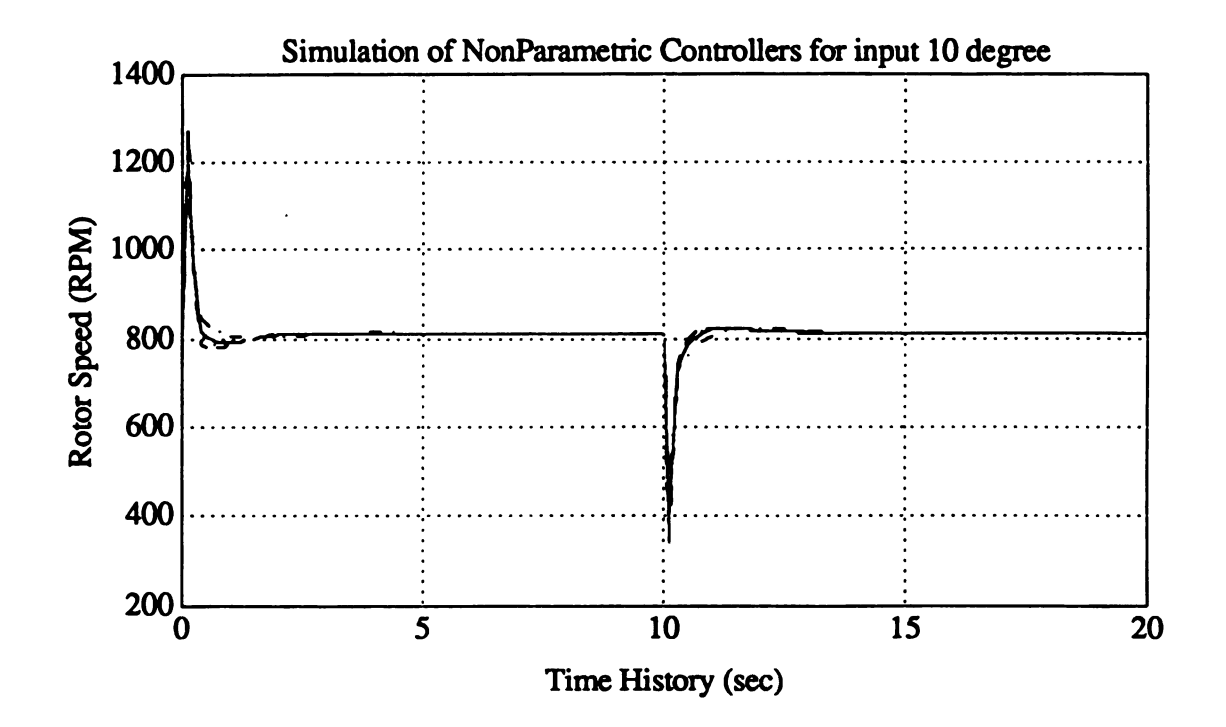


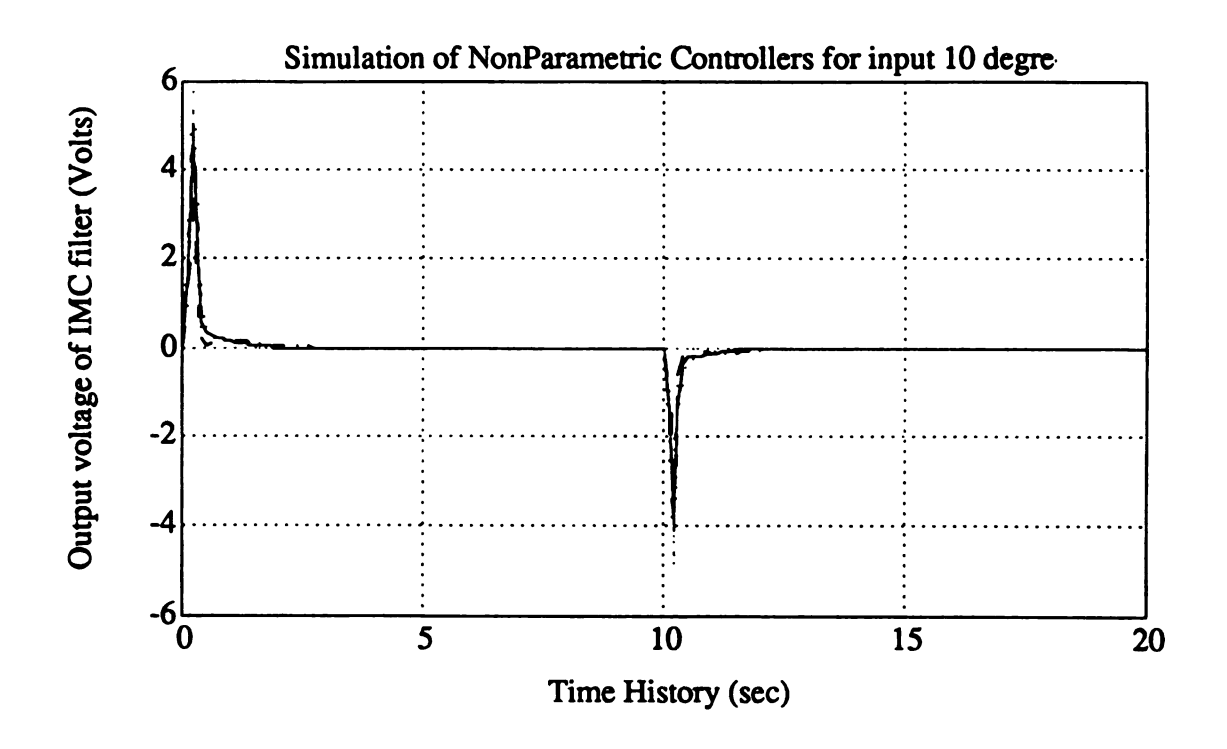




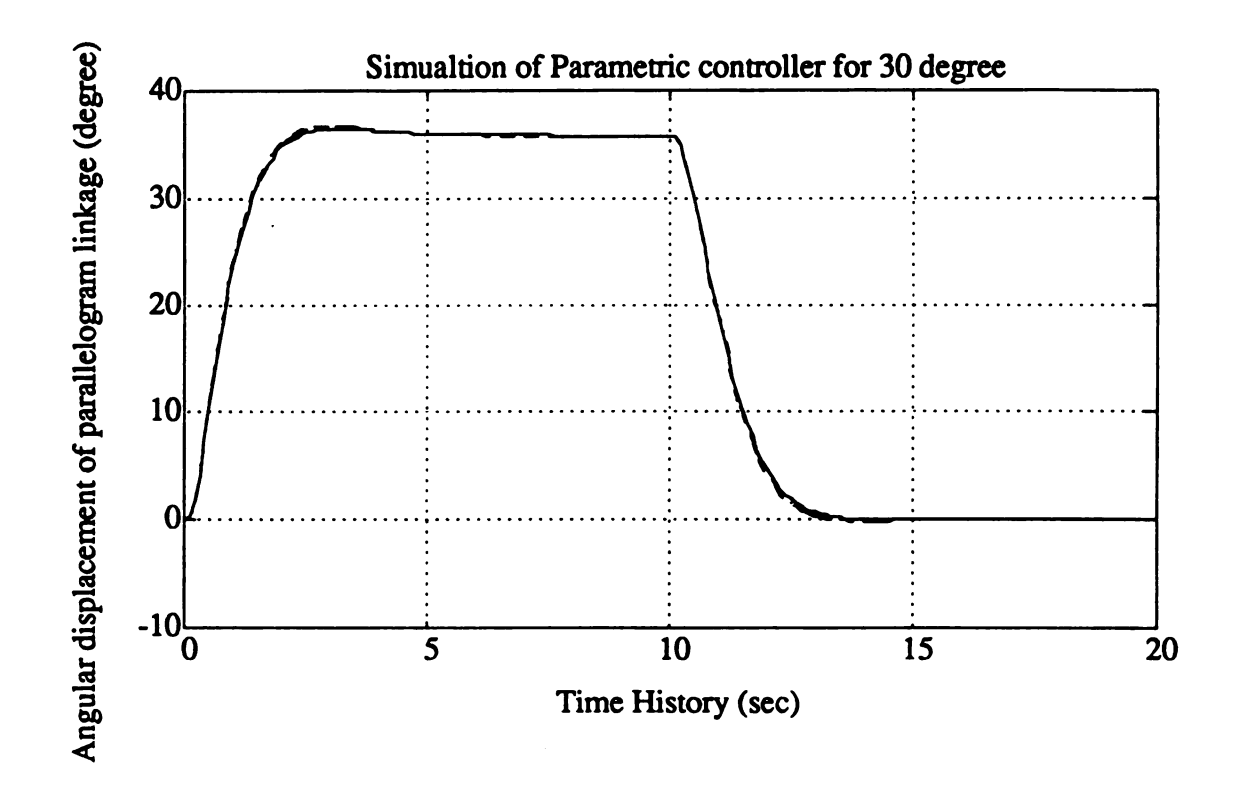


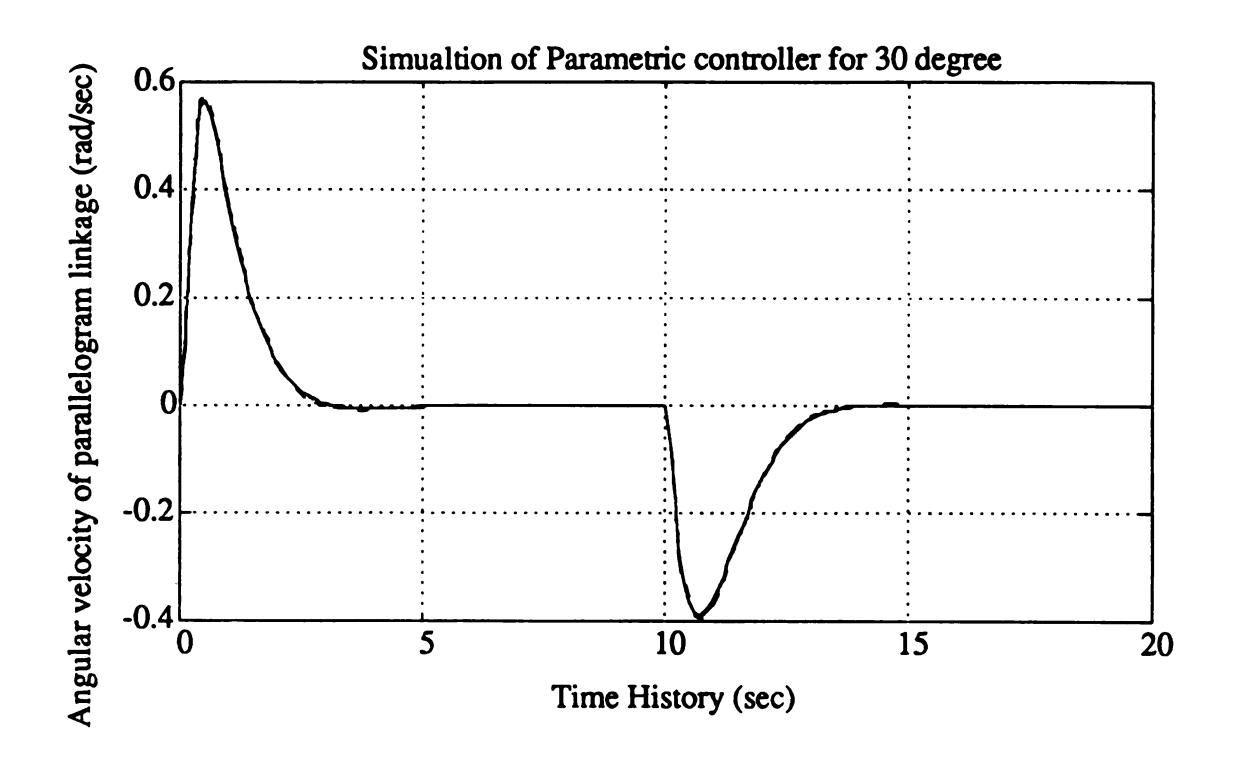


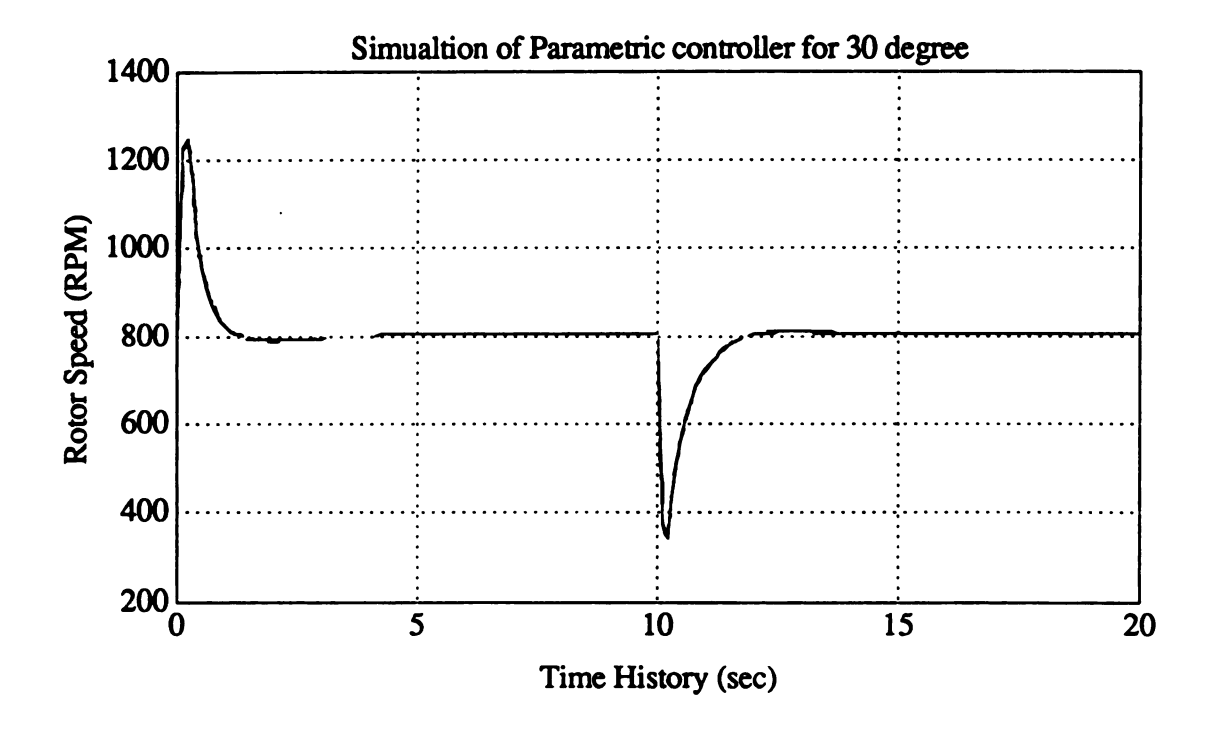


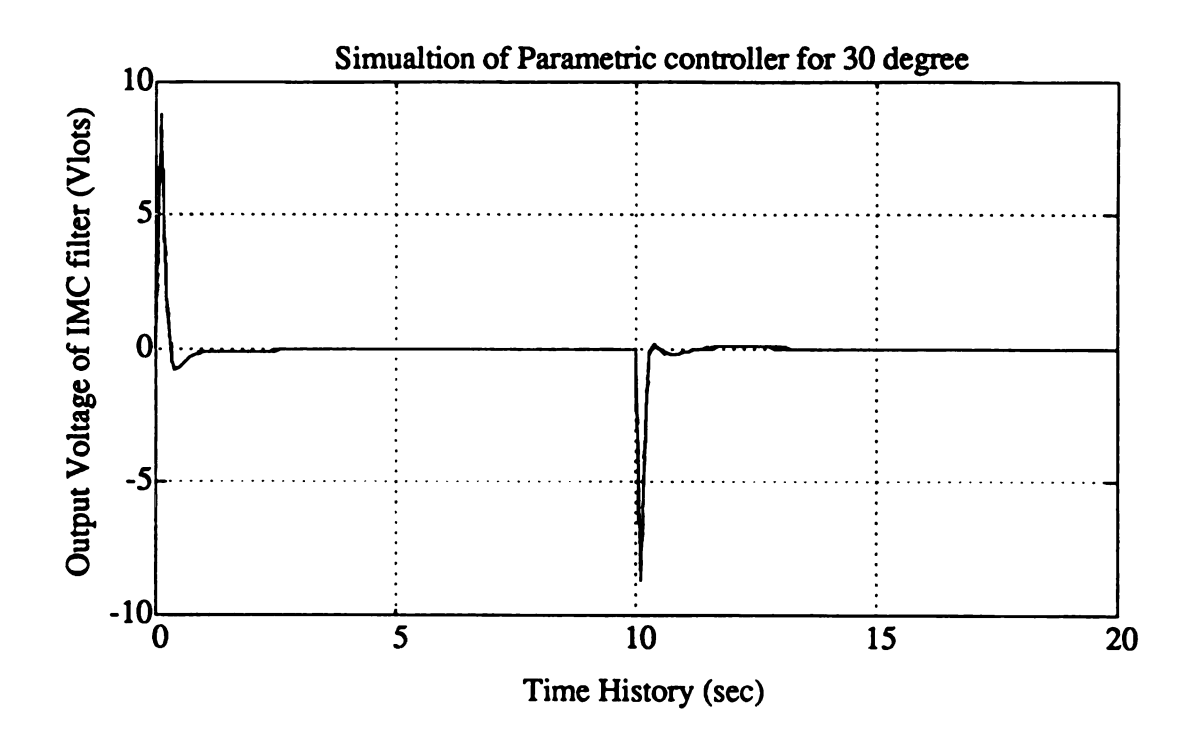


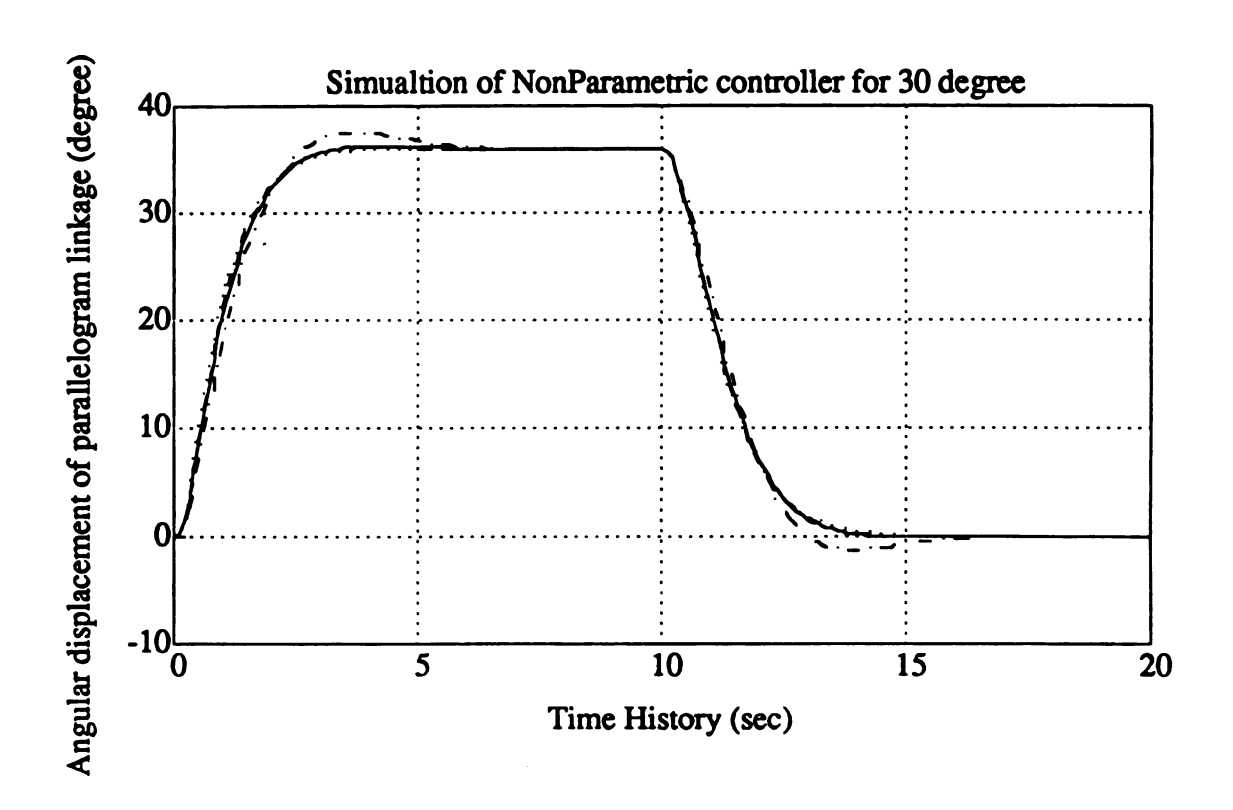
## (2) The next twenty-four plots are for IMC controllers with $\lambda = 0.2$

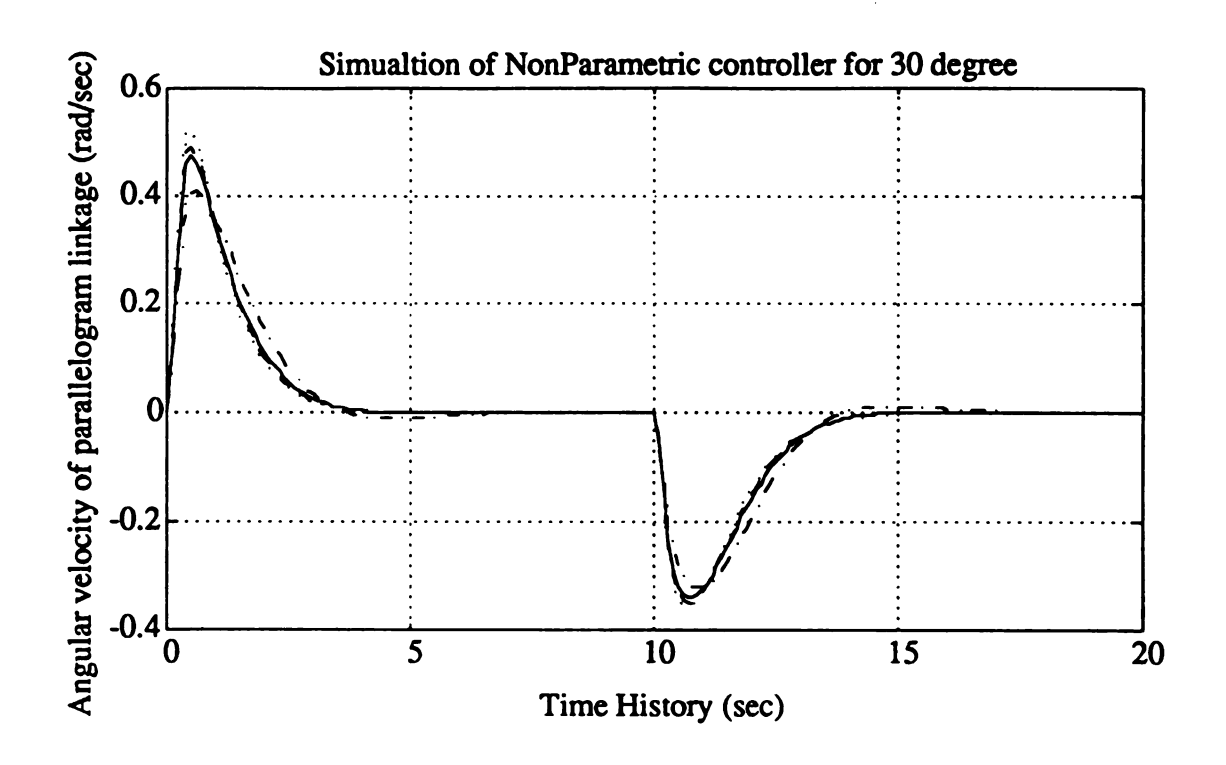


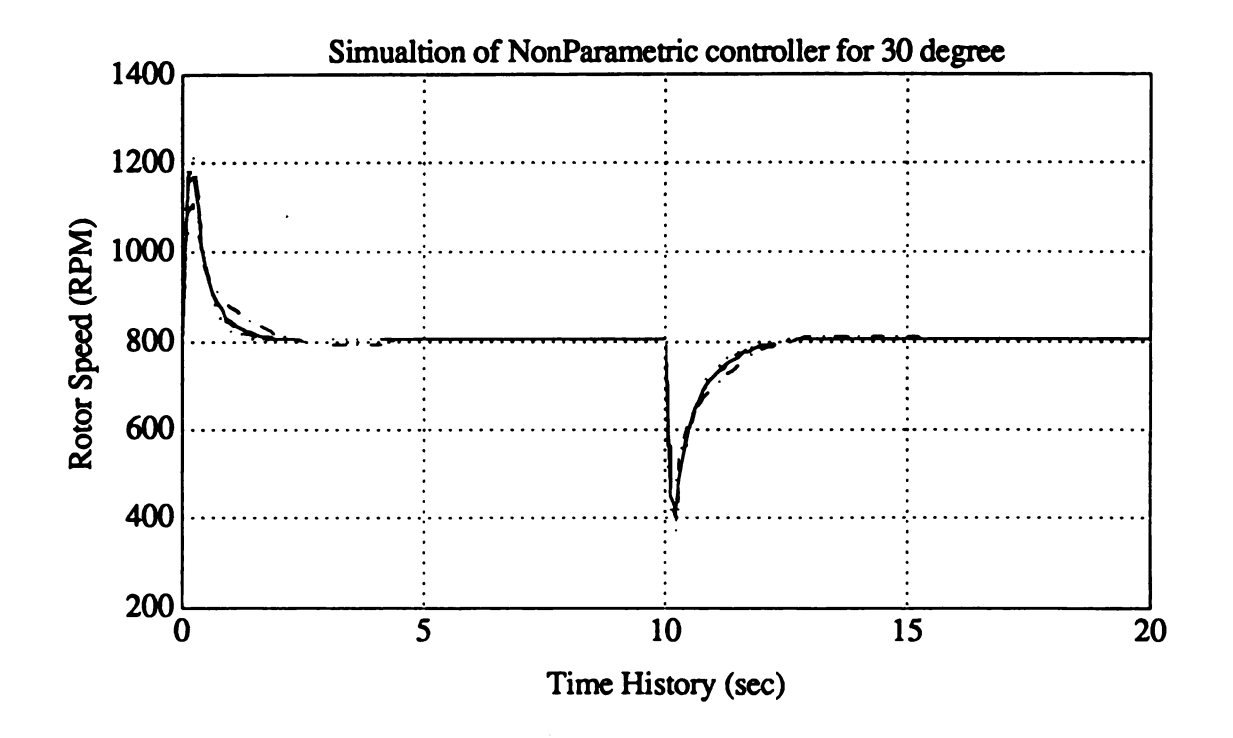


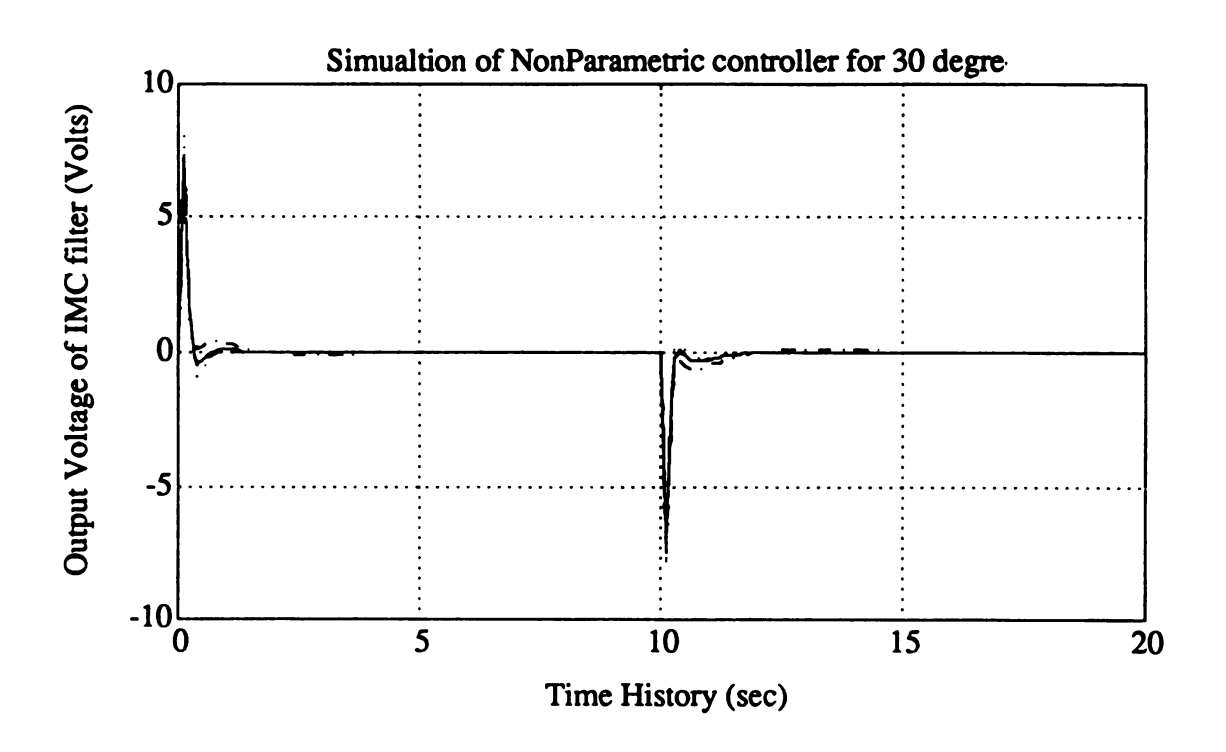


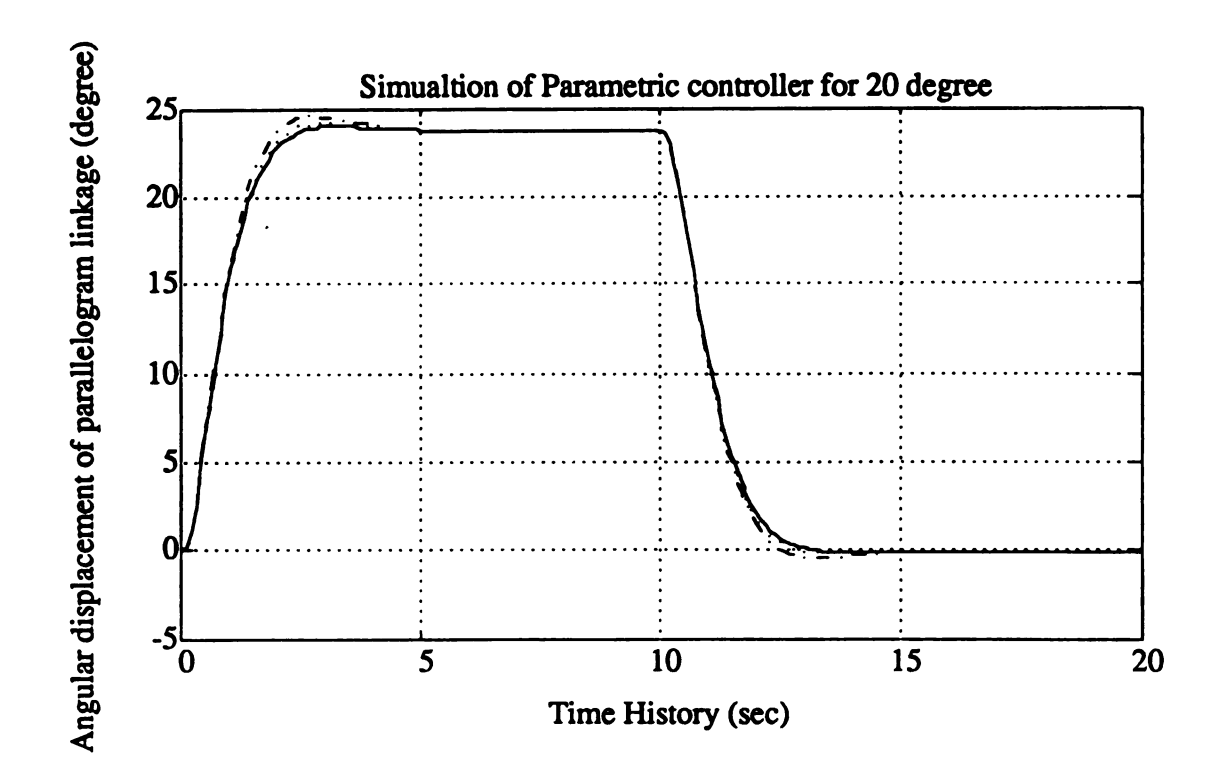


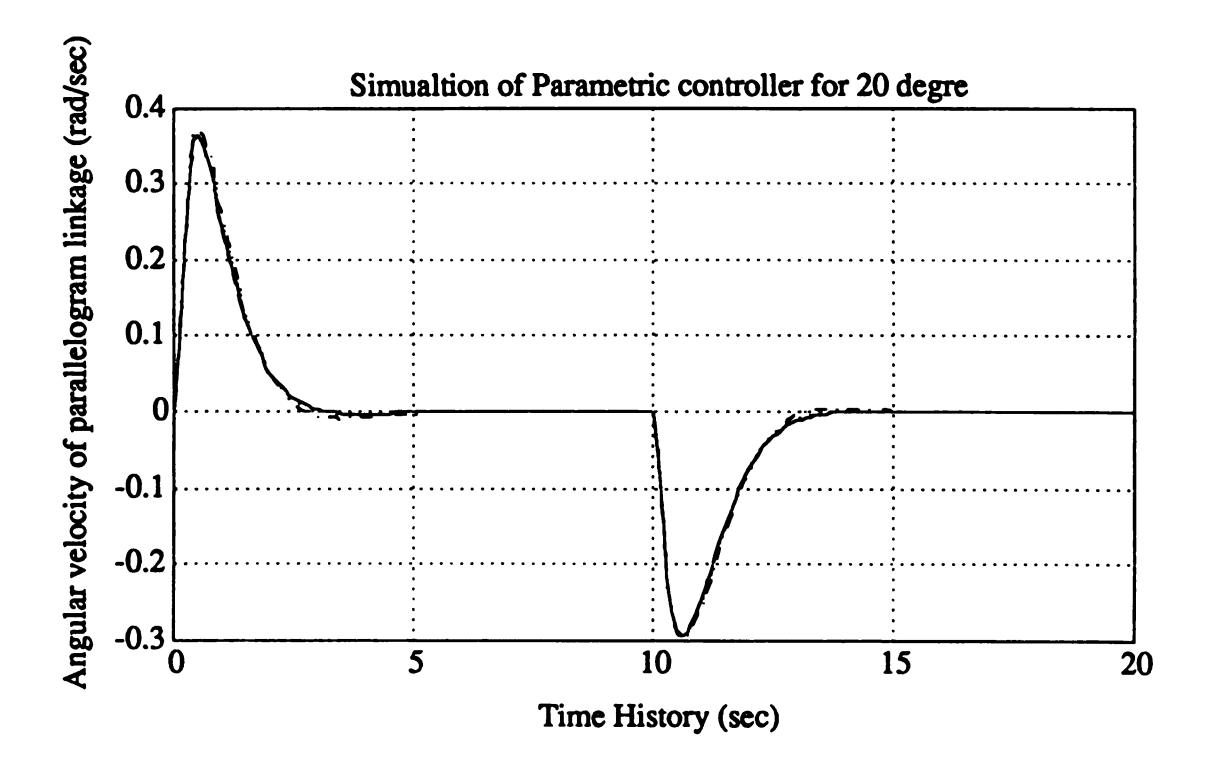


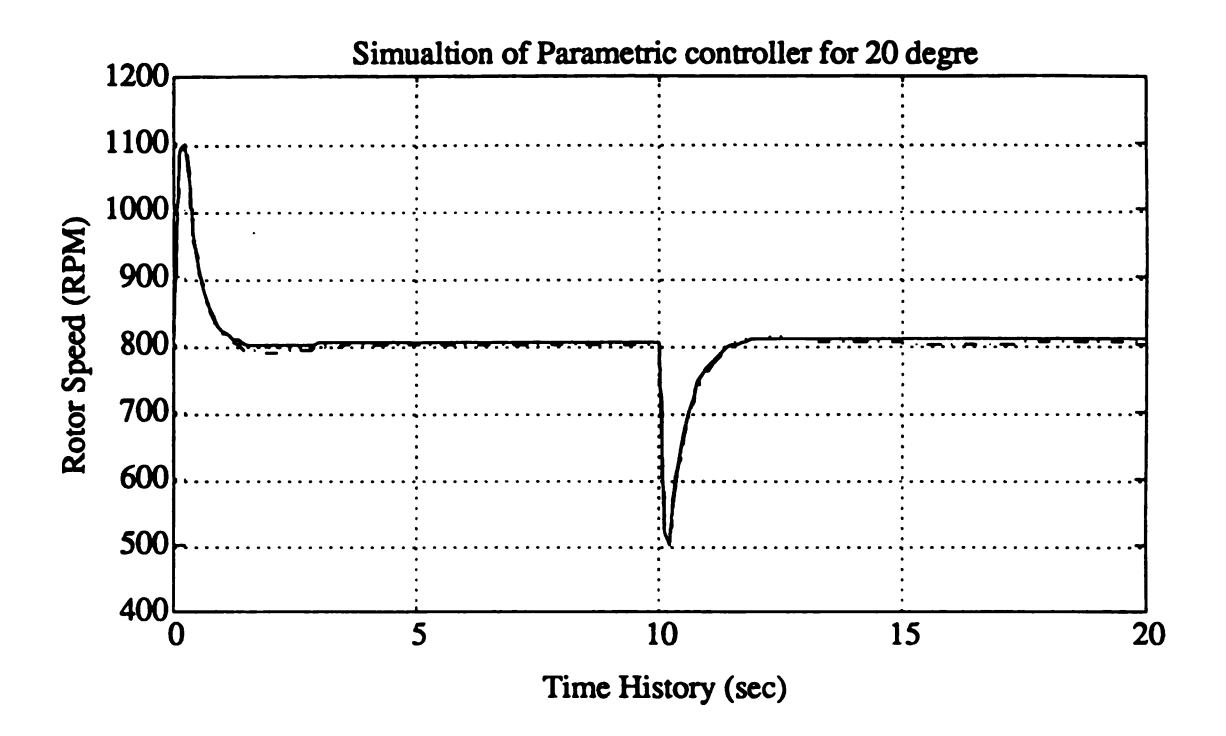


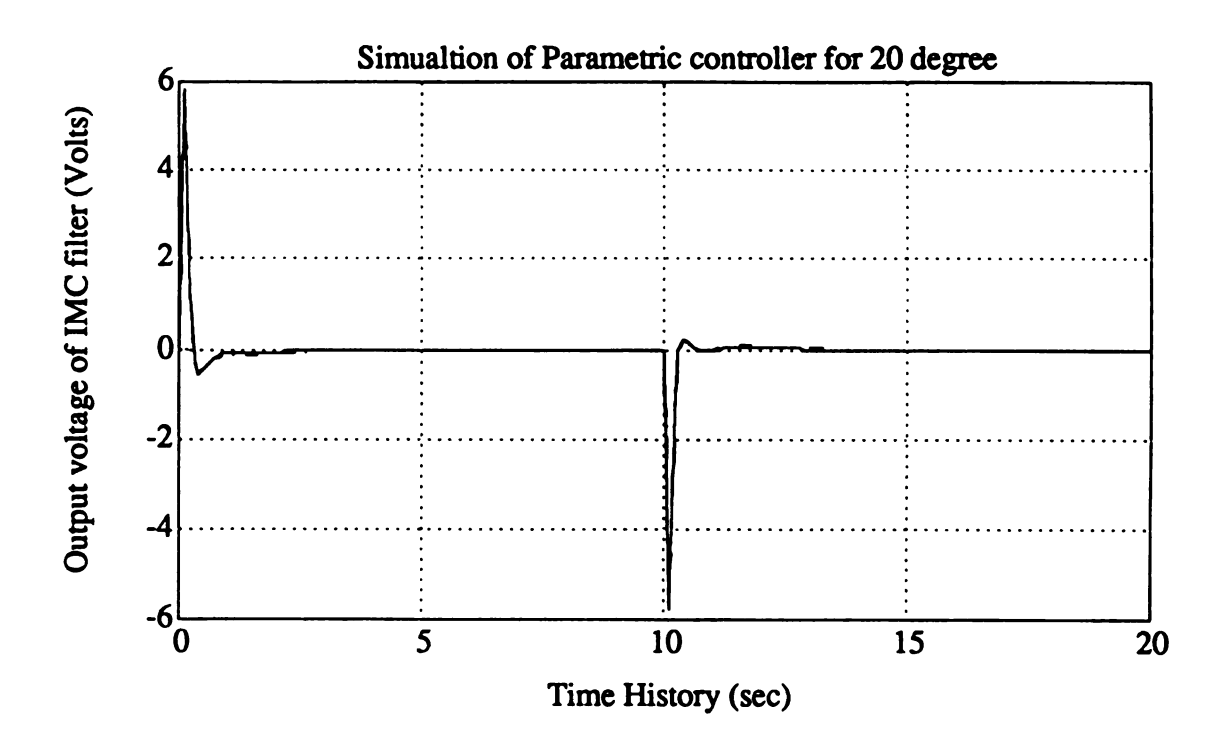


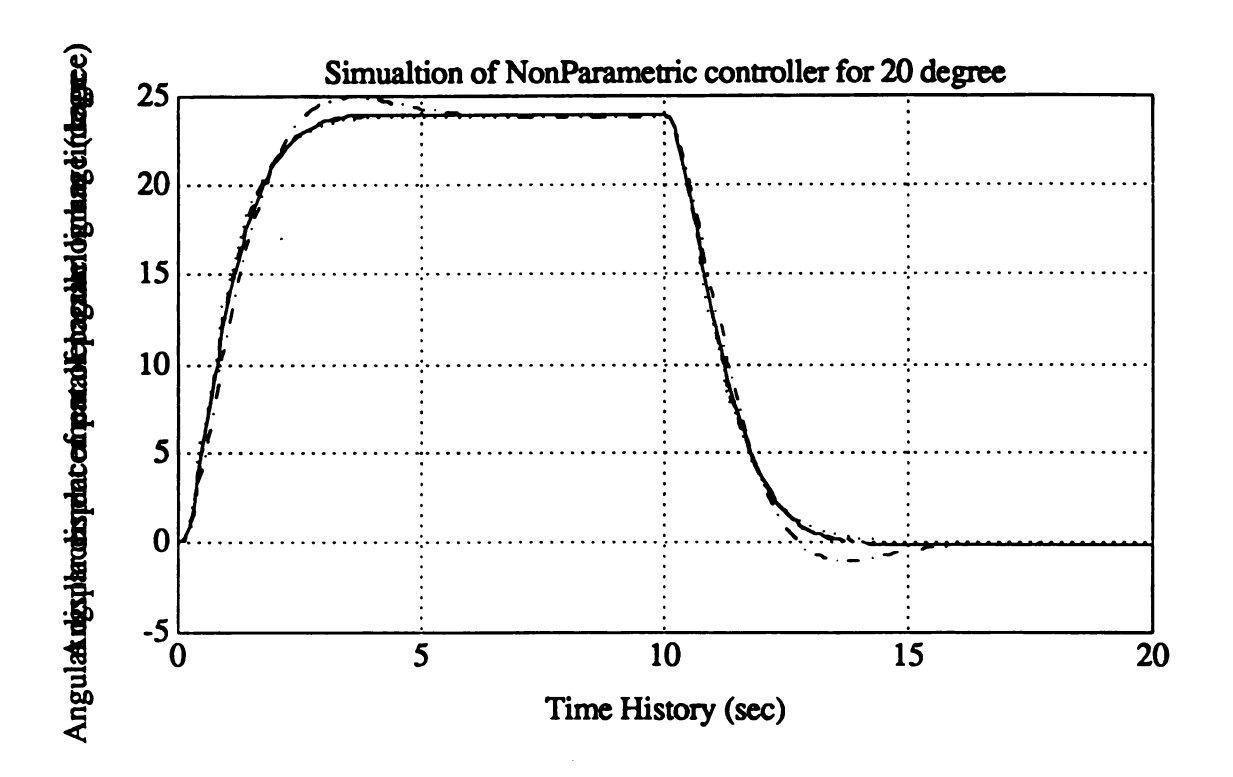


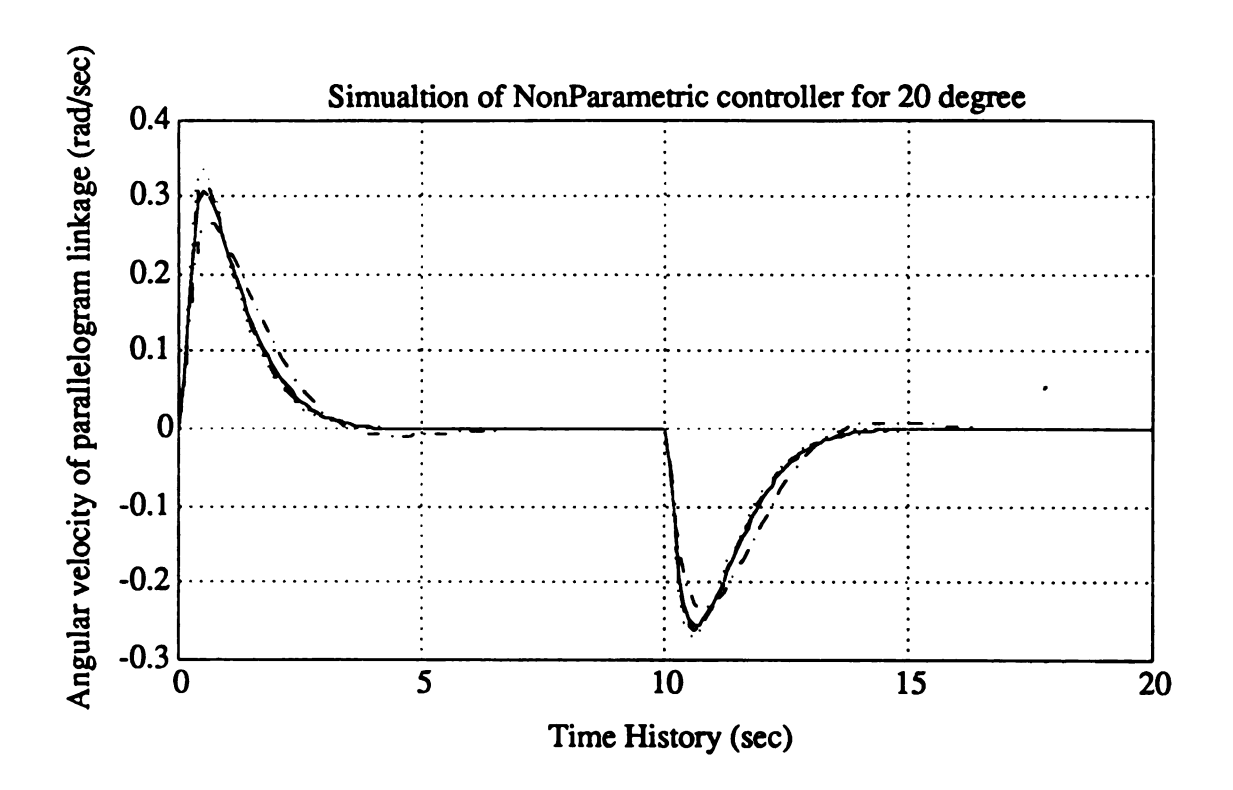


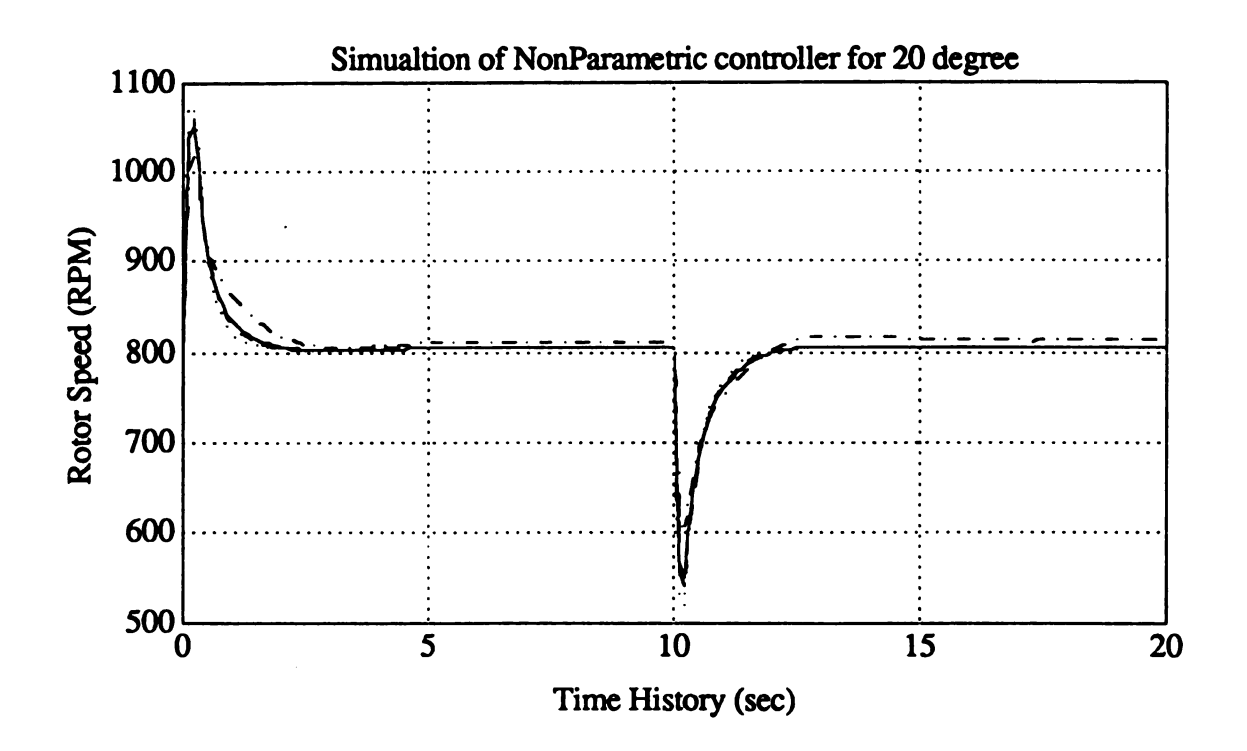


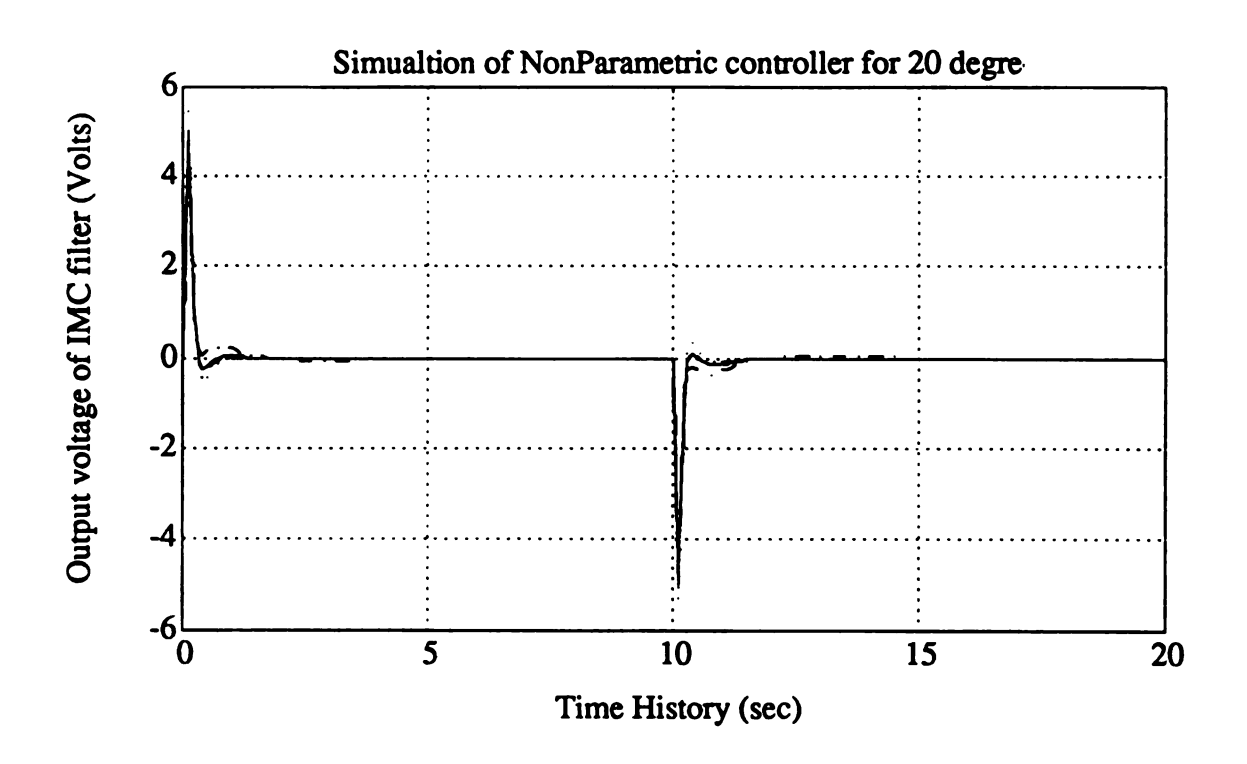


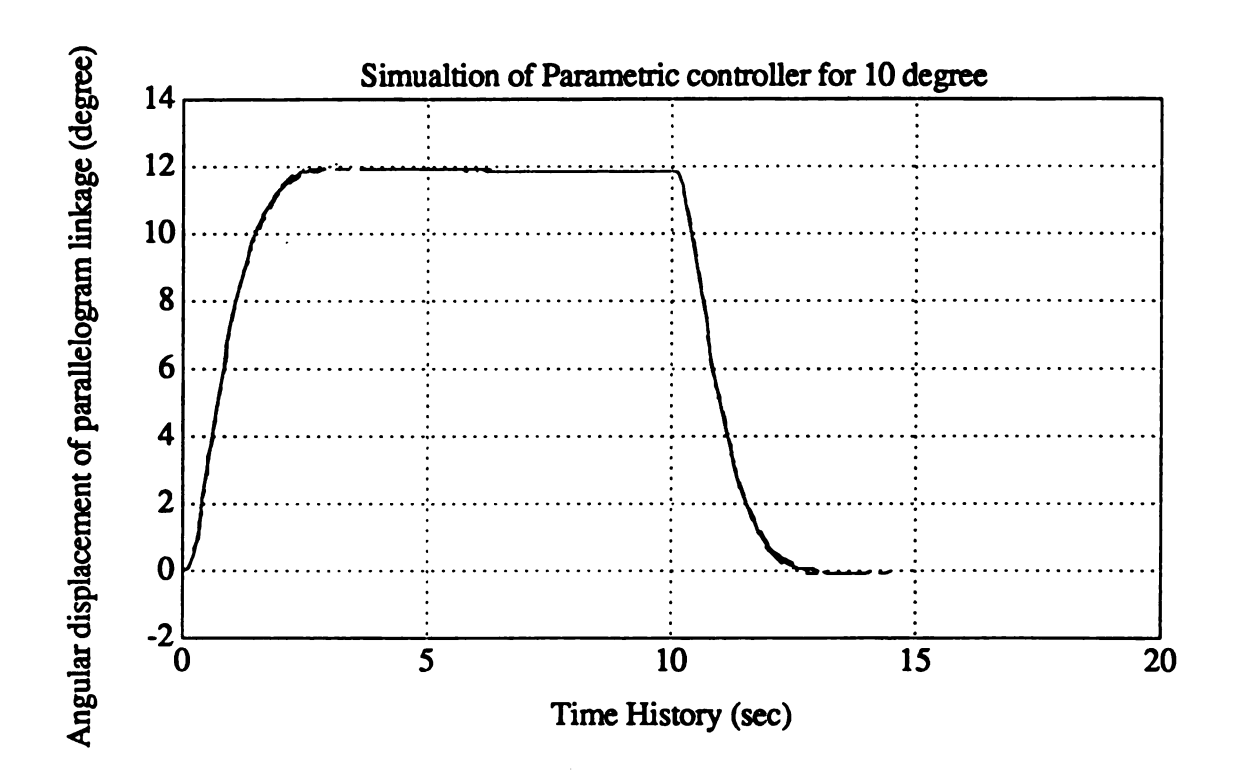


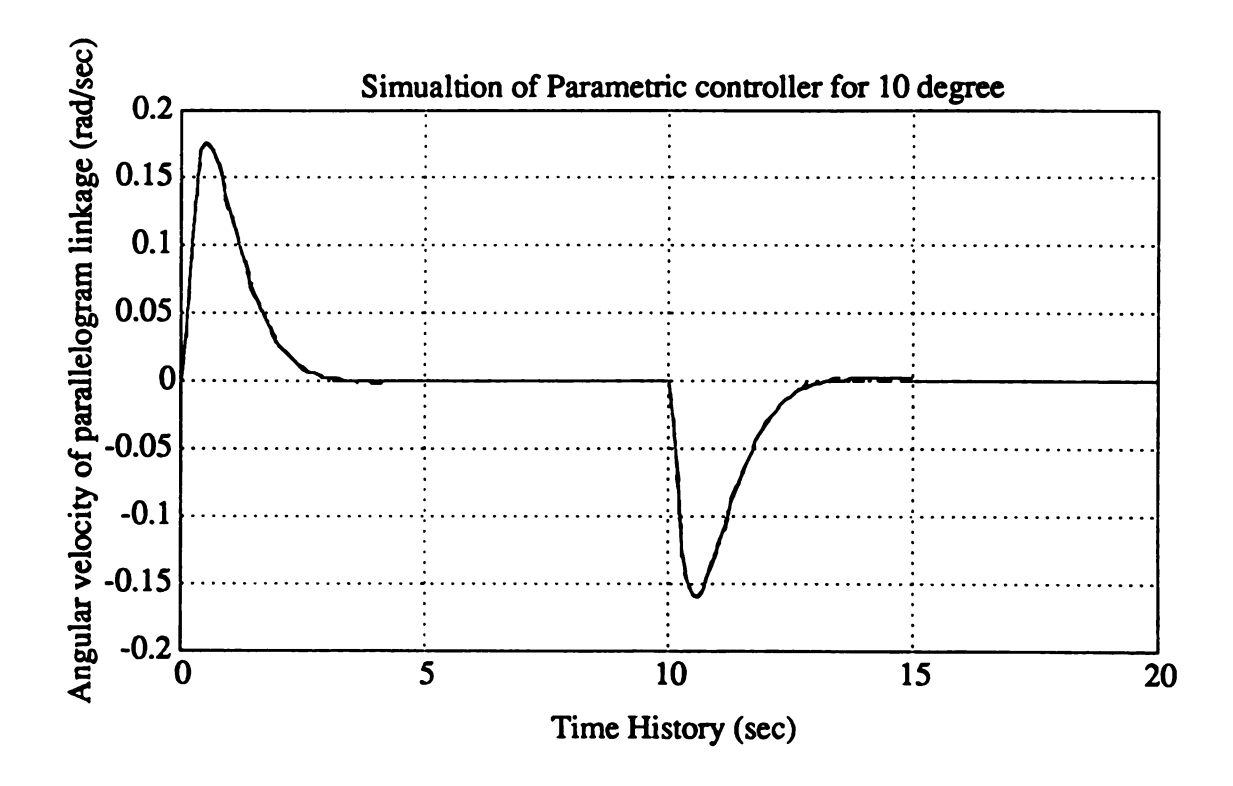


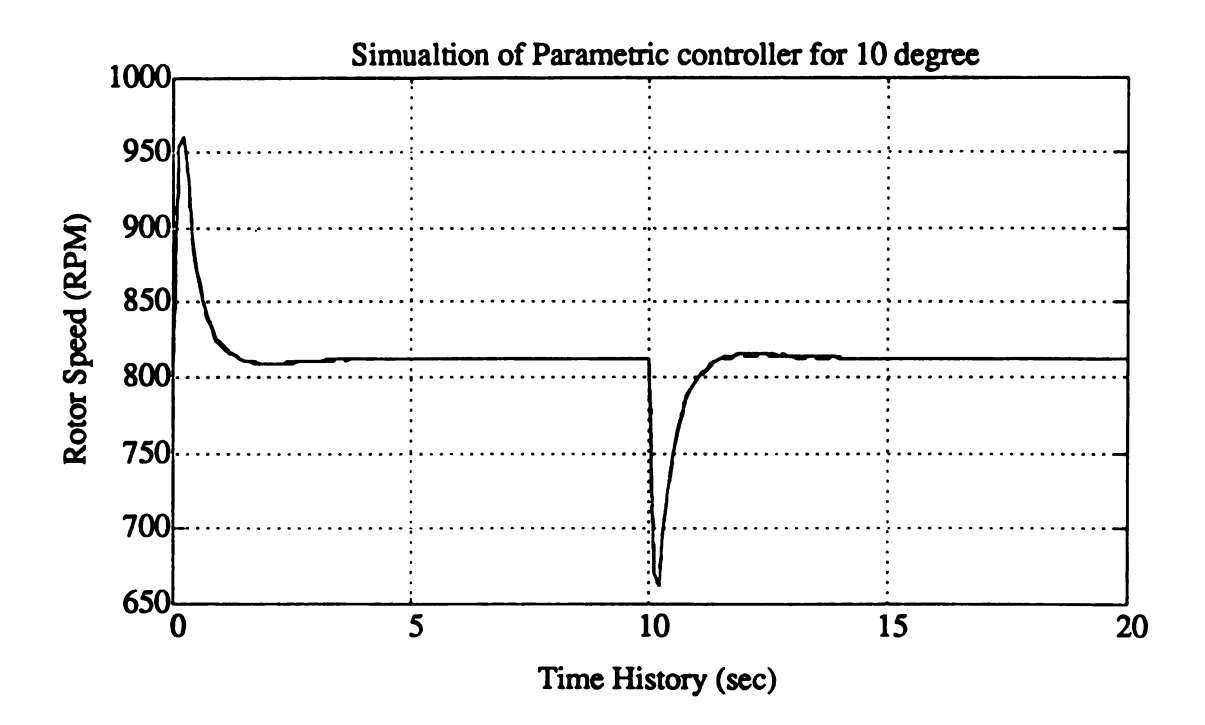


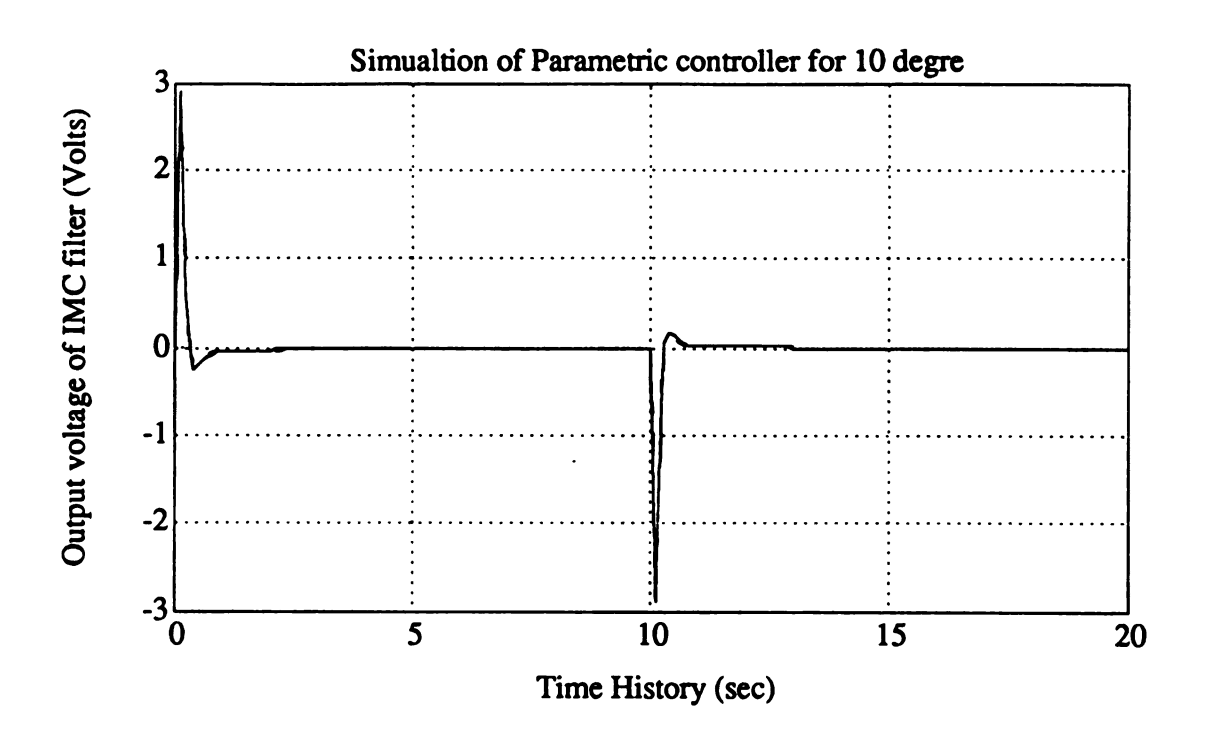


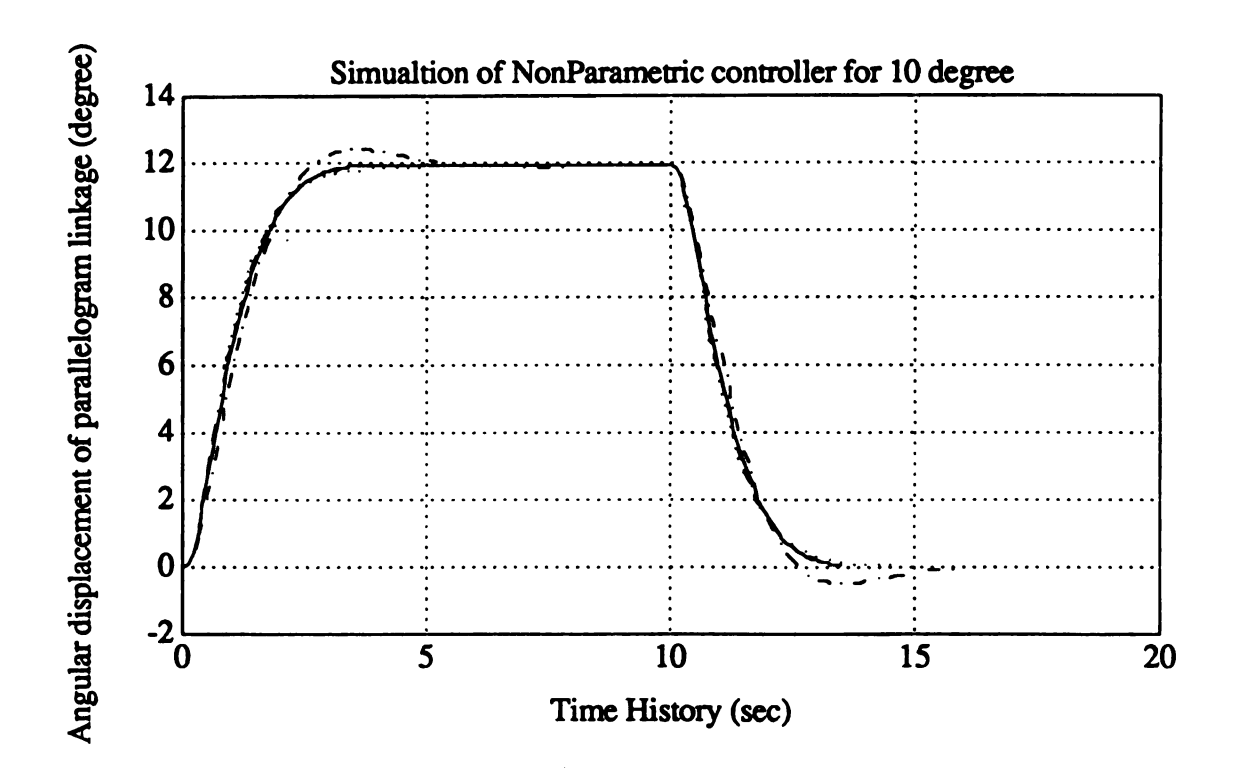


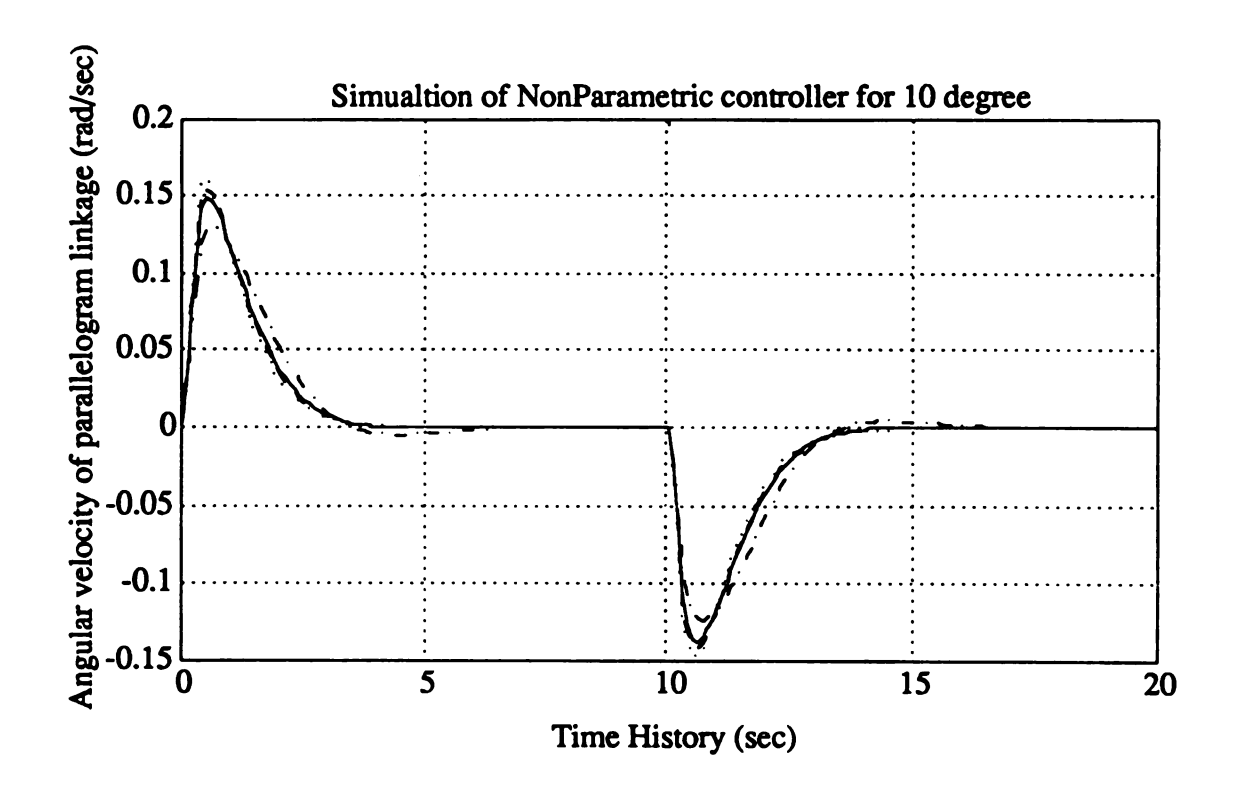


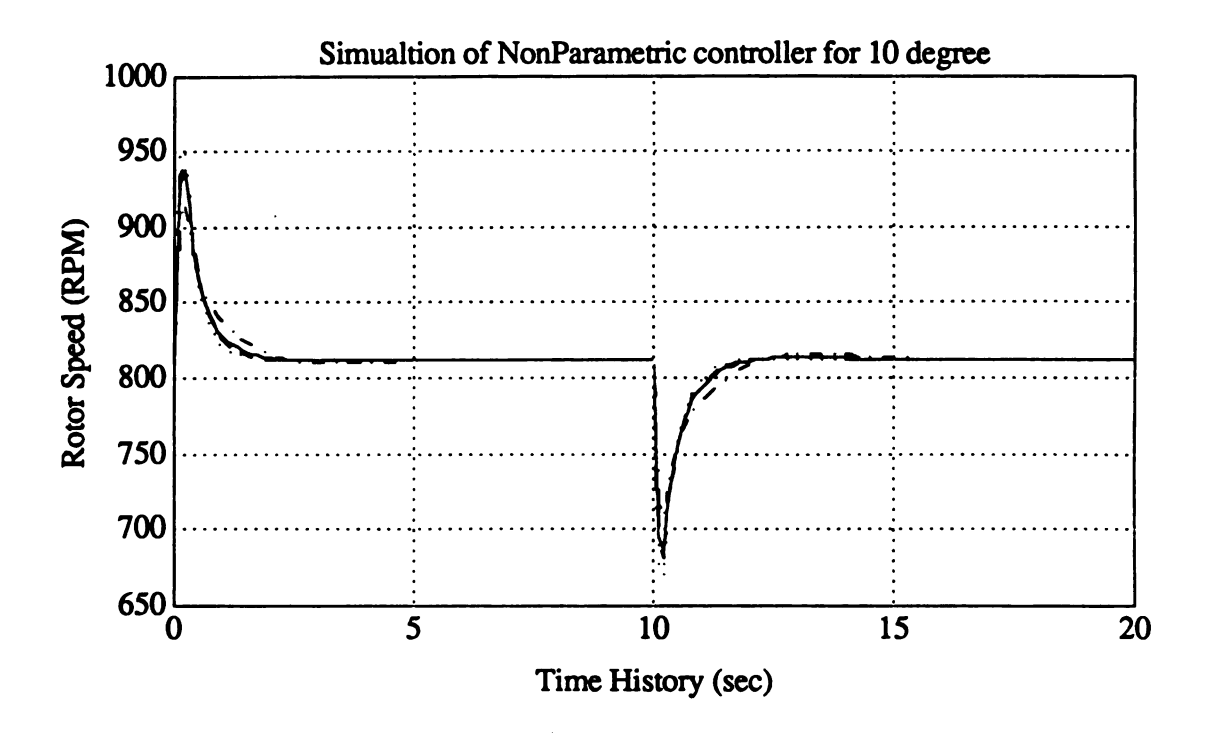


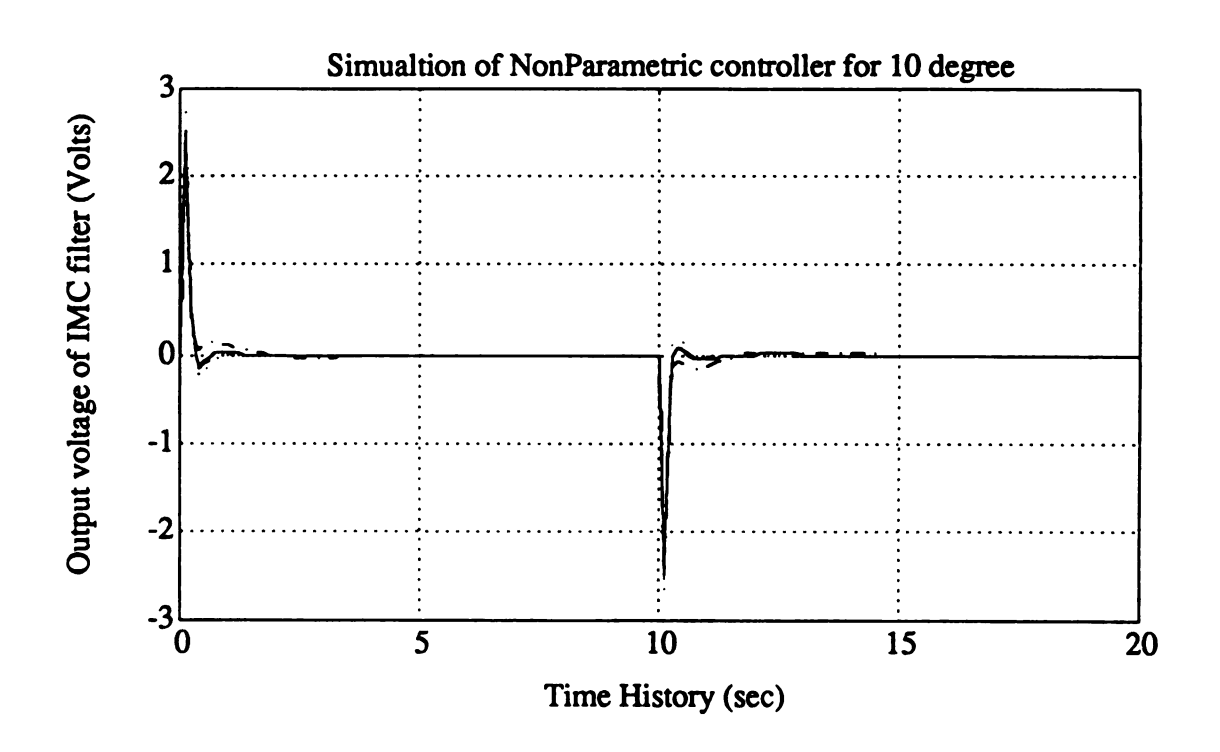












MICHIGAN STATE UNIV. LIBS 312930088502